UNIVERSITY OF SOUTHAMPTON

Faculty of Engineering and the Environment
Institute of Sound and Vibration Research

Active Acoustic Black Holes for Controlling Vibration

by

Kristian Hook

BSc. MMus.

ORCiD: 0000-0002-5011-0414

A thesis for the degree of
Doctor of Philosophy

July 2021

University of Southampton

Abstract

Faculty of Engineering and the Environment
Institute of Sound and Vibration Research

Doctor of Philosophy

Active Acoustic Black Holes for Controlling Vibration

by Kristian Hook

An Acoustic Black Hole (ABH) is a lightweight and compact damping solution, which can be realised as a lightly damped structural taper. Although ABHs are effective at attenuating vibration, their performance at lower frequencies is strongly dependent on the local modes of the taper. Limiting the size of an ABH therefore physically limits its cut-on frequency and accurate tuning is required to address low frequency problems. To improve the performance of ABHs at lower frequencies, this thesis proposes and investigates the integration of active control technologies into the ABH taper. Initially, a parametric study has been carried out which highlights how a beam based ABH termination can be geometrically tuned to maximise both narrow and broadband performance. Particularly, it is shown that the tip height and power law can be selected to minimise broadband reflection. With guidance from this study, an ABH termination has been designed and a piezoelectric patch has been attached to the taper. It has been shown through the implementation of a wave-based feedforward active control strategy that the Active ABH (AABH) outperforms a traditional constant thickness active termination and requires less electrical and computational power. However, it has also been shown that when the reflection coefficient is controlled, the local vibration in the AABH is significantly enhanced. To provide further insight into this connection, a remote damping control strategy has been considered and it has been shown that there is a control tradeoff between maximising performance and minimising the vibration of the taper. The AABH concept has then been extended to a plate with five embedded AABHs. It has been shown that the AABHs reduce the electrical power required to implement active control and provide a higher level of damping over a significantly wider bandwidth than achievable via a constant thickness plate with active elements.

In summary, this thesis presents the first exploration of integrating active control technologies into both one-dimensional and two-dimensional ABHs and demonstrates the significant benefits of combining passive and active control technologies. Future work will likely extend the novel AABH to more complex structures and consider not only their effect on structural vibration, but also on the structural radiation.

Contents

List of Figures

List of Tables

Declaration of Authorship

I declare that this thesis and the work presented in it is my own and has been generated by me as the result of my own original research.

I confirm that:

1. This work was done wholly or mainly while in candidature for a research degree at this University;
2. Where any part of this thesis has previously been submitted for a degree or any other qualification at this University or any other institution, this has been clearly stated;
3. Where I have consulted the published work of others, this is always clearly attributed;
4. Where I have quoted from the work of others, the source is always given. With the exception of such quotations, this thesis is entirely my own work;
5. I have acknowledged all main sources of help;
6. Where the thesis is based on work done by myself jointly with others, I have made clear exactly what was done by others and what I have contributed myself;
7. Parts of this work have been published as:
   - K. Hook, J. Cheer and S. Daley, "A parametric study and modal analysis of an acoustic black hole on a beam," in *Proceedings of ISMA-USD 2018*, pp. 4489–4498, 2018.
   - K. Hook, J. Cheer and S. Daley, "A Parametric Study of an Acoustic Black Hole on a Beam," *The Journal of the Acoustical Society of America*, vol. 145, no. 6, pp. 3488–3498, 2019.
   - J. Cheer, S. Daley and K. Hook, "Structural damper," *International Patent Application PCT/GB2020/050769*, 10 2020.
   - K. Hook, J. Cheer and S. Daley, "Minimisation of the reflection coefficient in a beam using an active acoustic black hole," in *INTER-NOISE and NOISE-CON Congress and Conference Proceedings*, vol. 261, no. 1, pp. 5280–5287, 2020.

- K. Hook, J. Cheer and S. Daley, "Optimal feedforward control of a beam with an active acoustic black hole termination," in *26th International Congress on Sound and Vibration*, pp. 1–8, 2019.
- K. Hook, S. Daley and J. Cheer, "Feedback active control using an acoustic black hole," in *Proceedings of ISMA-USD 2020*, pp. 1–9, 2020.
- J. Cheer, K. Hook and S. Daley, "Active feedforward control of flexural waves in an Acoustic Black Hole terminated beam," *Smart Materials and Structures* vol. 30, no. 3, pp. 1–14, 2021.

Signed:..... Date:.....

Acknowledgements

First and foremost, I would like to thank Dr. Jordan Cheer for his significant support and input throughout my PhD. He has provided guidance in all aspects of my work and has ensured that it is carried out to the highest standard. He has also helped me to significantly improve my technical writing and I feel privileged to have had him as a supervisor.

I would also like to thank Prof. Stephen Daley for his help and guidance during my PhD, particularly his industrial knowledge and his input regarding the remote damping controller formulation.

In addition to my supervisors, further thanks goes to Dr. Joe Milton and Charlie House for their help regarding finite element models, signal processing and experimental setups.

This work would also not have been possible without the funding provided by the EPSRC iCASE studentship award (Voucher number 16000058).

Finally, I would like to say a special thank you to all of my family and friends who have supported me throughout my PhD, particularly Karolína Votrubová for her continuous motivation and support through the harder times.

Definitions and Abbreviations

a_l	Acceleration measured at accelerometer l
b	Beam width
c	Flexural wave speed
$\boldsymbol{d}$	Vector of disturbance signals
d_{ϕ^-}	The reflected wave component of the disturbance signal
d	Disturbance signal
E	Young's modulus
E	Expectation operator
$\boldsymbol{e}$	Vector of error signals
e_{ϕ^-}	The reflected wave component of the error signal
e_{a_1}	Error signal from accelerometer 1
e_{a_2}	Error signal from accelerometer 2
e_l	Local taper vibration error signal
$\hat{e}_l$	Estimate of the gain and phase of the local error signal relative to the reference signal
$\boldsymbol{F}$	Excitation force
$\boldsymbol{F_p}$	Primary Excitation force
f	Frequency
f_{min}	Lower frequency limit
f_{max}	Upper frequency limit
f_l	Local sensitivity function
f_{ϕ^-}	Remote sensitivity function
$\boldsymbol{g}_{...}(\omega)$	The plant frequency response between the control actuator and the respective error sensor
$\boldsymbol{g}_{...}$	FIR filter representing the plant response between the control actuator and the respective error sensor
$\widehat{\boldsymbol{g}}_{...}(\omega)$	The estimated plant frequency response between the control actuator and the respective error sensor
$\widehat{\boldsymbol{g}}_{...}$	FIR filter representing the estimated plant response between the control actuator and the respective error sensor
$g_{...}$	The frequency response between the control actuator and the respective error signal
g_{lmj}	The j-th FIR coefficient of the plant response between the m-th piezoelectric patch and the l-th sensor

$\tilde{g}$	A point on the complex γ-plane which can be used to calculate a compensator that annihilates the remote error
h	Height
h_{min}	Minimum height of an embedded ABH
h_{plate}	The height of the plate
h_0	$h_{min} - h_{plate}$
$h(x)$	Height function of an ABH termination
$h(r_{ABH})$	Height function of an embedded ABH
h_{beam}	The height of the beam
h_{tip}	The height of the ABH tip
h_+	Positive wave decomposition variable
h_-	Negative wave decomposition variable
$\boldsymbol{h}_+$	Positive wave decomposition filter
$\boldsymbol{h}_-$	Negative wave decomposition filter
$\mathbf{I}$	Identity matrix
I_z	Moment of inertia about the z-axis
I_h	Number of FIR filter coefficients in the wave decomposition filters
$\boldsymbol{I}$	Vector of control filter coefficients
i	$\sqrt{-1}$
$i,\ j$	A specific FIR filter coefficient
$\boldsymbol{J}$	Cost function
J	FIR filter length
k	Flexural wavenumber
k_{tip}	Flexural wavenumber at the tip of the ABH
L	Number of sensors
l	Distance of the sensor array from any near-field inducing features
l_{beam}	Length of the beam
l_{abh}	Length of the ABH taper
M	Number of secondary sources
n	Sample number
n_s	A discrete number of samples
$\boldsymbol{p}_{...}$	FIR filter representing the primary response between the primary source and respective error sensor
R	Reflection coefficient
R_{atten}	Reflection coefficient attenuation
R_0	The reflection coefficient of the uncontrolled and undamped constant thickness termination
$\hat{\boldsymbol{R}}$	Matrix of filtered reference signals
$\hat{\boldsymbol{r}}_{\boldsymbol{l}}$	Vector of filtered reference signals corresponding to the l-th sensor and all M piezoelectric patches
$\hat{r}_{lm}$	The filtered reference signal corresponding to the l-th sensor and the

	m-th piezoelectric patch
$\hat{r}_{\phi^-}$	The reflected wave filtered reference signal
r	A point along the radius of the ABH
r_{ABH}	ABH radius
S	Cross-sectional area
$\boldsymbol{S_{dd}}$	Matrix of cross and power spectral densities of the disturbance signals
$\boldsymbol{S_{ee}}$	Matrix of cross and power spectral densities of the error signals
T	Sampling time period
t	Propagation time
u	Control signal
u_m	Control signal used to drive the m-th piezoelectric patch
$\boldsymbol{w}_i$	Vector of I FIR controller coefficients
$\boldsymbol{w}_{opt}$	Vector of optimal FIR control filter coefficients
w_{opt}	Optimal control filter coefficient
w_i	The i-th FIR controller coefficient
W	Wave amplitude
w	Complex flexural displacement
$\dot{w}$	Complex flexural velocity
$x(n)$	Reference signal
x_1	The location on the x-axis of sensor 1
x_2	The location on the x-axis of sensor 2
x_c	The location on the x-axis of the centre of the sensor array
x_{max}	The location on the x-axis of the ABH tip
$\boldsymbol{z}$	Vector containing the real and imaginary part of a reference signal
α	Sensitivity function
β	Positive control effort coefficient-weighting parameter (Chapters 3 and 5)
β	Remote damping variable used to express the conditions for control of the remote error signal (Chapter 4)
γ	Remote damping variable used to express the conditions for control of the local error signal
γ_0	A specific point on the complex γ-plane
Δ	Distance used to define the upper wave decomposition limit
Δ_x	Sensor separation along the beam
ϵ	Random white measurement noise with zero mean
ε	Scaling factor for the ABH termination height function
η_{Beam}	Isotropic damping loss factor for the beam
η_{ABH}	Isotropic damping loss factor for the ABH
θ	Vector containing the real and imaginary part of the error signal with respect the the reference signal
κ	Feedback compensator
κ_0	Feedback compensator calculated from γ_0

λ	Flexural wavelength
λ_{tip}	Flexural wavelength at the tip of the ABH
λ	RLS forgetting factor
μ	Power law of the ABH taper
ν	Poisson's ratio
ξ	Regularisation factor
π	Pi
ρ	Density
v	Gain relative to the reference signal
ϕ	Phase relative to the reference signal
ϕ^+	Positive travelling wave component
ϕ^-	Negative travelling wave component
ω	Angular frequency

AABH	Active Acoustic Black Hole
ABH	Acoustic Black Hole
ADC	Analogue to Digital Converter
ASAC	Active Structural Acoustic Control
AVC	Active Vibration Control
DAC	Digital to Analogue Converter
DSP	Digital Signal Processor
FE	Finite Element
FIR	Finite Impulse Response
FxLMS	Filtered reference Least Mean Squares
IHC	Instantaneous Harmonic Controller
NMSE	Normalised Mean Squared Error
PSD	Power Spectral Density
PZT	Piezoelectric Transducer
RLS	Recursive Least Squares

Chapter 1

Introduction

When subjected to a time-varying disturbance, a structure will vibrate with a response that is dependent on its mass, stiffness and damping [1]. Vibration in structures is generally undesirable [2] and various solutions, including damping technologies, have been created to reduce the level of vibration. In 1988, a lightweight damping solution, realised as a structure with a smoothly decreasing thickness, was proposed as a means to reduce flexural vibrations in a beam or plate [3]. The perhaps misleading terminology 'Acoustic Black Hole' (ABH) arose due to an article by Krylov and Tilman that compared the ABH damping mechanism to the behaviour of an astrological black hole [4]. The term ABH has now become standardised in the literature and this thesis will continue to use the term ABH for consistency. Since the early work of Krylov and Tilman, there has been a growing number of investigations into ABHs that can be separated into three broad categories: ABHs for vibration control, ABHs for energy harvesting and ABHs for acoustic wave reduction. Interestingly, the latter is probably the most fitting category for the name ABH. This thesis will focus on the use of ABHs for vibration control and a literature review of the work in this area will be presented in this chapter. With respect to the application of ABHs for energy harvesting [5–10] and acoustic wave reduction [11–13], the reader is referred to the literature for further information, as these areas do not form the focus of this thesis.

In order to contextualise the ABH research presented in this thesis, an introduction to the concept behind the ABH and the physical mechanism via which it is able to achieve significant levels of structural damping is provided. A review of the literature in the field of ABHs for vibration control will then be presented. Finally, an outline of the thesis structure and objectives of each chapter is given in Section 1.3 and the key contributions of this thesis are presented in Section 1.4

1.1 Acoustic Black Holes

The ABH effect, as described by Mironov in 1988 [3], is a phenomenon that occurs when a beam or plate is tapered to a point, over a distance equal to or larger than the structural wavelength. Figure 1.1 shows an example of an ABH, seen as the tapering of

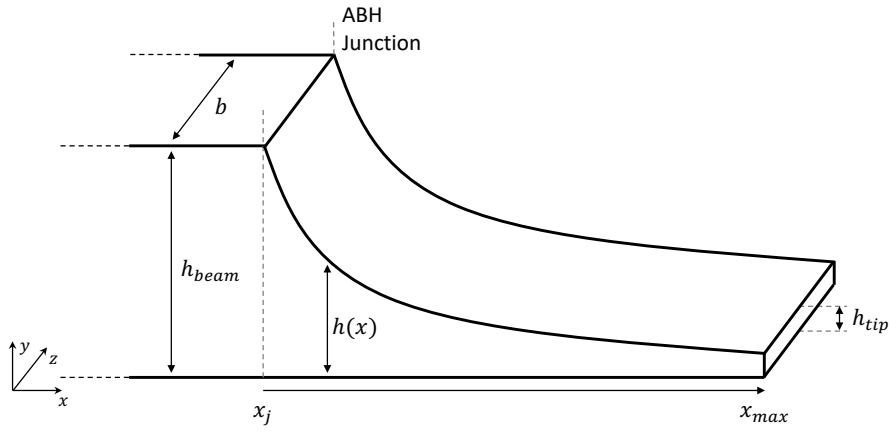

FIGURE 1.1: A diagram of an ABH taper. h_{beam} is the height of the beam, b is the width of the beam, $h(x)$ is the height function of the taper that varies along the x-axis, x_j is the location of the ABH junction, x_{max} is the location of the tip and h_{tip} is the tip height.

a beam via a power law height function, $h(x)$. The behaviour of such an ABH can be explained by considering flexural vibrations travelling down a tapered Euler-Bernoulli beam. Starting with Euler-Bernoulli beam theory, the equation of motion for free flexural vibration of a homogeneous beam is

$$EI_z \frac{\partial^4 w(x,t)}{\partial x^4} + \rho S \frac{\partial^2 w(x,t)}{\partial t^2} = 0, \tag{1.1}$$

where E is the Young's modulus of the beam, I_z is the moment of inertia about the bending axis, ρ is the density of the beam, S is the cross-sectional area of the beam and w is the complex wave amplitude, which can be expressed as

$$w(x,t) = W\mathrm{e}^{(kx+i\omega t)}, \tag{1.2}$$

where W is the amplitude of the wave, k is the flexural wavenumber, ω is the angular frequency of the wave and t is the propagation time [14, 15]. Substituting Equation 1.2 into 1.1 gives

$$EI_z k^4 W\mathrm{e}^{(kx+i\omega t)} - \rho S\omega^2 W\mathrm{e}^{(kx+i\omega t)} = 0, \tag{1.3}$$

which, with some rearrangement, can be organised into an expression for the flexural wavenumber,

$$k = \left(\frac{\rho S\omega^2}{EI_z}\right)^{\frac{1}{4}}. \tag{1.4}$$

The flexural wavenumber can be linked to the height function of the ABH shown in Figure 1.1 by considering a rectangular cross-section, such as a slice from the ABH termination shown in Figure 1.1, where b is the width of the cross-section and $h(x)$ is the height of the cross-section. In this case, the cross-sectional area, which is dependent on coordinate position x, can be expressed as

$$S(x) = bh(x). \tag{1.5}$$

The bending moment of inertia of a rectangular cross-section [16] can be written as

$$I_z = \frac{1}{12} bh^3(x). \tag{1.6}$$

Substituting Equations 1.5 and 1.6 into Equation 1.4, the flexural wavenumber can be expressed in terms of the height of the beam as

$$k(x) = \left(\frac{12\rho\omega^2}{Eh^2(x)} \right)^{\frac{1}{4}}. \tag{1.7}$$

It can be seen from equation 1.7, that if the height of the beam were to decrease, the flexural wavenumber would increase, approaching infinity at an infinitely small height. The flexural wavenumber can also be expressed as

$$k = \frac{\omega}{c} = \frac{2\pi}{\lambda}, \tag{1.8}$$

which allows the flexural wave speed to be expressed as

$$c(x) = \left(\frac{Eh^2(x)\omega^2}{12\rho} \right)^{\frac{1}{4}}, \tag{1.9}$$

and the flexural wavelength to be expressed as

$$\lambda(x) = \left(\frac{4Eh^2(x)\pi^4}{3\rho\omega^2} \right)^{\frac{1}{4}}. \tag{1.10}$$

For a tapered semi-infinite plate, the same equations may be used by inclusion of the poisson ratio [17].

It can be seen from Equations 1.9 and 1.10, that as the height of the taper decreases along the x-axis, the flexural wave speed and wavelength also decrease, theoretically approaching zero at an infinitely small height. Therefore, if a flexural wave were to enter an ABH with an infinitely small tip height, the wave would never reach the end of the taper and would not reflect back out of the ABH. However, in practice, an infinitely small tip height cannot be achieved and there will be reflection from the truncated tip, which will increase as the tip height is increased [4]. The performance of ABHs with finite tip heights can be significantly improved by the addition of a viscoelastic damping

layer, which dampens the vibration of the ABH via hysteresis [2]. Shorter wavelength vibration is more easily attenuated using hysteretic damping treatments and so only a thin viscoelastic layer is required due to the wave compression that occurs along the length of the taper, described by Equation 1.10. This effect has been practically demonstrated for thin viscoelastic damping layers added to either one or both sides of the taper [4, 18].

In addition to a finite tip height, in practice, a rapidly changing height function will also result in reflection due to the high impedance change. This effect has been explored in the literature [19–22] and the WKB approximation can be used to analytically determine whether a specific height function is likely to produce a high level of reflection; this will be reviewed in the following section. Subsequently, some various ABH designs will be reviewed in Sections 1.1.2 through to 1.1.3, before a discussion on the manufacturing of ABHs is presented in Section 1.1.5. Finally, Section 1.1.6 will present a brief review of semi-active ABHs.

1.1.1 The WKB Approximation and Modelling the ABH

The WKB approximation is a popular method for finding suitable modifications of plane-wave solutions for propagation in slowly varying structures [23]. In the ABH literature, a first-order WKB approximation to the flexural wave equation is generally used, which takes account of the variation of the wavenumber in addition to a varying amplitude term [3, 24]. This approximation has also been referred to as the geometrical acoustics approach [4, 25, 26] and a measure of the validity of this approximation has been used called the 'Normalised Wavenumber Variation' (NWV) [19, 21]. Additionally, higher order WKB approximations for modelling ABHs have been investigated in [22] and further details regarding the WKB approximation for modelling ABHs can be found in this reference.

The validity of the WKB approximation is limited to structures with gradual changes in impedance and therefore gradual changes in the wavenumber. The condition for validity can be found, for example, in [3, 19, 25], and can be expressed as

$$\frac{dk}{dx} \ll \left|k^2\right|, \tag{1.11}$$

where k is the flexural wavenumber and x is a spatial coordinate along the axis of propagation. Equation 1.11 can be rearranged to express the condition for validity as

$$\left|\frac{1}{k^2}\frac{dk}{dx}\right| \ll 1. \tag{1.12}$$

The flexural wavenumber from Equation 1.7 can be substituted in Equation 1.12 to check whether the WKB approximation is valid at a specific point along a tapered beam

at a specific frequency. This has been investigated in [19,21] as an ABH design tool and, as mentioned above, has been referred to as the NWV. Taking the height function used in [19], which can be expressed as

$$h(x) = \varepsilon x^{\mu} + h_{tip}, \tag{1.13}$$

where μ is the power law of the taper, h_{tip} is the tip height and ε is a scaling factor, the NWV can be calculated for each individual point along the taper for a range of frequencies. Some examples are shown in Figure 1.2 for a taper with a starting beam height of 1 cm, a length of 7 cm and a tip height of 0.5 mm. Figure 1.2 shows that as the power law

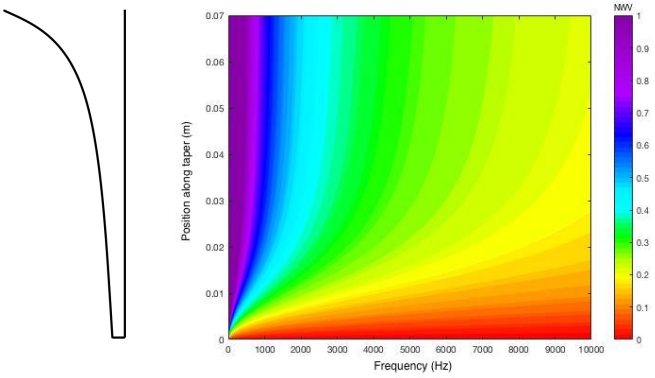

(a) $\mu = 2$

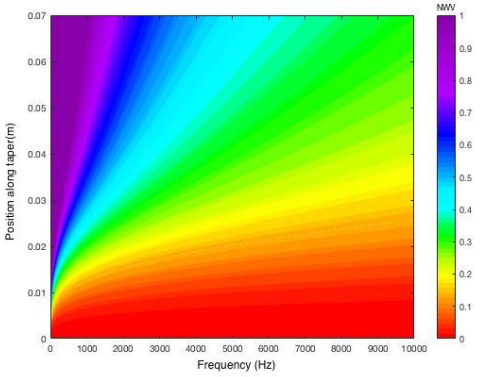

(b) $\mu = 3$

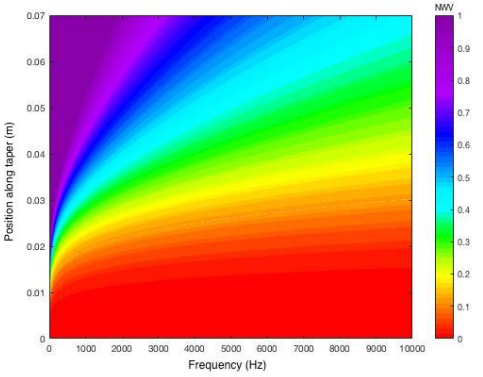

(c) $\mu = 4$

FIGURE 1.2: The WKB approximation validity (NWV) plotted over frequency and position along the taper for μ = 2, 3 and 4 power tapers. A guide showing the taper is presented to the left of (a).

is increased, the NVW becomes higher close to the junction of the ABH. This is because a higher power law gives a higher gradient change, and hence a higher impedance change, near the ABH junction. In addition, when frequency is increased, the NWV decreases because the wavelength is smaller relative to the impedance change. In the literature, a rule of thumb value of 0.4 or less has been accepted for the NWV [21]. If this condition is not satisfied, the WKB approximation can not be considered valid. It

is, therefore, clear that the first order WKB approximation becomes invalid over the full bandwidth presented for power laws higher than 3, but is also invalid for lower power laws at low frequencies. As a result, care must be taken when carrying out an investigation into ABHs using an analytical model with a first order WKB approximation and given the focus of this thesis is on enhancing the low frequency performance of the ABH, it will be necessary to use an alternative modelling approach.

1.1.2 Acoustic Black Hole Terminations

Although the slowing of flexural waves in a tapered plate was first observed by Mironov in 1988 [3], the behaviour of an ABH termination on a beam has been investigated in more detail by Krylov and Tilman in [4]. They showed, via a two dimensional analytical model of an ABH power law taper defined by $h(x) = \varepsilon x^{u}$, how the reflection coefficient of an ABH varies over frequency. In addition, a sinusoidal taper has also been investigated [4] and other taper profiles have been compared by Karlos *et. al.* [22], however, in general, the variation between the performance of the different taper functions has been shown to be relatively small. Therefore, a power law function has been adopted in the majority of the literature. In [4], Krylov and Tilman also showed that, for finite tip heights, a small amount of damping is required to achieve good performance, and that the ABH performs better at higher frequencies. It has also been shown in [4] that in a small number of discrete cases, the reflection coefficient of the ABH could be reduced by increasing the power law, decreasing the tip height or increasing the taper length. However, the ABH model in [4] uses a first order WKB approximation, which in Section 1.1.1 has been shown to be invalid for lower power laws at lower frequencies and this invalidity extends to higher frequencies when the power law is increased.

Despite the limitations of using the first order WKB approximation, Feurtado and Conlon have further investigated the NWV at the taper-beam boundary [19, 20] and a multi-objective optimisation of an analytical model has been carried out by Shepherd *et. al.* [21], optimising the NWV against the reflection coefficient using the analytical model. It has been found that, for the ABH investigated, a power of approximately 3 gave the optimum NWV-reflection tradeoff. This is consistent with the results shown in Figure 1.2, where it is shown that the WKB approximation starts to become invalid over a broader frequency range above a power law of 3; in contrast, the analytical model used in [4] predicts that a higher power law results in a lower reflection coefficient.

In order to further understand the damping performance of ABHs, Denis *et. al.* [27] have carried out an investigation into the reflection coefficient of an ABH termination on a beam using a geometrical acoustics based model, a beam waveguide model, a plate model and an experimental implementation. ABHs made from aluminium and a polymer (with the inclusion of a thin damping strip on the taper) have been used in

the investigation and the velocity at a mesh of points has been measured. The reflection coefficient has then been calculated using a method based on the Kundt tube-like technique [27]. Figure 1.3(a) shows the reflection coefficient that has been calculated

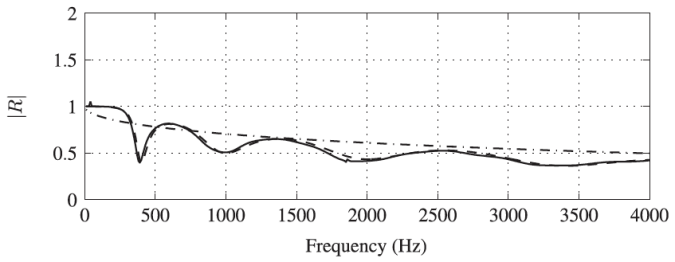

(a)

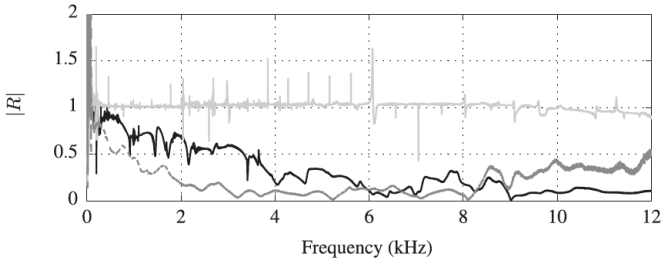

(b)

FIGURE 1.3: (a) The reflection coefficient of an ABH calculated using the geometrical model (dash-dotted line), the beam waveguide model (dashed line) and the plate model (full line). (b) The estimated reflection coefficient for an ABH termination made from aluminium (full black line) and polymer (dashed grey line). The light grey line represents the aluminium reference beam [27].

using the three different models. A comparison of the models shows that the beam waveguide and plate models yield the same result, but that the geometrical acoustic approach does not predict the oscillations in the reflection coefficient. The oscillations in the reflection coefficient have also previously been observed in [28, 29] and are dependent on the local modes of the ABH, which are not taken into account in the geometric acoustics model. It has also been shown in [29] that at higher frequencies, the modal overlap in the ABH is higher and the oscillations in the reflection coefficient are broadened. Figure 1.3(b) presents the experimentally estimated reflection coefficient for the aluminium ABH, the polymer ABH and the aluminium reference beam. From these results it can be seen that the manufactured aluminium ABH exhibits the oscillations in the reflection coefficient, as predicted by the waveguide and plate models. It can also be seen that the bands of low reflection are less pronounced for the polymer ABH, and that the aluminium reference beam exhibits almost perfect reflection over the bandwidth tested [27].

To further understand and visualise wave propagation in a damped ABH, Ji *et. al.* [18] have used a pulse laser to excite an ABH. A laser doppler vibrometer has been used to detect the flexural vibrations in the ABH, which were separated into their incident

and reflected components. The reflection coefficient has been calculated for a selection of ABH designs, with damping layers of varying thickness and location. The results demonstrated that there is an optimal thickness for the damping layer on their ABH, which is approximately 5 times thicker than the tip height. It has also been shown that the attenuation is enhanced when the damping strip is placed near the tip of the taper, where the wavelength is the shortest.

Novel designs such as a spiral shaped ABH taper [30] have been proposed to minimise the space an ABH occupies. In [30], it has been shown that introducing an Archimedean spiral yielded a similar reduction in reflection, allowing for a longer taper, and thus improved attenuation at lower frequencies, without significantly increasing the overall ABH size; Figure 1.4 shows a diagram of this taper design. The concept of the spiral

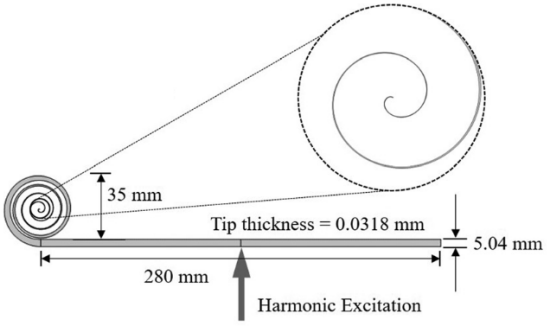

FIGURE 1.4: Lee and Jeon's Archimedean spiral ABH [30].

ABH has been investigated experimentally in [31]. The curvature effect on the driving point mobility was measured and compared to the modelled results. It was found that, compared to a straight ABH, the curvature effect did not significantly change the structural vibration above 2 kHz. It was also found that curling the ABH changed the resonance frequencies and that the gap distance, which is the distance between each layer of the spiral, could be used to tune the frequency of these resonances. Although this design requires less space, it may be more challenging to manufacture accurately and to integrate into the design of structures.

1.1.3 Embedded Acoustic Black Holes

In structures comprising of beams and plates, there is not always a free end that can be used to implement an ABH termination. Therefore, investigations have been carried out that examine embedded ABHs as a more practical realisation in structures. A design has been investigated in [40], where a number of ABHs were embedded within a beam, as shown in Figure 1.5. In [40], Tang and Cheng found that as more ABHs are stacked along a beam, they collectively form a more efficient broadband absorber, above the frequency of the first local cut-on mode. Although effective at absorbing

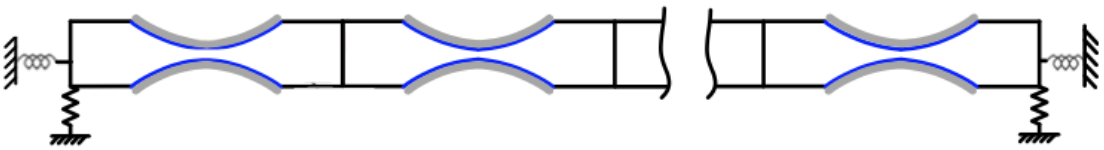

FIGURE 1.5: The design of multiple ABHs along a beam, with damping strips applied [40].

energy, the thin regions will significantly decrease the stiffness of the structure and therefore limit the practical uses of this design.

Whereas the performance of a beam based ABH has generally been gauged by its reflection coefficient or transmission, the performance of a plate based ABH has generally been gauged by its ability to reduce the structural response or radiated sound power. In [41], a numerical analysis has been performed on the different arrangements of ABHs in a plate, such as can be seen in Figure 1.6. The structural response and

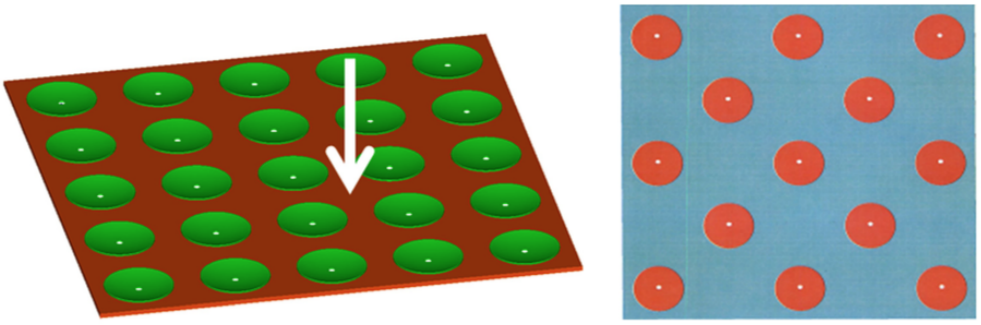

(a) 25 ABH grid (b) Partial 13 ABH grid

FIGURE 1.6: The different grid layouts of ABHs in a plate that were investigated in [41].

sound power radiated by these plates has been studied and it has been shown that both designs behaved in a similar way and both were effective at reducing the global structural vibration and radiated sound power when damping material was added to the ABHs. In another investigation, it has been shown that the transmission loss of a plate with 20 embedded ABHs is significantly higher than either an undamped or uniform plate [42]. Both a distributed and point drive excitation were used and were found to produce similar results.

The low frequency performance of plates with embedded ABHs has also been shown to strongly depend on the specific low order vibrational modes of the ABHs [43], which is consistent with the beam based studies presented in Section 1.1.2. In order to provide further insight into the behaviour of embedded ABHs, Feurtado and Conlon have used a scanning laser vibrometer to measure the velocities of and around the ABHs [44]. The

measured surface velocities were then transformed into the wavenumber domain. An investigation has also taken place that presents the phase accumulation of a plate with embedded ABHs [45]. In concurrence with previous results, it has been found that at low frequencies, the low order plate modes dominated the response and the ABHs had little effect. It was only above the first local ABH mode, named the cut-on mode, that the ABH began to significantly impact plate vibrations. The first local ABH modal frequency, and therefore the cut-on frequency of an ABH, can be calculated analytically and this has been shown, for example, in [46, 47].

Alternative ABH designs have also been investigated in [48, 49]. The examples presented in Figure 1.7 show that for some designs, the region with the minimum thickness has been shifted outward so that the ABH takes on a ring-like appearance. Other designs make use of stiffeners, similarly to [50] or distribute ABHs in rings. The designs

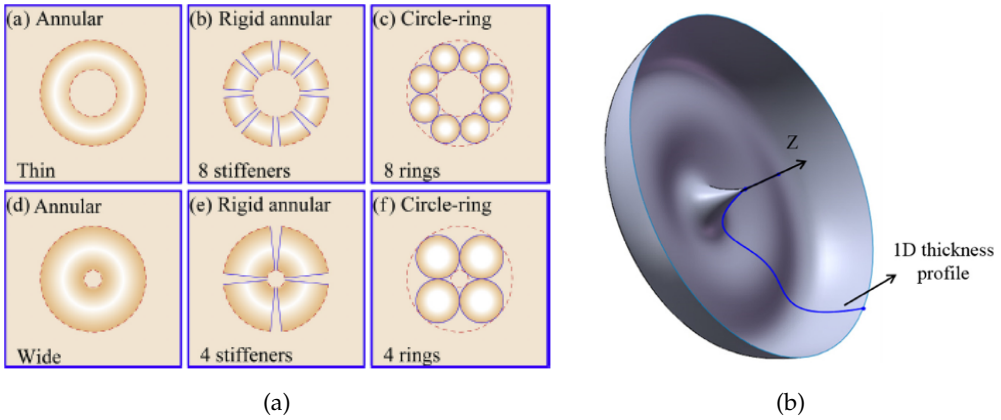

FIGURE 1.7: The different ABH designs investigated in [48, 49].

in Figure 1.7(a) have been created with the intention of surrounding and isolating an excitation area on a plate to avoid vibration transmission. Although the performance of the annular ABH without stiffeners has been shown to be the most effective at increasing transmission loss, the inclusion of some stiffeners has been shown to avoid excessive weakness in the plate. The addition of more ABHs in a concentric design has also been shown to be beneficial, however, if these ABHs are smaller, the cut-on frequency will be higher and the low frequency performance will deteriorate. The design in Figure 1.7(b) has been shown to enlarge the energy focussing area of the ABH and gives bi-directional ABH effects due to the inbound and outbound waves passing through the region of minimum thickness. As a consequence of this effect, it has been shown that two local ABH modes dominated the overall increase in damping.

Embedding ABHs within a plate, rather than on the surface, has also been investigated in [50–52], where the ABHs have been tunnelled into plates. Examples of the designs, with and without a strengthening stud, can be seen in Figure 1.8 [50, 51]. All tunnelled ABH plates were found to be effective at attenuating vibration and the strengthening

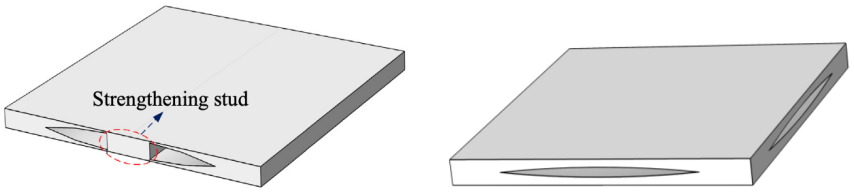

(a) (b)

FIGURE 1.8: The design of an ABH tunnelled into a plate (a) with and (b) without a strengthening stud [50,51].

stud that connects the two branches of the tunnelled ABHs has been shown to create a large impedance mismatch with the thin walls and generates effective Bragg scattering above 4 kHz, thus broadening the transmission band gaps and improving performance.

Ma and Cheng have investigated the topological optimisation of damping material applied to an ABH, with the objective of minimising either the vibration or the sound radiated from a plate with a singular ABH [53]. The optimal placement of damping material for minimising vibration or radiated sound power has been compared to the conventional central covering of the ABH. An example of the layouts for three frequencies can be seen in Figure 1.9. The first frequency was below the cut-on frequency of

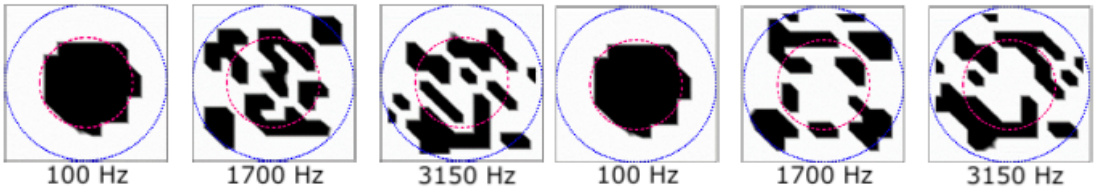

(a) (b)

FIGURE 1.9: Optimal damping distribution to minimise (a) vibration and (b) radiated sound power at three frequencies [53]. The first, 100 Hz, is below the cut-on frequency of the ABH; the second, 1.7 kHz, is above the cut-on frequency of the ABH but below the critical frequency of the ABH; the third, 3.15 kHz, is above the critical frequency of the ABH.

the ABH, where it has been found that the optimum damping configuration did not vary much from the conventional central covering. The second frequency was between the cut-on frequency of the ABH and the critical frequency of the ABH, where it has been found that the optimum damping configuration varies between minimising the vibration and minimising the radiated sound power. In this case, the damping material is placed away from the centre of the ABH to minimise the radiated sound power. This trend is also shown at the higher frequency, which is above the critical frequency (where acoustic wavelength becomes smaller than its structural counterpart [54]) of the ABH.

1.1.4 Surface-Attached Acoustic Black Holes

In addition to ABHs embedded in structures, recent investigations have been carried out to examine the use of ABHs as surface-attached dampers. For example, a continuation of the work on spiral ABHs has seen them implemented as surface-attached vibration absorbers [32], as shown in Figure 1.10(a). Alternative types of surface attached

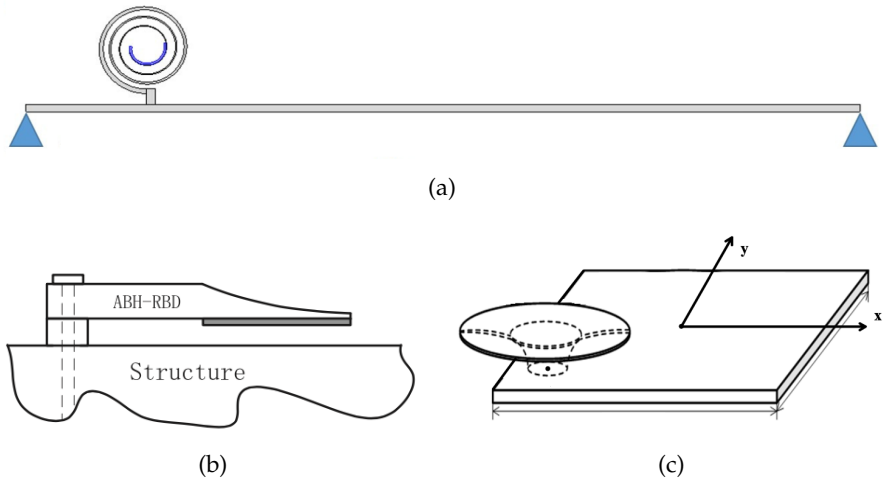

FIGURE 1.10: The design of surface-attached ABHs with damping strips applied [32–34].

ABHs are also shown in Figure 1.10. Figure 1.10(b) shows the surface-attached ABH from [33], where a standard ABH has been connected to the surface of a beam to act as a resonant beam damper. Figure 1.10(c) shows the surface-attached ABH used by Wang *et. al.* [34], where an ABH disk has been attached to a structure. All surface-attached vibration absorbers have been shown to be effective at dampening structural vibrations, however they require careful design and placement in order to couple effectively with the modes of the primary structure.

1.1.5 Manufacture of Acoustic Black Holes

In addition to the design of ABHs, the manufacturing of a precise taper can sometimes be problematic in real structures. Due to the thin region, the taper is susceptible to damage from, for example, imprecise milling. The effect of minor damage and imperfections within an ABH taper has been investigated by Bowyer *et. al.* [35, 36]. Additive layer manufacturing has been suggested to provide greater flexibility and has been investigated by Rothe et al. in [37]. The additive method allows for high definition structures to be created with fewer defects than would be seen if the same structure were milled. Additive manufacturing also offers the possibility to create intricate designs

that are not possible using more traditional manufacturing methods. The additive process may also allow damping material to be precisely integrated into novel ABH structures without the need for adhesives. For example, in [38], a series of additive designs have been investigated where the Youngs modulus of the material has been changed between 2.5 GPa and 0.2 GPa along the ABH taper. It has been found that designs with a more elastic tip are particularly effective at reducing the reflection coefficient of the termination and are able to achieve a lower reflection coefficient than the conventional ABH. However, these structures may not always be suitable for industrial applications due to the thin and soft tip of the ABH. Therefore, Cheer and Daley [39] have examined a functionally graded ABH design where only the elastic modulus is graded, rather than the physical structure itself. This work has demonstrated how the material properties can be smoothly varied to achieve comparable performance to a conventional geometric ABH without the need for a thin tip.

1.1.6 Semi-Active Acoustic Black Holes

The use of semi-active technologies in the design of ABHs has been studied to provide further tune-ability. For example, Ouisse *et. al.* [55] have varied the temperature of a viscoelastic damping layer in order to control its mechanical properties. It has been shown that by controlling the temperature of the damping layer, the bands of low reflection can be tuned to particular frequencies and the broadband reflection coefficient can be changed. It has also been shown that at the glass transition temperature, the loss factor of the damping material was as high as 2.4, which significantly increased the damping of the ABH. Although this temperature tuned damping could be used to effectively reduce the reflection coefficient above the second modal frequency of the taper, the performance of the ABH at lower frequencies was still shown to be strongly dependent on the bands of low reflection. In addition, this design required the ABH to be located in a thermal chamber which, in practical applications, could be problematic. Further work is therefore required to utilise this tuning method.

Zhao [56] has performed a theoretical and numerical study that compares the application of a viscoelastic damping strip to a shunted piezoelectric transducer under steady-state response. A diagram of the semi-active ABHs is shown in Figure 1.11. The thickness of the viscoelastic damping layer and the external resistor connected to the piezoelectric transducer have both been varied [56]. It has been concluded that the addition of a shunted piezoelectric transducer slightly improves the damping performance of the ABH compared to a passive damping layer and, in addition, the external resistor can be tuned to maximise damping over a particular frequency band. Increasing the number of ABHs in the beam has also been shown to provide more damping. However, the addition of shunted piezoelectric transducers did not significantly improve damping at lower frequencies, particularly below the cut-on frequency of the ABH, where

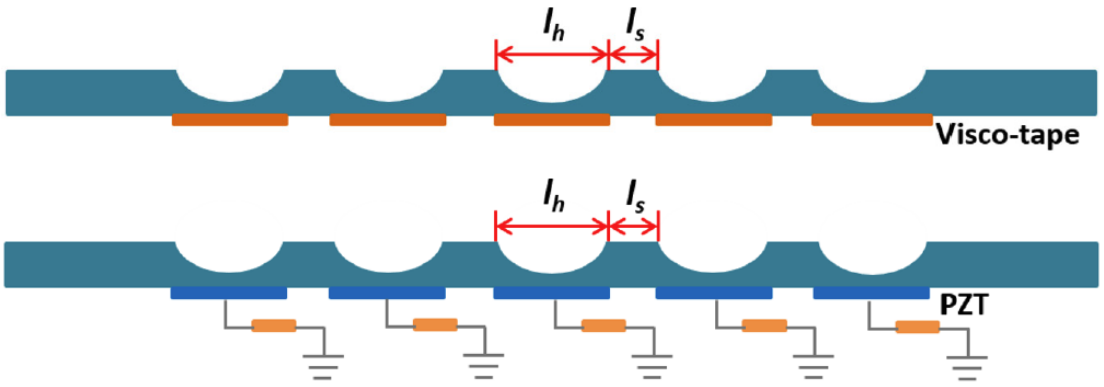

FIGURE 1.11: ABHs with viscoelastic tape attached and ABHs with piezoelectric transducers and external resistors attached [56].

vibration control is still limited. It has also been found that the operating bandwidth of the piezoelectric transducer system is extended due to the wavenumber sweep in the ABH. The wavenumber sweep that occurs along the ABH taper means that waves entering the taper would match the most effective absorbing frequency of the transducer at some point along the taper. This is also the mechanism behind the the use of ABHs for energy harvesting, which is not covered in this literature review. The use of shunted piezoelectric transducers in place of viscoelastic damping material has been studied experimentally in [57], where both the steady state and transient performance were tested.

1.2 Summary and Outlook

The literature review presented in this chapter covers a broad range of investigations into different passive ABH designs. It is clear from this review that although there are a lot of innovative ABH designs, their performance is generally limited at lower frequencies where the performance of the ABH is dependent on the local taper modes [4, 27, 29, 43, 45, 56]; this will be further demonstrated in Chapter 2. It has also been highlighted in this literature review that the addition of piezoelectric patches to ABHs can been used for both energy harvesting and semi-active damping and this offers a potentially enhanced performance, however, fully-active control strategies have not yet been investigated.

Active vibration control (AVC) is a well established method of control that can be used to reduce the vibration of a mechanical system by modification of the system's structural response [1]. AVC is commonly implemented when equivalent passive solutions would exceed limitations on the mass or size of the structure, making it a lightweight and compact control solution. It can sometimes be problematic to implement AVC at higher frequencies due to the spatial matching that is required between the primary

and secondary sources, which is easier achieve when the wavelength is longer. Therefore, AVC can be considered a logical and lightweight solution to the low frequency limitations of ABHs and the two damping strategies, ABHs and AVC, complement each other very well.

1.3 Thesis Structure and Objectives

The objective of the work presented in this thesis is to overcome some of the performance limitations of ABHs through the design and integration of active control technologies. Initially, an investigation has been carried out to determine how three key design parameters can be used to design an ABH with practical dimensions. Piezoelectric components have then been integrated into the ABH to address the performance limitations of the passive system that were identified in the parametric study. The performance of an active ABH (AABH), including its energy and computational requirements, has then been investigated to determine whether the AABH provides advantages over a conventional active control design. The structure of this thesis is organised as follows.

Chapter 2

The objective of the work presented in this chapter is to investigate the design and performance of a passive ABH beam termination. A finite element (FE) model has been used to perform a parametric study where the tip height, taper length and power law of the ABH termination have been varied over practical ranges. The reflection coefficient has then been calculated for each configuration and frequency bands of low reflection have been observed, which are dependent on the design parameters. A modal analysis has also been carried out using the FE model to explain the spectral variation in the reflection coefficient. The magnitude of the local minima within the bands of low reflection have been seen to be dependent on the design, which lead to an investigation into the tradeoff between the design parameters. This investigation shows how the power law and tip height could be selected to minimise the broadband reflection from an ABH. An experimental validation has then been performed.

Chapter 3

In this chapter, the ABH designed in Chapter 2 has been taken and active control technologies have been integrated into the ABH to investigate the benefits of an AABH termination compared to a more conventional constant thickness active termination. A

wave-based feedforward active control strategy is presented that can be used to control the reflected wave, and hence the reflection coefficient of the AABH. Offline active control has been performed to assess the performance of the AABH in terms of the reflection coefficient and also in terms of the energy and computational requirements. The wave-based control strategy has also been implemented using a constant thickness active termination so that a comparison can be made. The AABH termination has been shown to provide more attenuation than the constant thickness active termination, requires a shorter filter to accurately model the plant response and takes less energy to implement. However, it has also been shown that this control strategy produces a significant enhancement of the vibration in the AABH that is not present in the constant thickness active termination. An experimental validation is performed for each configuration.

Chapter 4

To further investigate the relationship between the reflection from the AABH taper and the local vibration in the AABH, the work in this chapter presents the application of a tonal remote damping feedback control strategy using an AABH. A selection of feedback compensators have been calculated using a geometric approach that allows a local feedback loop to be used to control both the local taper vibration and the reflected wave component simultaneously. The compensators have been implemented in the frequency domain and the results provide insight into the connection between the vibration of the taper and the reflection from the AABH. It has also been shown that a compensator can be calculated with constraints on enhancing either the reflected wave component or the local taper vibration. A time domain implementation is then presented to back up the frequency domain results.

Chapter 5

Using the findings of the previous chapters, the work presented in this chapter extends the AABH concept to multiple AABHs embedded into a plate and a comparison is presented between the plate with embedded AABHs and a constant thickness plate with active components. The plates have been individually mounted on a box and clamped on all sides. Embedding AABHs has been shown to reduce the overall mass of the plate and additionally dampens vibration above 2 kHz. A multichannel feedforward active control strategy is then presented that can be used to control the vibration of the plate below 2 kHz. Offline active control has been performed on each plate and it has been shown that embedding AABHs reduces the energy required for control. However, the plant modelling requirements and the attenuation achieved from control is similar for

both plates, which has been attributed to the high level of damping caused by clamping the plates. Up to 10 kHz, it is shown that embedding AABHs provides significant damping over the full frequency range, whereas the constant thickness active plate is only effective over the actively controlled bandwidth.

Chapter 6

The final chapter in this thesis gives a summary of the research presented in the previous chapters, including a contextualisation within the current field of ABHs. The key results and conclusions from each of the preceding chapters have been drawn together and their significance within the field of ABHs has been discussed. Finally, some suggestions are provided for further research in the field of AABHs.

1.4 Contributions

The main contributions of this thesis are listed below.

1. A detailed parametric study of an ABH termination on a beam, including a modal analysis, which provides new insight into how the tip height and power law can be selected to minimise narrow and broadband reflection [58, 59].

2. The proposal of the active acoustic black hole (AABH) concept, where an actuator is attached to the ABH to provide both passive damping and active control [60]. Through the implementation of a wave-based feedforward control strategy, it is shown that an AABH beam termination outperforms a constant thickness active beam termination in terms of reflection control, electrical power requirements and computational demand [61–63].

3. The implementation of a remote damping feedback active control strategy using an AABH beam termination that provides further insight into the relationship between controlling reflection, thus improving the performance, and controlling taper vibration, thus reducing the stresses that cause structural fatigue [64].

4. Extension of the AABH concept to a plate, encompassing multiple AABHs and thus a multichannel system. It is shown that coupling the passive damping of the ABHs at higher frequencies with active control at lower frequencies provides a higher level of damping over a significantly wider bandwidth than achievable via a constant thickness plate with active elements and requires less electrical power to implement.

Chapter 2

A Parametric Study of a Passive Acoustic Black Hole Termination

Previously, in the introductory chapter of this thesis, it has been shown that the performance of an ABH can be modified by varying the taper length, tip height and power law [4]. However, if using an analytical model, the bandwidth over which the first order WKB approximation is valid has been shown to quickly decrease as the power law is increased [19]. As a result, it has been shown that, whilst the taper length should be maximised and the tip height minimised, the power law can be selected to reach an optimal tradeoff between performance and WKB validity [21]. Further insight into the performance of ABHs with higher power law profiles has been shown in [22], where a higher order WKB model has been used to show how tapers with higher power laws, which were penalised in [21] due to violation of the smoothness criterion, physically result in significant reflection from the junction between the uniform section of the beam and the taper due to the rapid impedance change at this point [20, 22]. Similar results have been shown using finite element models, and investigations have focussed on either a specific design parameter [28, 65], or considered only a small number of design cases over frequency or a parameter sweep at a specific frequency [29, 56, 66, 67]. Flexural waves have been solely considered in the majority of the literature because they generally dominate the structural response of beams. Reducing the energy of the flexural waves is, therefore, desirable for effective noise control [15, 16, 68] and this study will continue to focus solely on flexural waves.

To provide more detailed insight in to the effect that varying the geometrical design parameters has on the performance of an ABH termination, this chapter contains an extended parametric design study, which considers the influence of the tip height, taper length and power law on the ABH reflection coefficient over a broad frequency range. The results from this study are complemented by a corresponding modal analysis, which builds on previous work that has demonstrated the link between the ABH

performance and the modal density [29]. This work also builds upon the link between the bands of low reflection and the local modes of the ABH cell [69], by highlighting in detail how the local modes of the ABH are influenced by the geometrical design parameters. Furthermore, using the data from the full parametric design sweep, it is shown how ABHs can be designed for narrowband performance. In particular, it is shown that there are local minima in the bands of low reflection that are dependant on both the design parameter and frequency. The results from the investigations into each individual design parameter have fed into an investigation into how the geometrical parameters should be selected for optimal broadband performance, which is particularly useful when selecting the optimum power law for an ABH design with practical constraints on the taper length and tip height, but also shows new insight into the selection of the tip height.

A parametric study has been chosen for this investigation rather than a direct optimisation procedure as, for example, highlighted in [66], to enable the intricate effects that each design parameter has on the reflection coefficient of the ABH over a broad frequency and parameter range to be examined. Although this parametric study may ultimately be used to assess the optimal set of design parameters, it is not restricted to a specific optimisation cost function and, therefore, is able to provide broader insight. A Finite Element (FE) model has been used to carry out this study, rather than a higher order analytical model, because it could be easily extended for future investigations. Many practical structures can be modelled using FE. A computer aided design is first created and then material properties and pre-built physics packages can be applied to the structure. The presented parametric study considers an ABH termination on one end of a beam, as shown in Figure 2.1.

The structure of this chapter is as follows. Initially, the geometry and physical properties of the modelled beam with an ABH termination are presented in Section 2.1 and followed by a discussion of the meshing procedure in Section 2.1.1. A wave decomposition method is then presented in Section 2.2, which outlines how the generated data can be used to calculate the reflection coefficient of the modelled ABH termination. Section 2.3 presents the results from the parametric study for each individual design parameter and this section ends with an investigation into the performance tradeoffs that arise between the design parameters. The results are accompanied by a discussion about optimal design when one or more of the parameters are limited, for example due to practical design constraints. Section 2.4.2 presents an experimental validation of the simulation results and finally, Section 2.5 presents the conclusions from this investigation and summarises the key findings.

2.1 Model Description

The FE model presented in this section has been implemented using COMSOL Multiphysics. Timoshenko beam theory and the beam physics module have been used, which neglects torsional and compressional waves. In this physics module, the beam and taper can be defined as a 2D cross-section and are given a finite width. The model can then be solved for a one-dimensional flexural wave and the reflection coefficient of the ABH termination can be calculated. A 3D model was also implemented to validate the accuracy of the 1D model over the considered frequency range, however, due to the high computational requirements the 3D model was not used for the full parametric study. Although modelling an ABH in this way neglects torsional modes and flexural modes across the width of the beam, it allows a comprehensive parametric study to be carried out within practical computational limitations. One-dimensional models have been successfully utilised in the study of ABHs in work such as [20, 69]. A diagram of the model geometry is shown in Figure 2.1 and the range of each parameter studied is detailed in Table 2.1. In this parametric study, the geometry of the beam, which has the ABH termination on one end, has been kept constant. That is, the beam height, width and length defined in Table 2.1 do not change throughout this investigation. The geometrical properties of the ABH termination (excluding its width) are, however, varied over practical ranges, as also detailed in Table 2.1. The sampling resolution of each of the ABH parameters is also included. Although a variety of taper profiles have been investigated in the literature [4, 22], the differences in performance are relatively small. Therefore, in this study, a power law profile has been assumed and the height function in this case can be defined as

$$h(x) = \varepsilon \left(\frac{x_{max} - x}{x_{max}} \right)^{\mu} + h_{tip}, \tag{2.1}$$

where $\varepsilon = h_{beam} - h_{tip}$ is a scaling factor, x is the position along the taper, μ is the power law of the taper that defines the gradient and h_{tip} is the tip height at the end of the taper.

TABLE 2.1: The parameters used in the model geometry.

Parameter	Symbol	Value / Range of Values	Sampling Resolution
Beam height	h_{beam}	10 mm	n/a
Beam length	l_{beam}	300 mm	n/a
Beam/ABH width	b	40 mm	n/a
ABH tip height	h_{tip}	0.01 mm – 3 mm	6.67×10^{-3} mm
ABH taper length	l_{abh}	10 mm – 300 mm	2 mm
ABH power law	μ	1 – 10	0.1
Excitation force	$\mathbf{F}$	1N	n/a
Sensor separation	Δ_x	20 mm	n/a

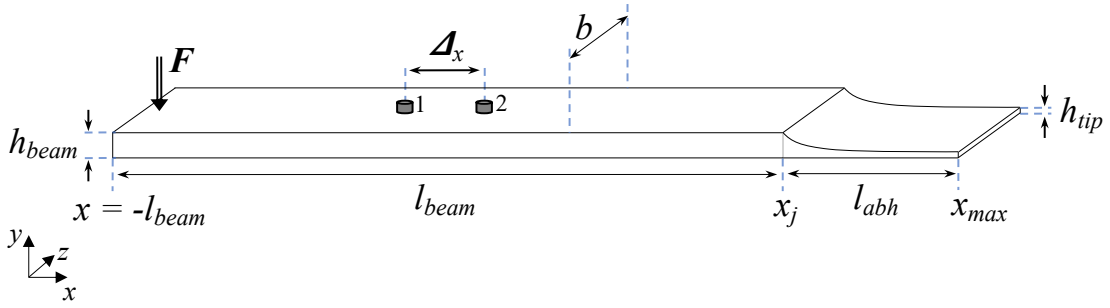

FIGURE 2.1: A diagram of the modelled beam with an ABH termination. The locations of the force excitation and sensors are also indicated.

In addition to the geometrical parameters, Figure 2.1 also shows the position of two sensors on the beam, separated by Δ_x, and a point force, which corresponds to a symmetrically located excitation with respect the width of the beam. The sensors were positioned midway along the beam section for the extraction of the reflection coefficient, which will be discussed in Section 2.2. The length of the uniform beam was chosen to be sufficient such that evanescent components could be neglected in the analysis, as will be discussed in Section 2.2. The beam and ABH were both assumed to be constructed from aluminium alloy 6082-T6 and some hysteretic damping has been implemented as an isotropic loss factor with a value of $\eta_{Beam} = 0.0001$, which is consistent with other studies [41, 43, 66] and will also be cross-validated via experimental results in Section 2.4.2. To model the additional damping layer required on the taper of the practical ABH, further damping was included in the ABH by applying a separate, additional, isotropic loss factor of $\eta_{ABH} = 0.2$ and the additional mass of this damping layer was modelled by an evenly distributed mass of 11.9 g along the length of the taper. This damping, and the additional mass associated with it, were calculated to match the damping layer used in the experimental implementation discussed in Section 2.4. The addition of damping material to the ABH also changes the rigidity along the taper. Although the rigidity change associated with this damping layer could be included in the model by modifying, for example, the Young's modulus of the taper, it was not required in order to achieve a good match between the experimental and modelled results. The boundary conditions of all the edges were set to free and the initial state of the ABH was set to stationary. A picture of the completed model from COMSOL can be seen in Figure 2.2

2.1.1 Model Meshing and Convergence Study

Typically, a minimum of 6 finite elements should be used per wavelength when constructing an FE model [70]. However, in an ABH the wavelength varies along the length of the tapered section and, therefore, some care must be paid to meshing the ABH. To determine the specific meshing requirement for the ABH, a convergence study was

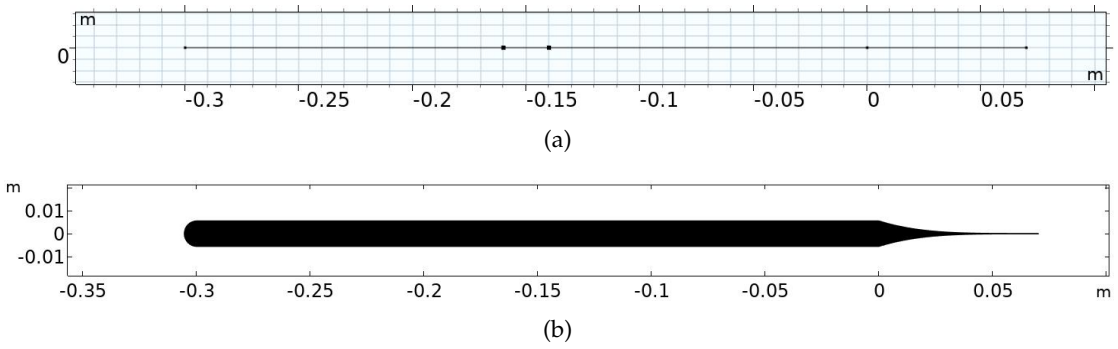

FIGURE 2.2: Two pictures of the beam with an ABH termination in COMSOL. (a) shows the input design and (b) shows the modelled geometry.

performed with the number of elements per wavelength ranging from 1 to 20. Edge elements were used as required by the beam physics module in COMSOL and, to ensure that the minimum number of elements per wavelength was realised at all points in the ABH, the elements were linearly spaced and the mesh resolution was calculated from a reference wavelength taken from the tip of the ABH, where the wavelength is shortest. The wavelength in the tip of the ABH can be calculated by first recounting from Chapter 1 the expression for the flexural wavenumber, which after setting $h(x) = h_{tip}$ can be written as

$$k_{tip} = \left(\frac{12\rho\omega^2}{Eh_{tip}^2} \right)^{\frac{1}{4}}, \tag{2.2}$$

which rearranging for λ_{tip} gives

$$\lambda_{tip} = \frac{2\pi}{k_{tip}} = \left(\frac{4Eh_{tip}^2\pi^4}{3\rho\omega^2} \right)^{\frac{1}{4}}. \tag{2.3}$$

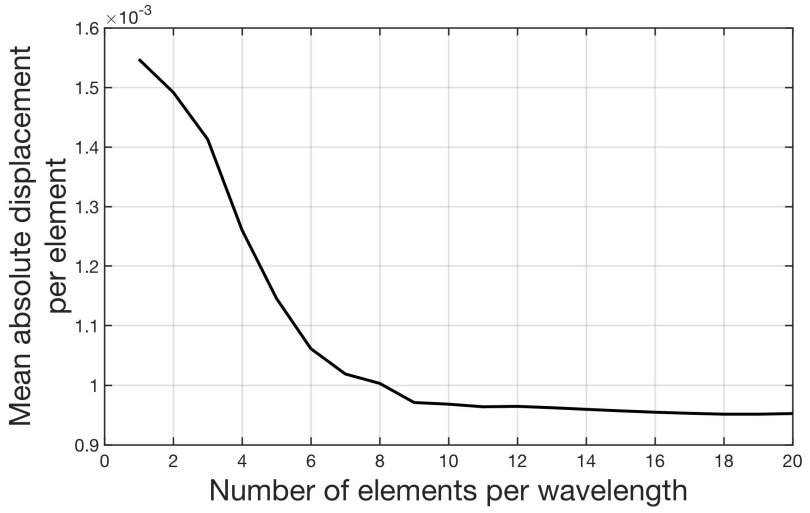

FIGURE 2.3: The mean absolute displacement in the taper plotted against the number of elements per wavelength at 10 kHz.

To guarantee that the meshing procedure was sufficient for the full parameter sweep, a mesh convergence study has been conducted for the longest taper (300 mm), smallest tip height (0.01 mm) and a power law of $\mu = 10$, which gives the largest variation in the wavelength along the taper within the considered parameter range. To assess the convergence, the model was solved at a frequency of 10 kHz, which is the upper frequency of interest, for an increasing number of elements per wavelength. The mean absolute displacement in the ABH was calculated by taking the sum of the absolute displacements measured at each element in the taper and dividing by the number of elements in the taper. The results from this study are shown in Figure 2.3 and, from these results, it can be seen that the mean absolute displacement per element has converged to a constant value when there are approximately 10 or more elements per wavelength. A convergence study was also carried out to ensure that a sufficient number of elements were used to model the uniform beam section, which is constant over the various parameterisations of the ABH and 10 elements per wavelength were used. Therefore, 10 elements per wavelength have been used for both the beam mesh and the taper mesh in the following parametric study.

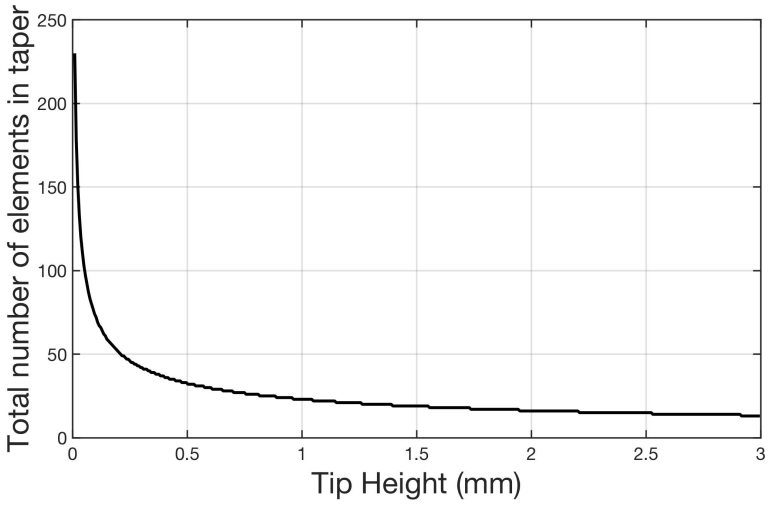

FIGURE 2.4: The number of elements required to model a 70 mm taper with a power law of 10 for each tip height increasing from 0.01 mm to 3 mm with 10 elements per wavelength at a 10 kHz excitation frequency.

Based on the results of the convergence study, Figure 2.4 shows how the total number of elements required to model the taper section varies with the tip height at the maximum frequency of interest in the following study, which is 10 kHz. From this plot it can be seen that the number of elements required rapidly decreases as the tip height increases. In the beam section, a total of 32 elements were required at the upper frequency of interest.

2.2 Wave Decomposition in a Beam

Wave decomposition is the separation of a measured disturbance into the individual wave components. Examples of wave decomposition can be found in the literature for both acoustic systems [71], and structures such as beams [72, 73]. Wave decomposition has also been performed on a beam with an ABH termination in order to estimate the reflection coefficient [27]. This section will present a wave decomposition method, based on [27], which will be used to investigate the performance of the ABH and facilitate a comparison between different ABH designs.

In order to perform a wave decomposition, the number of sensors required is dependant on the number of wave components that make up the disturbance. For example, if there are positive and negative travelling near-field and far-field waves, four sensors are required so that four simultaneous equations can be formed. These four equations can be manipulated so that the amplitude and phase of each of the wave components can be estimated. Although multiple wave components can be separated, solving the simultaneous equations requires a matrix inversion, that can cause problems if the matrix is ill-conditioned. This can occur if the sensor spacing is too small or close to a half-wavelength. In addition, increasing the number of wave components considered in the decomposition reduces the determinant of the matrix and these factors can result in a matrix that is close to being singular (i.e. if its determinant is zero and the matrix does not have an inverse) [1, 72]. It is, therefore, convenient to place the sensor array a sufficient distance from any impedance changes or input forces, so that the contribution from the near-field waves can be neglected. In this case, only two sensors are required and the two simultaneous equations can be solved without singularity issues. Further information about wave decomposition in the presence of a near-field, including the limitations associated with solving the inverse problem, can be found in [72, 74, 75].

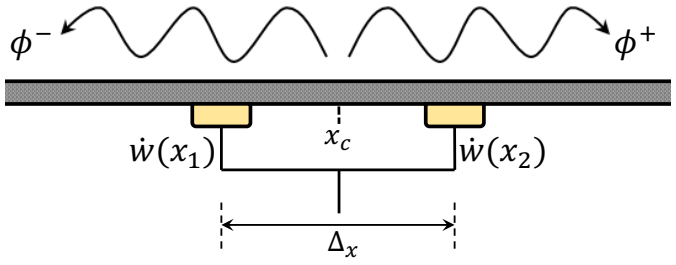

FIGURE 2.5: Two sensors placed at x_1 and x_2 that are used to measure the velocity, $\dot{w}$, at each respective point. The sensors are centred on a mid-point, x_c, and are separated by Δ_x. The velocity measured at each sensor can be used to calculate ϕ^- and ϕ^+, the positive and negative travelling propagating waves along the beam.

A diagram of the beam section of the model is shown in Figure 2.5 indicating the sensing points and the two propagating waves. It has been assumed in the following investigation that the near-field contribution can be neglected once it has decayed to 10% of

its original magnitude, i.e.

$$e^{-kl} = 0.1, \tag{2.4}$$

where l is the distance from the sensor array to any features, such as impedance changes, that introduce near-field components and k is the flexural wavenumber. This percentage decay is consistent with previous studies [27] and corresponds to a 20 dB reduction in the near-field wave components. To address the limits that this assumption imposes on the location of the sensor array, the flexural wavenumber,

$$k = \left(\frac{12\rho\omega^2}{Eh_{beam}^2} \right)^{\frac{1}{4}}, \tag{2.5}$$

is first considered. Substituting Equation 2.5 into Equation 2.4 and rearranging gives the low frequency limit as

$$f_{min} = \frac{1}{l^2} \left(\frac{Eh_{beam}^2 (\ln(0.1))^4}{48\rho\pi^2} \right)^{\frac{1}{2}}. \tag{2.6}$$

In addition, an upper frequency limit due to aliasing can be calculated by considering the requirement that the distance between the two sensors must be less than half a wavelength. An expression for the upper frequency limit can be derived expressing the flexural wavenumber as

$$k = \frac{2\pi}{\lambda}, \tag{2.7}$$

and equating this to the expression given in Equation 2.5. This leads to an expression for the flexural wavelength, which can be written as

$$\lambda = \frac{2\pi}{k} = \left(\frac{4\pi^4 Eh_{beam}^2}{3\rho\omega^2} \right)^{\frac{1}{4}}. \tag{2.8}$$

Because the sensor separation should not exceed $\lambda/2$, Δ_x can be substituted in place of $\lambda/2$ and Equation 2.8 can be rearranged to express the upper frequency limit as

$$f_{max} = \frac{1}{\Delta_x^2} \left(\frac{Eh^2\pi^2}{48\rho} \right)^{\frac{1}{2}}. \tag{2.9}$$

In the presented study, the sensor array was located at 140 mm from the excitation force and 140 mm from the ABH boundary, so that l = 140 mm and the sensor spacing was set to Δ_x = 20 mm. These parameters give a low frequency limit of approximately 600 Hz and an upper frequency limit of approximately 57 kHz. However, this analysis assumes that the structure behaves as a beam with one-dimensional wave propagation, which will break down when the wavelength becomes comparable to either the width

or height of the beam [27]. Equation 2.9 can, therefore, be revised as

$$f_{max} = \frac{1}{\Delta^2}\left(\frac{Eh^2\pi^2}{48\rho}\right)^{\frac{1}{2}}, \tag{2.10}$$

where Δ represents either the width of the beam, the height of the beam or the distance between the sensors, whichever is the largest distance. In the following study, this limit first occurs where the wavelength becomes comparable to the width of the beam, which is 40 mm, and gives a practical upper frequency limit of approximately 14 kHz. Therefore, to keep within these frequency limits, the following investigation analysis has been limited to a frequency range of 600 Hz to 10 kHz.

Now that the limitations of the wave decomposition have been established, the equations to calculate the positive and negative travelling far-field waves can be derived. Referring to Figure 2.5, each sensor measures the velocity at its location, which is the superposition of the two propagating waves at each point, such that

$$\dot{w}(x_1) = i\omega(\phi^+ e^{-ikx_1} + \phi^- e^{ikx_1}) \tag{2.11}$$

$$\dot{w}(x_2) = i\omega(\phi^+ e^{-ikx_2} + \phi^- e^{ikx_2}), \tag{2.12}$$

where $\dot{w}$ is the transverse velocity measured at x_1 or x_2 and ϕ^+ and ϕ^- are the complex amplitudes of the positive and negative propagating waves respectively [1]. In order to express the wave amplitudes in terms of the velocity measured at each sensor, x_1 and x_2 must first be expressed in terms of the point midway between the two sensors, which will be referred to as x_c. The distance between point x_c and either sensor is thus $x_c \pm \Delta_x/2$, and it follows that $x_1 = x_c - \Delta_x/2$ and $x_2 = x_c + \Delta_x/2$. Using these new expressions, Equations 2.11 and 2.12 can be expanded into matrix form and written in terms of each velocity sensor as

$$\begin{bmatrix}\dot{w}(x_1)\\ \dot{w}(x_2)\end{bmatrix} = i\omega \begin{bmatrix} e^{-ik\left(x_c-\frac{\Delta_x}{2}\right)} & e^{ik\left(x_c-\frac{\Delta_x}{2}\right)} \\ e^{-ik\left(x_c+\frac{\Delta_x}{2}\right)} & e^{ik\left(x_c+\frac{\Delta_x}{2}\right)}\end{bmatrix} \begin{bmatrix}\phi^+\\ \phi^-\end{bmatrix}. \tag{2.13}$$

By inverting the matrix of exponentials, Equation 2.13 can be re-arranged to express the wave amplitudes in terms of the velocity measured at the two sensors as

$$\begin{bmatrix}\phi^+\\ \phi^-\end{bmatrix} = \frac{1}{i\omega\left(e^{ik\Delta_x} - e^{-ik\Delta_x}\right)} \begin{bmatrix} e^{ik\left(x_c+\frac{\Delta_x}{2}\right)} & -e^{ik\left(x_c-\frac{\Delta_x}{2}\right)} \\ -e^{-ik\left(x_c+\frac{\Delta_x}{2}\right)} & e^{-ik\left(x_c-\frac{\Delta_x}{2}\right)}\end{bmatrix} \begin{bmatrix}\dot{w}(x_1)\\ \dot{w}(x_2)\end{bmatrix}. \tag{2.14}$$

By using Euler's identity, and arbitrarily setting $x_c = 0$, the positive and negative propagating wave amplitudes can then be calculated in terms of the velocity at each of the

sensors as

$$\phi^{+} = \frac{-1}{2\omega \sin(k\Delta_x)} \left[\dot{w}(x_1) \mathrm{e}^{\frac{ik\Delta_x}{2}} - \dot{w}(x_2) \mathrm{e}^{\frac{-ik\Delta_x}{2}} \right] \tag{2.15}$$

$$\phi^{-} = \frac{-1}{2\omega \sin(k\Delta_x)} \left[\dot{w}(x_2) \mathrm{e}^{\frac{ik\Delta_x}{2}} - \dot{w}(x_1) \mathrm{e}^{\frac{-ik\Delta_x}{2}} \right]. \tag{2.16}$$

The magnitude of the reflection coefficient can thus be calculated as

$$|R| = \left| \frac{\phi^{-}}{\phi^{+}} \right|. \tag{2.17}$$

This will be used in the following parametric study to investigate the tradeoffs in the design of the ABH beam termination, as shown in Figure 2.1.

2.3 Finite Element Results

In this section, the results from the parametric study of an ABH beam termination are presented. Specifically, the reflection coefficient is studied over a broad frequency range when the tip height, taper length and power law are varied. The reflection coefficient for each parameterisation has been calculated using the method presented in Section 2.2 over a frequency range of 600 Hz to 10 kHz, which is within the upper and lower limits of validity of the wave decomposition method, as discussed in Section 2.2. In addition, for each parameterisation, the local modes of the ABH have been calculated by modelling the ABH in isolation and assuming a no-rotation boundary condition at the junction between the beam and the ABH. The no-rotation boundary condition was found to approximate the modal behaviour of the ABH coupled to the beam section well because in the fully-coupled system, the rotational stiffness of the beam at the ABH junction is much greater than the bending stiffness. The results from this investigation into the different design parameters are presented in the following order. Firstly, the effect that varying the tip height has on the reflection coefficient of the ABH is shown over the frequency range of interest. Secondly, over the same frequency range, the effect of varying the taper length is shown and finally, over the same frequency range, the effect of varying the power law is shown. In each case, the mode shapes are shown as an overlay at the corresponding modal frequencies.

2.3.1 The Effect of the Tip Height

Figure 2.6(a) shows a contour plot of the reflection coefficient plotted as a function of frequency for a range of tip heights from 0.01 mm to 3 mm, which has been chosen to cover practically realisable tip heights. The taper length has been fixed at 70 mm and the power law set to $\mu = 4$. The resolution of the change in the tip height was

decreased iteratively until the results shown in Figure 2.6(a) converged. The tip height was ultimately varied in steps of 6.67 μm, which corresponds to $1/5^{\text{th}}$ of the minimum flexural wavelength.

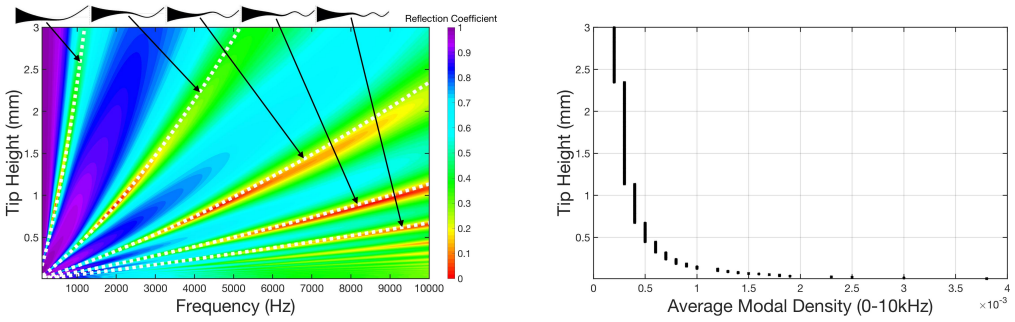

FIGURE 2.6: (a) The reflection coefficient, shown on a colour scale of 0 to 1, plotted as a function of frequency and tip height for an ABH with a taper length of 70 mm and a power law of 4. The modal frequencies are indicated by the white dotted lines and the first five mode shapes are shown. (b) The change in modal density averaged across the considered bandwidth as a function of the tip height.

The results in Figure 2.6(a) show that as frequency increases from 600 Hz to 10 kHz, there are varying bands of high and low reflection coefficient. At larger tip heights, the spectral bands become wider in both bandwidth and spacing and, resultantly, there are fewer bands of low reflection within the presented frequency range. Interestingly, it is also clear that the minima in the spectral bands are lower in the mid-range of tip heights presented and, therefore, if the ABH was being tuned for a narrowband control problem, there may be a benefit to selecting a tip height that is greater than the minimum manufacturable limit; this is distinct from the general ABH design approach. For example, the performance at 7 kHz can be maximised by using a tip height of 0.7 mm. Despite this potential for narrowband tuning, by decreasing the tip height the bands of low reflection begin to overlap and the broadband performance tends to increase; this broadband performance will be explored in more detail in Section 2.3.4.

In addition to the narrowband and broadband performance of the ABHs, it is interesting to consider the low frequency performance limit, which can be determined by evaluating the modes of the ABH. Therefore, to provide further insight into the physical behaviour of the ABH, the modes of the ABH cell have been calculated as described in the introduction to Section 2.3. The variation in the frequency of the first 5 modes of the ABH cell over tip height are shown by the white dotted lines in Figure 2.6(a) and the corresponding mode shapes are shown for the first 5 modes. From these results it can be seen that the frequencies at which the modes occur align well with the bands of low reflection and that at low frequencies the ABH only achieves a low reflection coefficient at frequencies very close to the first mode. It can also be seen from these results that the modal density increases with a decrease in the tip height, which is consistent

with [29] and Figure 2.6(b) shows the change in the modal density averaged across the considered bandwidth as a function of the tip height. From this plot it can be seen that the modal density increases exponentially for a decreasing tip height. The increase in the modal density for smaller tip heights is due to higher order modes occurring at lower frequencies and this can, in turn, be related to the increased reduction in the wavelength over the length of the taper.

2.3.2 The Effect of the Taper Length

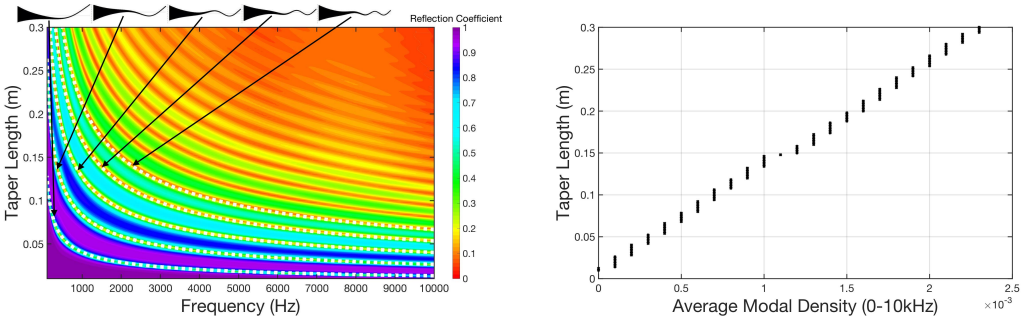

(a) (b)

FIGURE 2.7: (a) The reflection coefficient, shown on a colour scale of 0 to 1, plotted as a function of frequency and taper length for an ABH with a tip height of 0.6 mm and a power law of 4. The modal frequencies are indicated by the white dotted lines and the first five mode shapes are shown. (b) The change in modal density averaged across the considered bandwidth as a function of the taper length.

Figure 2.7(a) shows a contour plot of the reflection coefficient plotted as a function of frequency for a range of taper lengths from 10 mm to 300 mm, which has been chosen to represent practically realisable taper lengths. The tip height has been fixed at 0.6 mm and the power law set to $\mu = 4$. As in the previous section, the resolution of the change in the taper length was decreased iteratively until the results shown in Figure 2.7(a) converged. The taper length was ultimately varied in steps of 2 mm, which corresponds to $1/10^{\text{th}}$ of the minimum flexural wavelength. The results in Figure 2.7(a) show that, as frequency increases, the reflection coefficient of the ABH varies in bands, similarly to Figure 2.6(a). For longer tapers, there are more bands of high and low reflection than for shorter tapers over the same bandwidth. As discussed in Section 2.2, the low frequency limit of the ABH is dependent on the length of the taper and it can be seen from the results in Figure 2.7(a) that the low frequency limit decreases as the taper length is increased. For the considered power law ($\mu = 4$) and tip height ($h_{tip} = 0.6$ mm), when the taper is shorter than 26 mm, the broadband performance of the ABH is limited over the presented frequency range. As in Section 2.2, this can be related to the length of the ABH and a 26 mm taper becomes comparable to the flexural wavelength at a frequency of 10 kHz. At taper lengths below 26 mm it can be seen from Figure 2.7(a) that a dip in the reflection coefficient only occurs over a narrow bandwidth around the

first ABH mode, as discussed in the previous section. That said, considering the relatively small amount of damping assumed in the presented results, it can be seen that ABHs with longer tapers are very effective, especially at higher frequencies, where the reflection coefficient is between around 0 and 0.2 over a large portion of the presented bandwidth.

Once again, the first 5 modes of the ABH cell have been calculated over the range of taper lengths and their frequencies are indicated by the white dotted lines in Figure 2.7(a). From these results, it can again be seen that the modal frequencies correspond to the bands of low reflection. In addition, it can be seen that the modal density increases as the taper length increases and this is clearly shown by Figure 2.7(b), which shows the average modal density as a function of the taper length. From this plot, it can be seen that the average modal density increases linearly with the taper length, resulting in improved performance for longer tapers.

2.3.3 The Effect of the Power Law

The final geometrical parameter that can be tuned when designing an ABH for a beam application is the power law. In fact, in many applications this may be the main design parameter due to restrictions on tip height, due to manufacturing and structural integrity requirements, and taper length, due to the space available for the ABH. Figure 2.8(a) shows a contour plot of the reflection coefficient plotted as a function of frequency for a range of power laws from 1 to 10. The taper length has been fixed at 70 mm and the tip height has been set to 0.6 mm. In this case, the power law has been varied in steps of 0.1, which has been determined iteratively, as in the previous sections.

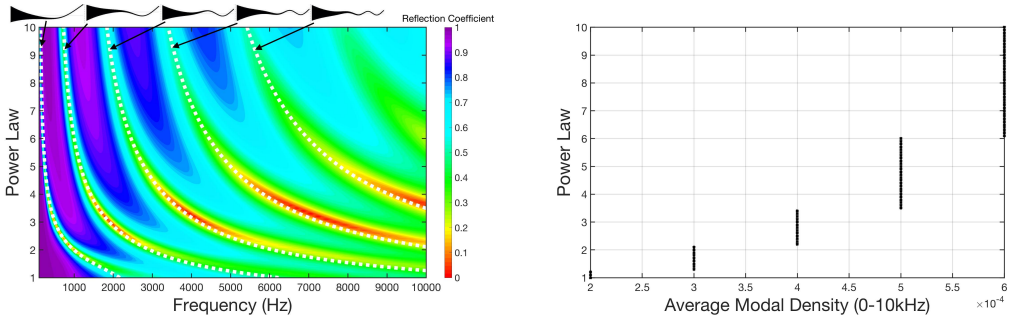

(a) (b)

FIGURE 2.8: (a) The reflection coefficient, shown on a colour scale of 0 to 1, plotted as a function of frequency and power law for an ABH with a tip height of 0.6 mm and a taper length of 70 mm. The modal frequencies are indicated by the white dotted lines and the first five mode shapes are shown. (b) The change in modal density averaged across the considered bandwidth as a function of the power law.

From the results presented in Figure 2.8(a) it can be seen that the spectral bands of high and low reflection, observed previously, also vary with the taper power law. At higher

frequencies, on average, the reflection coefficient is lower for all power laws and this is consistent with the previous results and literature. Figure 2.8(a) once again shows the alignment between the modal frequencies of the ABH and the bands of low reflection for the range of power laws examined. A higher power law changes the mass distribution of the taper and can be seen to lower the modal frequencies and thus increase the modal density over the presented frequency range. This is also shown by the average modal density versus power law, which is shown in Figure 2.8(b). From this plot it can be seen that the modal density increases exponentially with the power law. In addition to the changes in the modal frequencies, it can be seen from the results shown in Figure 2.8(a) that for power laws less than around 5, the minima in the spectral bands are lower than for higher power laws. For example, in the band corresponding to the third mode, the reflection coefficient is lowest for a power law between 3 and 5. There thus exists an optimal power law, which reaches a tradeoff between the large impedance change between the beam and the taper at higher power laws, and the limited length of the taper over which the wave speed is relatively slow at lower power laws. That is, the reflection at higher power laws becomes dominated by the component reflected from the junction to the ABH rather than from the ABH itself, as demonstrated in [22], and it can be seen from the results in Figure 2.8(a) that this is a frequency dependent effect.

Based on the above discussion and the results in Figure 2.8(a), it is evident that there is an optimum power law that can be used to attenuate a particular frequency. For example, if attenuation is required at 7 kHz and the ABH has been constrained to a length of 70 mm and a tip height of 0.6 mm, the optimum power law would be 3.3. This demonstrates that the power law can be used to tune the behaviour of an ABH when the other geometrical design parameters, namely the length and tip height, are constrained due to practical restrictions.

In the previous sections, the eigenfrequencies corresponding to the local ABH modes are complex and the imaginary part of each eigenfrequency is approximately 10 times smaller than the real part, representing a damping ratio of approximately 0.1. The real part of the eigenfrequencies has been shown to align well with the bands of low reflection and the mode shape has also been shown for each of these frequencies. Although it hasn't been explored here, the bands of low reflection have been linked to the poles and zeros of the complex eigenvalues [76]. The poles have been shown to correspond to the local ABH modes whilst the zeros have been shown to correspond to destructive interference phenomena [76]. It has also been shown in [76] that when the complex reflection coefficient is plotted, the zeros are shifted towards the real axis when a loss factor is present in the ABH. Critical coupling between the beam and the ABH occurs when sufficient loss is present in the ABH, such that the zeros lie on the real axis. At frequencies where this arises, the impedance is matched between the beam and the ABH, leading to significant absorption of the incident wave [76]. Further in-depth analyses

of the relation between the complex eigenfrequencies and the local modes of the ABH taper can be found in [76].

2.3.4 Parameter Selection for Optimal Design

It has been shown in the previous sections that the geometrical parameters of an ABH can be tuned to achieve a change in its performance characteristics. In particular, it has been discussed how the parameters can be tuned to optimise the ABH for performance at a single frequency or over a narrow band. However, the ABH design parameters could also be tuned to minimise the reflection over a broadband frequency range and in this case the optimal parameters will depend on both the bandwidth of interest and the constraints due to the application. In this section, the potential design tradeoffs are considered for the case when the maximum broadband performance of the ABH is required and the optimal design parameters will be evaluated. The broadband performance has been assessed over a frequency range of 600 Hz – 10kHz by calculating the average reflection coefficient for each combination of design parameters, and the minimum broadband reflection coefficient over the parameter space has been evaluated.

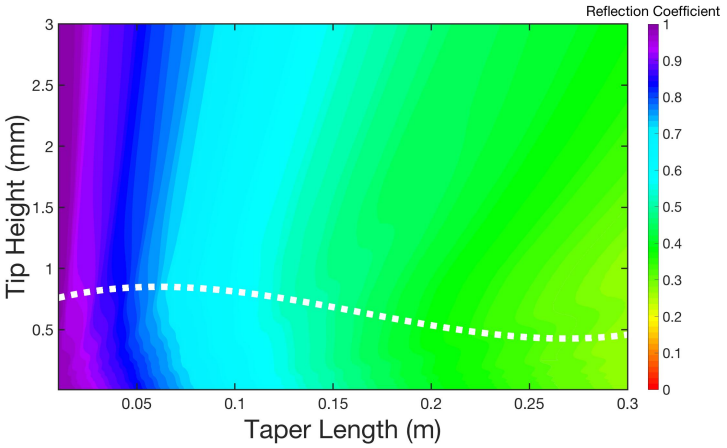

FIGURE 2.9: The variation in the broadband average reflection coefficient with both the tip height and taper length of an ABH with a power law of 4. The reflection coefficient has been averaged over a broadband frequency range (600 Hz – 10 kHz) and is shown on a colour scale of 0 to 1. The optimum tip height is shown by the dotted white line.

In the first instance, Figure 2.9 shows how the broadband average reflection coefficient varies with both taper length and tip height for an ABH with a power law of 4. From these results it can be seen that increasing the taper length lowers the broadband average reflection coefficient for this power law. The optimal configuration is thus relatively trivial in this case, essentially requiring the longest taper length achievable. That said, for each taper length there is an optimum tip height and it is, therefore, insightful to discuss the behaviour further. For the parameter ranges examined, it is clear that the optimum tip height, which minimises the broadband reflection coefficient for a specific

taper length, varies with taper length. This is shown by the dotted white line in Figure 2.9 and is generally lower for longer taper lengths. This is somewhat distinct from current ABH design strategies, which specify that reducing the tip height improves the performance of the ABH. This is because, as shown in Section 2.3 for a power law of 4, that although a small tip height gives a higher modal density, the minima in the bands of low reflection are low enough to shift the minimum in the broadband average up to the mid-range tip heights. This may explain the lower optimum tip height at longer taper lengths because, as shown in Section 2.3, increasing the taper length reduces the reflection coefficient at all frequencies and would therefore reduce the difference between the minima in the bands of low reflection in Section 2.3 and the reflection coefficient when the modal density is high. It should be noted then that the optimum tip height for minimising the broadband reflection coefficient may not be suitable for all broadband vibrational problems as there may be cases where the problematic frequencies do not align with the bands of low reflection.

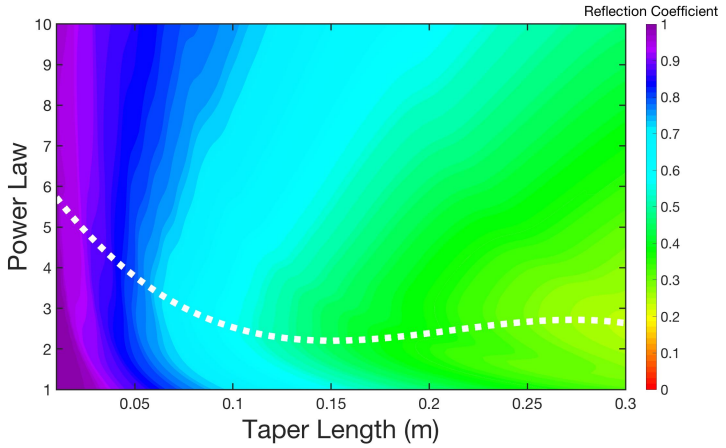

FIGURE 2.10: The variation in the broadband average reflection coefficient with both the power law of the taper and the taper length for an ABH with a tip height of 0.6 mm. The broadband reflection coefficient is shown on a colour scale from 0 to 1. The optimum power law is shown by the dotted white line.

Figure 2.10 shows how the broadband average reflection coefficient varies with both the power law of the ABH and the length of the taper. For a fixed power law, the results show that increasing the length of the taper decreases the broadband average reflection coefficient. As shown in Section 2.3, increasing the length of the taper increases the modal density and, therefore, increases the attenuation provided by the ABH. A more interesting observation from the results presented in Figure 2.10 is, however, that at each taper length there is an optimum power law that can be used to achieve the lowest broadband reflection and this power law has been indicated by the dotted white line. From the indicated optimal results shown in Figure 2.10, it can be seen that the optimum power law varies with taper length. In section 2.3, it was shown that increasing the power law results in an increase in the modal density, but also increases the reflection from the junction between the beam and the ABH. This trade-off differs for

each taper length, due to the corresponding variation in the modal density as discussed in Section 2.3. Specifically, for a long taper with a high modal density, a lower power law is used to limit the impedance change and, therefore, reflection at the junction. Whereas for a shorter taper, with a relatively low modal density, a higher power law provides the optimal trade-off between reflection from the junction and modal density. This trend can be seen from the results presented in Figure 2.10. It is also interesting to note that for taper lengths greater than about 100 mm, the optimum power law is relatively constant with a value between 2 and 3. In summary, the results in Figure 2.10 show that the power law of an ABH can be optimised for a specific taper length to achieve the minimum broadband reflection coefficient. If, in practice, the length of the ABH taper was constrained by the intended application, the power law of the ABH could be optimally tuned according to the data shown in Figure 2.10.

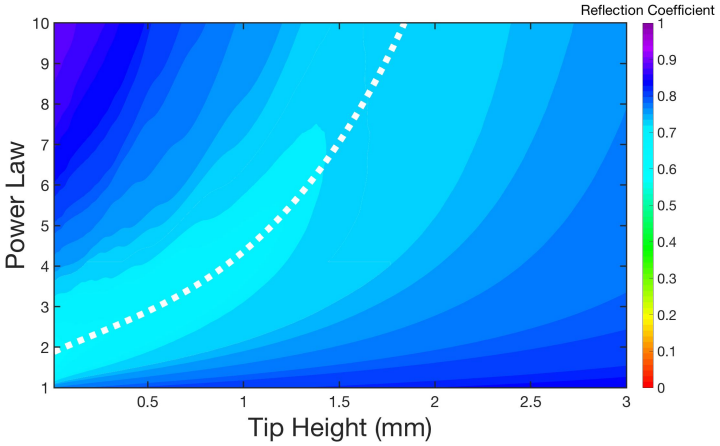

FIGURE 2.11: The variation in the broadband average reflection coefficient with both the power law of the taper and the tip height of an ABH with a taper length of 70 mm. The broadband reflection coefficient is shown on a colour scale from 0 to 1. The optimum power law is shown by a dotted white line.

In addition to considering how the broadband performance varies with both power law and taper length, it is interesting to consider the variation with power law and tip height and this is shown in Figure 2.11. The optimum power law, which minimises the broadband reflection coefficient for each tip height, is shown by the dotted white line. From these results it can be seen that the optimum power law is greater for larger tip heights and this can be related to a shift in the trade-off between modal density and reflection from the junction. That is, when the modal density is limited by the tip height, the benefit of increasing the modal density by using a higher power law outweighs the relative change in the reflection from the junction to the ABH. For smaller tip heights, this balance between the reflection from the junction and the modal density occurs at a lower power law.

The results presented in this section have been calculated using a damping loss factor of $\eta_{ABH} = 0.2$, so that they are consistent with the previous results presented over

frequency. However, if the damping were to be modified the same characteristic behaviour would be expected. Only a small amount of damping is required to achieve the low reflection that occurs when a local taper mode is excited. Therefore, as long as there is damping present, modifying the loss factor of this damping will predominantly affect the frequencies outside of the bands of low reflection. Over frequency, increasing the loss factor will decrease the maxima of the reflection coefficient, bringing them closer to the minima. This effect will be more substantial at higher frequencies, where the shorter wavelengths are more easily damped. There will be, therefore, a point where the damping is high enough that the characteristic behaviour of the ABH is lost above a particular frequency. When the broadband reflection coefficient is calculated, this effect will cause the value of the reflection coefficient to decrease and will reduce the clarity of the optimum configuration, however it will not completely remove the presence of an optimum configuration.

2.4 Experimental Validation

In this section, the reflection coefficient of a practical ABH will be experimentally calculated and presented alongside the experimentally identified modes. These results will be assessed to validate the physical insights provided by the simulation-based study. This experimental study will demonstrate that the practical ABH behaves with the characteristics that were predicted in the simulation study presented in Section 2.3.

2.4.1 Experimental Setup

An ABH on a beam was cut from an aluminium plate, alloy T6, using a water jet and the dimensions are shown in Table 2.2. The tolerance for each parameter is also given in Table 2.2. In most cases, the tolerance is small compared to the value of the parameter and so is not expected to significantly affect the experimental results. However, the tolerance for the power law is 1/10th of its specified value and the tolerance for the tip height is 1/5th of its specified value. By referring to Sections 2.3.1 and 2.3.3, it can be seen that this variation will change the modal frequencies of the ABH, particularly for higher order modes. As a result, the bands of low reflection can vary and so care must be taken when manufacturing ABHs for narrowband applications. The manufactured beam with the ABH termination is shown in Figure 2.12, with and without the additional damping applied to the taper. The damping that was used in this experiment was 'Yellow Plastic Compound', manufactured by WT Henley [77]. The compound is easy to mould and was attached to the aluminium surface without requiring additional adhesive. The structure was then mounted, via a force gauge, onto a large shaker as shown in Figure 2.13. The shaker was driven with white noise, using a sample time of 41.7 μs (corresponding to a Nyquist frequency of 12 kHz).

TABLE 2.2: The dimensions of the manufactured ABH on a beam.

Parameter	Value
Beam height	10 mm $\pm$ 0.1 mm
Beam length	300 mm $\pm$ 0.1 mm
Beam width	40 mm $\pm$ 0.1 mm
ABH tip height	0.5 mm $\pm$ 0.1 mm
ABH taper length	70 mm $\pm$ 0.1 mm
ABH width	40 mm $\pm$ 0.1 mm
ABH power law	4 $\pm$ 0.1
Damping mass	12 g $\pm$ 0.5 g

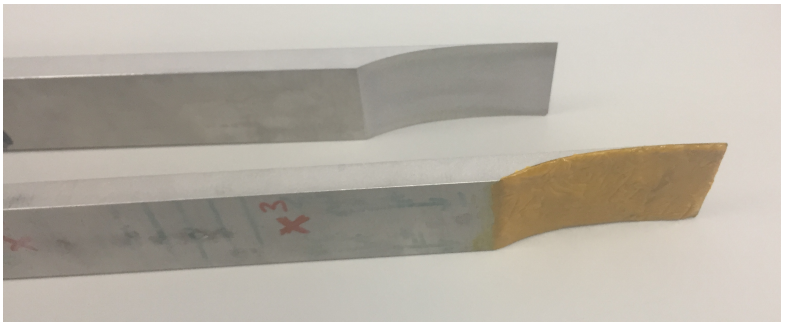

FIGURE 2.12: A picture of the ABH that was used in the experimental study, with and without damping.

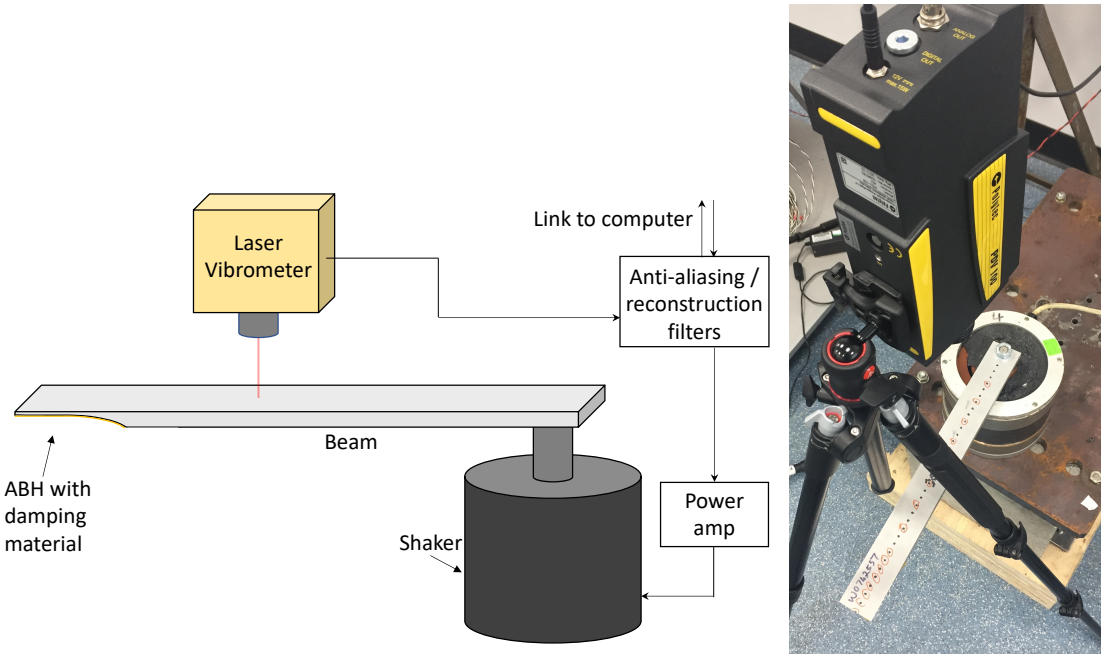

(a) (b)

FIGURE 2.13: A diagram (a) and picture (b) of the experimental setup used.

The resulting vibration of the structure was measured at intervals of 5 mm along the length of the beam and the taper sections using a Polytec PDV–100 laser vibrometer mounted on a tripod 210 mm above the ABH. Each measurement was taken for a duration of 60 s to allow significant averaging to achieve good coherence. 5 mm intervals between measurement points were chosen along the length of the beam and the taper sections so that the modes of the system could be analysed. The reflection coefficient was then calculated using the wave decomposition method described in section 2.2. Similarly to the FE model, a measurement separation of 20 mm was used and each measurement location was at least 140 mm from either the shaker or the ABH junction. Using the same calculation method described in Section 2.2, the lower frequency measurement limit was $\sim$ 600 Hz and the upper frequency measurement limit was $\sim$ 14 kHz. The upper frequency limit has been reduced to 10 kHz due to the anti-aliasing filters used.

2.4.2 Experimental Results

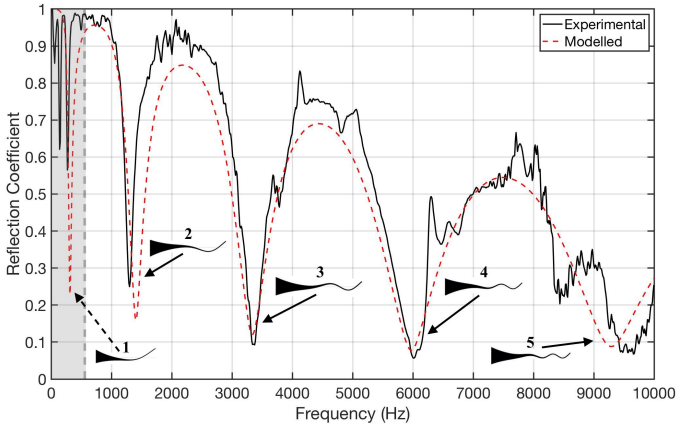

FIGURE 2.14: The reflection coefficient calculated using the experimentally measured velocities from an ABH on a 300 mm beam. The dimensions of the beam and ABH are specified in Table 2.2 and the measured mode shapes at each minima have been plotted. The grey shaded area is the frequency range that the wave decomposition is not necessarily valid. In addition, the reflection coefficient calculated using the FE model is shown.

Figure 2.14 shows the measured reflection coefficient over frequency along with the measured mode shapes of the ABH cell and their frequencies. Minima in the reflection coefficient occur at 1.3 kHz, 3.35 kHz, 6.01 kHz and 9.45 kHz. The modes of the ABH cell were extracted by noting the peaks in the frequency response of the taper and examining the amplitude of the displacement along the taper at these frequencies. These modes have been numbered in Figure 2.14. The first five modal frequencies match the frequencies of the bands of low reflection, with the first mode occurring at approximately 315 Hz. The first mode falls outside of the valid frequency range of the wave decomposition and therefore the reflection coefficient measured at this frequency is not

valid, but is still included for reference. Figure 2.14 also shows FE results for the same ABH design parameters, where the mass and loss factor of the yellow damping material have been matched in the model as discussed in Section 2.1. Although there are slight deviations, the FE results match the experimental results well and validate the insight gained from the model based investigation.

2.5 Summary

The work presented in this chapter contains an extended study of how the controllable geometrical parameters of an ABH influence the reflection coefficient and the broadband average reflection coefficient of a beam. A FE model has been developed and utilised to carry out a parametric design study. In the first instance, the variation in the reflection coefficient over frequency has been investigated as either the tip height, taper length or power law of the ABH are modified. These results have shown that the reflection coefficient exhibits bands of low reflection and, through a modal analysis, these bands have been linked to the modes of the ABH cell. Although the bands of low reflection have been previously related to the modes of the ABH cell [69], this study has demonstrated, over a broad frequency range with a high level of resolution, that as each of the ABH design parameters are varied, the modes of a damped ABH change in frequency and the corresponding bands of low reflection change in both frequency and amplitude. Thus, the finer details of how each design parameter affects the modal frequencies, modal density and reflection coefficient of an ABH have been shown. Specifically, it has been shown that not only are there bands of low reflection, but that there are optimal minima within these bands for certain parameter values. These minima are achieved by selecting the power law and tip height to reach a trade-off between increasing the modal density of the ABH and reducing the reflection from the junction to the ABH. It can therefore be seen that, contrary to previous studies, to achieve optimal performance the ABH design should not necessarily maximise the modal density, which is achieved by using a high power-law and small tip-height.

The results from the initial parametric investigation into each design parameter have also fed into an investigation into the variation in the broadband averaged reflection coefficient when two of the three geometrical design parameters are varied simultaneously. This investigation has initially shown that the broadband average reflection coefficient is minimised by maximising the taper length as expected. However, contrary to current ABH design strategies, the tip height was shown to have an optimum value for a specific ABH parameterisation. In practical applications, the tip height and taper length are likely to be constrained and, therefore, a series of results have also been presented that demonstrate how the power law should be optimally tuned depending on other design constraints. In overview, it has been shown that the optimal power

law decreases with the taper length and increases with the tip height and this observation has been linked to reaching a trade-off between maximising the modal density and limiting the reflection from the junction between the beam and the taper.

In order to validate the findings of the FE model, an experimental case study of an ABH termination on one end of a beam has been performed using one set of design parameters. A thin layer of damping material was applied to the taper to enhance the performance and the structure was driven with broadband white noise as a disturbance. Two sensors were used to decompose the wave components and calculate the reflection coefficient. In addition, the local mode shapes of the ABH cell have been identified by measuring the displacement along the taper at each frequency and the frequencies of these modes have been determined from the peaks in the frequency response of the taper. It has been shown that the bands of low reflection are present in the damped ABH, and that these bands of low reflection align with the experimentally identified ABH modes. These results support the numerical analysis presented and thus serve to validate the findings from the FE model.

In addition to the design study, the results from this parametric investigation also highlight the limited performance of passively damped ABHs at low frequencies, especially when the dimensions of the ABH are constrained in some way. It has been shown that outside of the narrow bands of low reflection, located at the modal frequencies, the reflection remains high, which may be problematic if there are constraints on the design of the ABH or if there are multiple tonal disturbances. The following chapters will use the manufactured ABH from this investigation and build upon the passive damping of the ABH by integrating active components into the taper in order to improve the performance. The following chapter describes the realisation of an AABH and an investigation into the implementation of a feedforward wave-based control strategy is presented, which is used to actively control the reflection coefficient of the ABH termination.

Chapter 3

Feedforward Control using an Acoustic Black Hole Termination

In Chapter 2, and in a variety of the literature [20,22,28,29,47,65–67], it has been shown that an ABH can be designed to minimise reflection passively over a narrow or broad band of frequencies by tuning the taper length, tip height and taper gradient. It has also been shown that these parameters are interdependent and they can thus be optimised when considering different practical limits due to manufacturing or the intended application [19,21,59]. In addition to the investigations into passive tuning, a semi-active method of tuning the damping layer was proposed in [55], in which a thermally controlled material was utilised. Although it was an effective tuning method, it required accurate temperature adjustment which meant that the structure had to be placed in a thermal chamber, therefore limiting the practicality of this tuning method. Another semi-active method for tuning the damping layer has been presented in [56], where the standard viscoelastic damping layer has been replaced by a shunted piezoelectric transducer. In this investigation, the external resistor was changed to alter the damping properties of the piezoelectric transducer.

When implemented passively, or semi-actively, ABHs have been found to have a low frequency cut-on limit and the damping performance is poor below this frequency [43]. The low frequency cut-on limit can be approximated as the frequency at which the flexural wavelength becomes comparable to the taper length [45–47]. Although one solution to lowering the cut-on frequency limit is to increase the taper length, this is not always possible in practical applications where space is limited. One possible solution to overcome a limitation on space has been proposed where a longer ABH can be curled up to form a spiral [30,31]. However, a design such as this is more complex to manufacture and the increased height may make it difficult to integrate into existing structures. An alternative approach to improve the low frequency performance of an ABH is to integrate Active Vibration Control (AVC) technology into the taper. AVC is

an effective solution for the control of structural vibration when there are restrictions on the size and weight of the control treatment [1], and thus presents a complimentary solution to the passive ABH.

This chapter contains a detailed investigation into the realisation of an Active ABH (AABH) when used as a termination on one end of a beam. A feedforward wave-based control strategy that has previously been used in the realisation of an active anechoic beam termination is adopted from the literature [73, 75, 78]. Section 3.1 contains a description of this control strategy in the context of an AABH including wave decomposition, controller formulation and controller limitations. Section 3.2 presents the experimental setup used in this investigation, an investigation into the effect of plant model accuracy, an investigation into the effect of control filter length and the offline and real-time results from the wave-based control. To assess the performance of the AABH, control is also performed on a beam with a constant thickness termination. The chapter is then concluded with a summary of the investigation, which is presented in Section 3.3.

3.1 Wave-Based Active Control

In this section, a wave based control strategy is presented where the objective is to minimise the reflected wave, therefore reducing the reflection coefficient of the termination. This control strategy has been chosen, rather than, say, global control, because it demonstrates the performance enhancements gained by integrating active components whilst also defining the control performance in the same way that passive ABHs have been assessed in a large amount of the literature, via the reflection coefficient.

3.1.1 Wave Decomposition in the Time Domain

It has previously been shown in Section 2.2 that, in the frequency domain, a disturbance can be decomposed into its individual wave components. This section will initially refresh how wave decomposition is performed in the frequency domain, using acceleration rather than velocity, and then extend this to the time domain. It will be assumed that the sensor array is positioned so that the near field waves can be considered negligible. This assumption can be made once the amplitude a near field wave has decayed to 10 % of its original amplitude [27, 59], which can be calculated as a 20 dB reduction with respect to the original level. The limitations that this assumption imposes on wave-based control have been previously discussed in Section 2.2 and will be addressed for the AABH experimental setup in Section 3.2.1. In order to decompose a far field disturbance into its positive and negative travelling wave components, two sensors are required. Figure 3.1 shows two accelerometers on a beam, separated by Δ_x

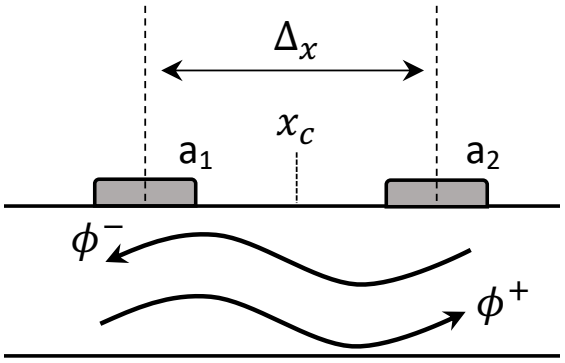

FIGURE 3.1: Two accelerometers placed on a beam, separated by distance Δ_x, which can be used decompose the disturbance within the beam into two far field wave components.

and centred at the point x_c. In the frequency domain, the amplitude of the disturbance measured at each accelerometer can be expressed as

$$\begin{bmatrix} a_1(\omega) \\ a_2(\omega) \end{bmatrix} = -\omega^2 \begin{bmatrix} e^{-ik\left(x_c-\frac{\Delta_x}{2}\right)} & e^{ik\left(x_c-\frac{\Delta_x}{2}\right)} \\ e^{-ik\left(x_c+\frac{\Delta_x}{2}\right)} & e^{ik\left(x_c+\frac{\Delta_x}{2}\right)} \end{bmatrix} \begin{bmatrix} \phi^+(\omega) \\ \phi^-(\omega) \end{bmatrix}, \tag{3.1}$$

where k is the flexural wavenumber and ω is the angular frequency. Equation 3.1 can be simplified to

$$\begin{bmatrix} a_1(\omega) \\ a_2(\omega) \end{bmatrix} = -\omega^2 \begin{bmatrix} e^{ik\frac{\Delta_x}{2}} & e^{-ik\frac{\Delta_x}{2}} \\ e^{-ik\frac{\Delta_x}{2}} & e^{ik\frac{\Delta_x}{2}} \end{bmatrix} \begin{bmatrix} \phi^+(\omega) \\ \phi^-(\omega) \end{bmatrix} \tag{3.2}$$

if it is assumed that the arbitrary location $x_c = 0$. The matrix containing exponentials in Equation 3.2 can be inverted to obtain an expression for the positive and negative wave amplitudes,

$$\begin{bmatrix} \phi^+(\omega) \\ \phi^-(\omega) \end{bmatrix} = -\frac{1}{\omega^2\left(e^{ik\Delta_x} - e^{-ik\Delta_x}\right)} \begin{bmatrix} e^{ik\frac{\Delta_x}{2}} & -e^{-ik\frac{\Delta_x}{2}} \\ -e^{-ik\frac{\Delta_x}{2}} & e^{ik\frac{\Delta_x}{2}} \end{bmatrix} \begin{bmatrix} a_1(\omega) \\ a_2(\omega) \end{bmatrix}. \tag{3.3}$$

Equation 3.3 can be simplified to give an expression for the amplitude of each of the individual wave components,

$$\phi^+(\omega) = -\frac{e^{ik\frac{\Delta_x}{2}}}{\omega^2\left(e^{ik\Delta_x} - e^{-ik\Delta_x}\right)} a_1(\omega) + \frac{e^{-ik\frac{\Delta_x}{2}}}{\omega^2\left(e^{ik\Delta_x} - e^{-ik\Delta_x}\right)} a_2(\omega) \tag{3.4}$$

$$\phi^-(\omega) = \frac{e^{-ik\frac{\Delta_x}{2}}}{\omega^2\left(e^{ik\Delta_x} - e^{-ik\Delta_x}\right)} a_1(\omega) - \frac{e^{ik\frac{\Delta_x}{2}}}{\omega^2\left(e^{ik\Delta_x} - e^{-ik\Delta_x}\right)} a_2(\omega), \tag{3.5}$$

which, using Euler's formula, can be written as

$$\phi^+(\omega) = h_-(\omega)a_1(\omega) + h_+(\omega)a_2(\omega) \tag{3.6}$$

$$\phi^-(\omega) = h_+(\omega)a_1(\omega) + h_-(\omega)a_2(\omega), \tag{3.7}$$

where

$$h_{-}(\omega) = \frac{-\mathrm{i}}{4\omega\cos(k\Delta_x/2)} - \frac{1}{4\omega\sin(k\Delta_x/2)} \tag{3.8}$$

$$h_{+}(\omega) = \frac{-\mathrm{i}}{4\omega\cos(k\Delta_x/2)} + \frac{1}{4\omega\sin(k\Delta_x/2)}. \tag{3.9}$$

To implement equation 3.7 in real-time, the two frequency responses, $h_{-}(\omega)$ and $h_{+}(\omega)$, can be approximated using FIR filters [73,78,79], which can be achieved, for example, by using the MATLAB function `invfreqz`. However, if this function is directly used to approximate the frequency responses, the resulting impulse responses are non-causal. To ensure causality, a small delay is added prior to calculating the filters by multiplying the frequency responses by $\mathrm{e}^{\mathrm{i}\omega n_s}$, where n_s is a discrete number of samples [73,78]. The effect that this delay has on the performance of the control system is minimal if the propagation time between the accelerometers and the piezo is greater than n_s [80]. The resulting, causal, FIR filters will be referred to as $\boldsymbol{h}_{-}(t)$ and $\boldsymbol{h}_{+}(t)$ in the following sections.

3.1.2 Controller Formulation

A diagram of the control setup is shown in Fig. 3.2 and a block diagram of the controller that minimises the reflected wave is shown in Figure 3.3. Although there are two accelerometers used as error sensors, the controller is only required to minimise the reflected wave, and so uses a single-input single-output feedforward architecture. The measured signals are passed through the two FIR wave filters of I_h coefficients, $\boldsymbol{h}_{-}$ and $\boldsymbol{h}_{+}$, to give the reflected wave components of the signals, denoted by a subscript ϕ^{-}. In this system, the reference signal, $x(n)$, is the signal that is being used to drive

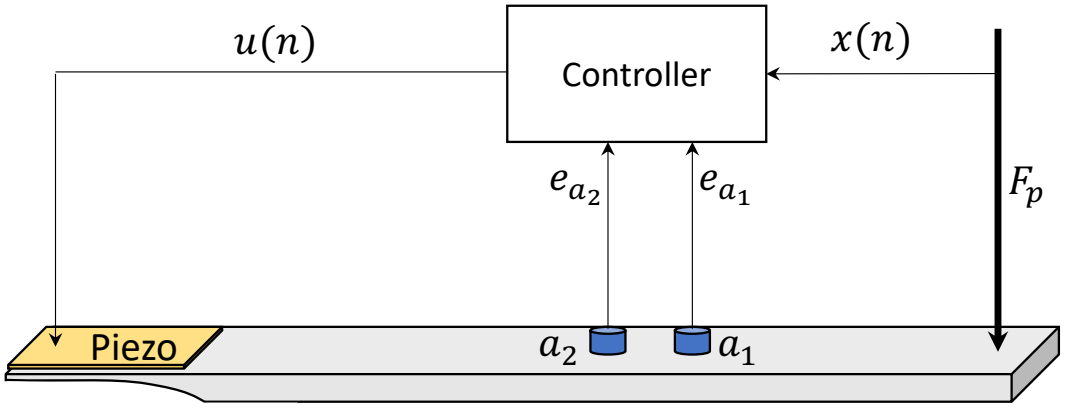

FIGURE 3.2: A diagram showing a beam with an AABH termination and two accelerometers that are used as the error sensors for the wave-based feedforward active control system. The signal from each of these accelerometers is fed into the controller in addition to a reference signal taken from the primary input.

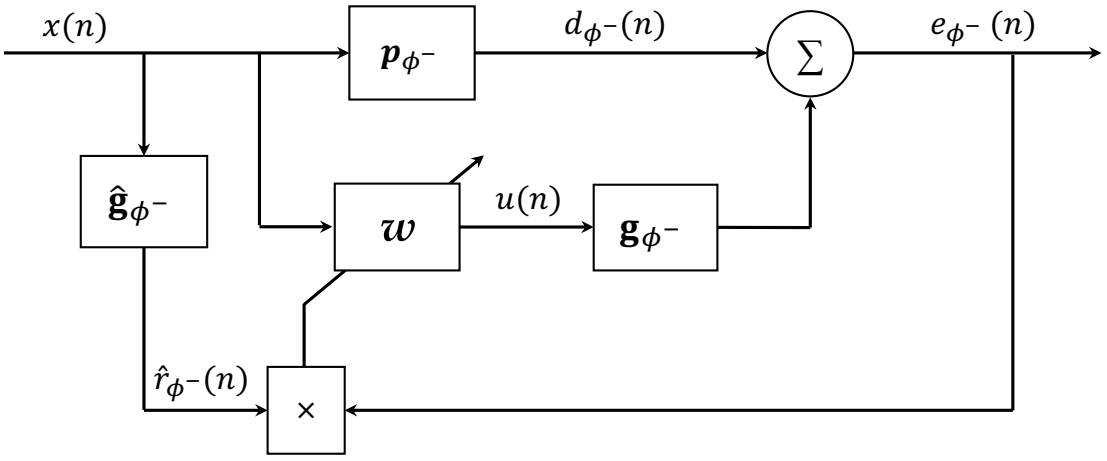

FIGURE 3.3: A block diagram showing a wave-based feedforward active control system. ϕ^- has been used to denote the reflected wave component of the respective filter or signal, that is obtained by using the wave filters described in Section 3.1.1. In this control system the digital controller, $\boldsymbol{w}$, is adapted to minimise the error signal, e_{ϕ^-}.

the primary disturbance. Although the incident wave component could be used as the reference signal, similarly to [78], the use of the disturbance signal has been chosen because it allows the optimal performance to be assessed without being limited by the quality of the reference signal. In practice, however, it is unlikely that the disturbance signal would be available and the incident wave would be used as the reference signal. This may require a higher sample rate to account for delays in the signal processing. The elements in the vector $x(n)$ correspond to the signal measured at the n-th time step. This signal is filtered by $\widehat{\boldsymbol{g}}_{\phi^-}$, which represents the combined response of the estimated plant filter and the reflected wave filter, calculated as

$$\widehat{\boldsymbol{g}}_{\phi^-} = [\boldsymbol{h}_+^T \widehat{\boldsymbol{g}}_{a_1}] + [\boldsymbol{h}_-^T \widehat{\boldsymbol{g}}_{a_2}], \tag{3.10}$$

where the subscript a_1 and a_2 denotes the estimated plant filter corresponding to the respective accelerometer shown in Figure 3.2. The filtered reference signal can thus be expressed as

$$\hat{r}_{\phi^-}(n) = \widehat{\boldsymbol{g}}_{\phi^-}^T x(n), \tag{3.11}$$

where $x(n)$ is the vector of current and past samples of the reference signal. $\hat{r}_{\phi^-}$ is used to update the controller, $\boldsymbol{w}$, which is used to filter the reference signal to generate the control signal, $u(n)$. The reference signal is also filtered by the primary response FIR filter, $\boldsymbol{p}_{\phi^-}$, to obtain the disturbance signal where

$$\boldsymbol{p}_{\phi^-} = [\boldsymbol{h}_+^T \boldsymbol{p}_{a_1}] + [\boldsymbol{h}_-^T \boldsymbol{p}_{a_2}]. \tag{3.12}$$

The error signal can be calculated as the sum of the reflected wave component of the primary disturbance,

$$d_{\phi^-}(n) = \boldsymbol{p}_{\phi^-}^T x(n), \tag{3.13}$$

and the reflected wave component of the secondary disturbance, $\boldsymbol{g}_{\phi^-}^T u(n)$, where

$$\boldsymbol{g}_{\phi^-} = [\boldsymbol{h}_+^T \boldsymbol{g}_{a_1}] + [\boldsymbol{h}_-^T \boldsymbol{g}_{a_2}] \tag{3.14}$$

is the secondary path of the reflected wave component between the piezoelectric patch and the sensor array and $u(n)$ is the vector of current and past samples of the control signal. The error can be expressed as

$$e_{\phi^-}(n) = d_{\phi^-}(n) + \sum_{j=0}^{J-1} \boldsymbol{g}_{\phi_j^-} u(n-j), \tag{3.15}$$

where the secondary path between the control source and the reflected wave component measured at the error sensor has been represented by a J-th order FIR filter with coefficients $\boldsymbol{g}_{\phi_j^-}$. As shown in Figure 3.3, the control signal is generated by filtering the reference signal, $x(n)$, with the controller, $\boldsymbol{w}$, which is implemented as a FIR filter with I coefficients, $\boldsymbol{w}_i$, to give

$$u(n) = \sum_{i=0}^{I-1} w_i x(n-i). \tag{3.16}$$

Substituting Equation 3.16 into 3.15 then gives the error signal at the sensor array as

$$e_{\phi^-}(n) = d_{\phi^-}(n) + \sum_{j=0}^{J-1} \sum_{i=0}^{I-1} \boldsymbol{g}_{\phi_j^-} w_i x(n-i-j), \tag{3.17}$$

and by making the assumption that the control filter is time-invariant [81], this can be rewritten as

$$e_{\phi^-}(n) = d_{\phi^-}(n) + \sum_{i=0}^{I-1} w_i \hat{r}_{\phi^-}(n-i), \tag{3.18}$$

where the reference signal filtered by the reflected wave component secondary path response is

$$\hat{r}_{\phi^-}(n) = \sum_{j=0}^{J-1} \hat{\boldsymbol{g}}_{\phi_j^-} x(n-j). \tag{3.19}$$

Equation 3.18 can be expressed more succinctly using vector notation as

$$e_{\phi^-}(n) = d_{\phi^-}(n) + \boldsymbol{w}^T \hat{\boldsymbol{r}}_{\phi^-}(n), \tag{3.20}$$

With the error signal expressed in Equation 3.20, it is possible to derive the optimal broadband control filter that minimises the cost function defined as the weighted summation of the mean-squared error signal and the sum of the squared control filter coefficients. This cost function can be expressed as

$$\boldsymbol{J}(n) = \mathrm{E}[e_{\phi^-}^2(n)] + \beta \boldsymbol{w}^T \boldsymbol{w}, \tag{3.21}$$

where E denotes the expectation operator and β is a positive control effort coefficient-weighting parameter. The inclusion of the second term in the cost function has a number of practical benefits, which are discussed in Section 2.3.1 of [81], and it has been included here primarily to enable a constraint to be imposed on the magnitude of the control signals. Substituting Equation 3.20 into Equation 3.21 gives

$$\boldsymbol{J}(n) = \boldsymbol{w}^T \mathrm{E}[\hat{\boldsymbol{r}}_{\phi^-}(n)\hat{\boldsymbol{r}}_{\phi^-}^T(n)]\boldsymbol{w} + 2\boldsymbol{w}^T \mathrm{E}[\hat{\boldsymbol{r}}_{\phi^-}(n)d_{\phi^-}(n)] + \mathrm{E}[d_{\phi^-}^2(n)] + \beta \boldsymbol{w}^T \boldsymbol{w}, \tag{3.22}$$

where $\mathrm{E}[\hat{\boldsymbol{r}}_{\phi^-}(n)\hat{\boldsymbol{r}}_{\phi^-}^T(n)]$ is the autocorrelation matrix of the filtered reference signal and $\mathrm{E}[\hat{\boldsymbol{r}}_{\phi^-}(n)d_{\phi^-}(n)]$ is the cross-correlation vector between the filtered reference signal and the disturbance [81]. The vector of optimal control filter coefficients can then be calculated by setting the derivative of Equation 5.15 with respect to the control filter coefficients to zero and this leads to the optimal solution

$$\boldsymbol{w}_{opt} = -\left\{\mathrm{E}[\hat{\boldsymbol{r}}_{\phi^-}(n)\hat{\boldsymbol{r}}_{\phi^-}^T(n)] + \beta \mathbf{I}\right\}^{-1} \mathrm{E}[\hat{\boldsymbol{r}}_{\phi^-}(n)d_{\phi^-}(n)], \tag{3.23}$$

where $\mathbf{I}$ is the identity matrix. From Equation 3.23, it can be seen that β is used to add a value that is proportional to the sum of the squared filter weights. This is equivalent to adding white noise with a mean-square value of β to the reference signal [81]. A finite value of β can prevent large filter coefficient values, which do not significantly reduce the mean-square error and which lead to a control signal with a large peak-to-peak voltage. Additionally, it is assumed that the inverted matrix in Equation 3.23 is positive definite and can, therefore, be inverted and it can be seen that a finite value of β regularises the solution to the inverse problem [81]. In a practical real-time implementation, the optimum solution is usually reached by an adaptive algorithm such as the FxLMS algorithm. However, in the following investigation the optimal solution given by Equation 3.23 will be utilised to ensure that the limitations on the maximum control performance are clearly demonstrated.

3.2 An Experimental Investigation of an Active Acoustic Black Hole Termination

In this section, an experimental investigation into the use of an AABH termination for wave-based feedforward control is presented. The performance of the AABH termination has been compared to a constant thickness termination, both with the same active components. The layout of this section is as follows. The experimental setup is described in Section 3.2.1. Section 3.2.3 presents a plant modelling study, where the relationship between the length of the FIR filter used to model the plant response and the accuracy of the resulting plant model has been investigated. From these results, a specific error has been selected so that the accuracy of the plant model for each termination configuration is the same. A control filter length study is presented in Section 3.2.4,

where the length of the control filter has been compared to the average broadband attenuation achieved. The performance of each termination has then been assessed over frequency in Section 3.2.5, where the same control filter length has been used for each termination. Finally, the results from a real-time validation are presented in Section 3.2.6.

3.2.1 Experimental Setup

The dimensions of each of the two beams used in this investigation are shown in Table 3.1 and a diagram is shown in Figure 3.4 for clarity. These dimensions are identical to the dimensions of the ABH and constant thickness terminations that have been used to experimentally validate the model in Chapter 2, because the ABH design provides effective passive damping and allows a direct comparison to be made between the passive performance of the piezoelectric patch and the viscoelastic damping material used in Chapter 2 (Henley's yellow compound [77]).

TABLE 3.1: The geometrical parameters for the beam and each termination. Each parameter has a tolerance of $\pm$ 0.1 mm.

Parameter	Beam	ABH termination	Constant thickness termination
Height	10 mm	$(9.5(1\text{-}(x/70))^4 + 0.5)$ mm	10 mm
Length	300 mm	70 mm	70 mm
Width	40 mm	40 mm	40 mm

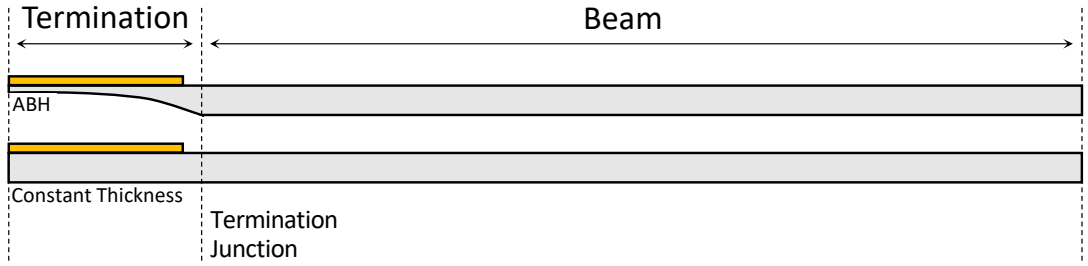

FIGURE 3.4: A diagram showing the beam and termination described in Table 3.1.

A PI Ceramic P-876.A11 DuraAct patch transducer has been attached to the flat side of the ABH taper and to the constant thickness termination using adhesive. The flat side of the ABH taper was chosen so that the piezo patch was not pre-stressed on either termination. The P-876.A11 patch has a mass of 2 g, an operating voltage range of -50 V to 200 V and its dimensions are 61 mm $\times$ 35 mm $\times$ 0.4 mm. Full technical specifications for the piezo patch can be found at [82]. Figure 3.5 shows a diagram of the experimental setup and a photo of each configuration is shown in Figure 3.6.

When set up, the effective mass of the piezoelectric patch was 4 g due to the extra mass of the hanging wires. A comparison between the damping performance of the

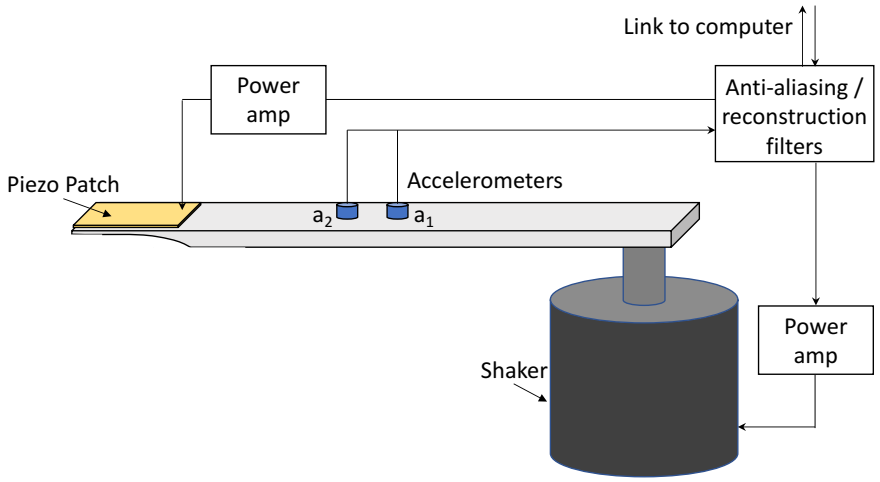

FIGURE 3.5: A diagram showing the experimental setup used in this investigation.

(a) (b)

FIGURE 3.6: Pictures of the experimental setup used to measure the responses of the AABH and beam.

piezoelectric transducer and 12 g of Henley's yellow compound, which was used in the experimental investigation presented in Chapter 2, can be seen in Figure 3.7. These results show that the piezoelectric patch provides a slightly lower level of damping compared to the Henley's yellow compound and this is demonstrated by the minima in the bands of low reflection, which are lower when Henley's yellow compound is used. This is also evident from the broadband average reflection coefficient, which is 0.62 when the piezoelectric patch is used and 0.54 when Henley's yellow compound is used. The difference in frequency of the minima in the bands of low reflection can be attributed to the higher mass of the Henley's (12 g) compared to the effective mass of the piezoelectric patch (4 g) and the additional stiffness that is associated with each damping treatment.

Two accelerometers were attached to the beam using wax and were placed 200 mm and 220 mm from the primary source. Referring to Section 2.2, the low frequency limit of the wave decomposition can be calculated as approximately 310 Hz, which has been

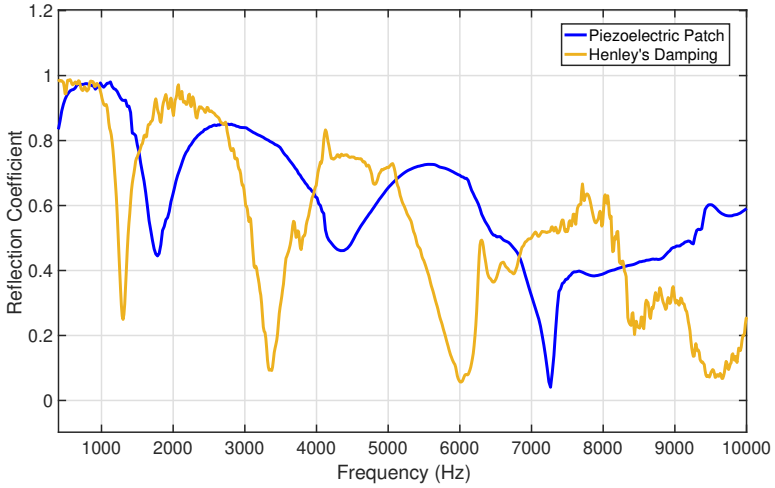

FIGURE 3.7: The reflection coefficient of the ABH termination when the piezoelectric patch is attached (dark blue line) compared with the Henley's yellow compound (yellow line).

rounded up to 400 Hz for this investigation. The upper frequency limit is determined by the largest distance, selected from the accelerometer spacing, 20 mm, the width of the beam, 40 mm, and the height of the beam, 10 mm. In this case, the width of the beam is the longest and the upper frequency limit can be calculated as approximately 14 kHz. However, the anti-aliasing and re-construction filters used were set to a cut-off frequency of 10 kHz, which thus defines the upper frequency limit. In addition to the aliasing high frequency limit, there is another high frequency limit that occurs when the delay through the controller is greater than the group delay between the actuators and sensors [1]. In this investigation, a sampling frequency of 24 kHz has been used, which equates to a sampling period of approximately 42 μs. The frequency at which the group delay between the piezoelectric patch and the closest sensor on the beam becomes equal to or less than the delay through the controller has been calculated as approximately 15 kHz. This is higher than the 10 kHz upper frequency limit imposed by the anti-aliasing and reconstruction filters and therefore this frequency limit does not limit the controller.

3.2.2 Plant Responses

As discussed in Section 3.1.2, the proposed wave-based feedforward control strategy requires an accurate model of the plant response to generate the filtered reference signal, $\hat{r}_{\phi^-}$. The plant model for each configuration has been calculated by fitting a FIR filter to the respective plant response using the MATLAB function `invfreqz`. To examine the requirements of the AABH and constant thickness active termination plant models, a study that compares the plant modelling error to the number of FIR coefficients in the plant model has been carried out.

Using a sampling frequency of 24 kHz, the plant responses between the piezoelectric transducer and each of the two accelerometers have been calculated by driving the transducer with broadband white noise and taking a 60 second measurement. The disturbance signal was kept the same for each configuration. The frequency responses were calculated using the H1-estimator and are presented in Figure 4.1.

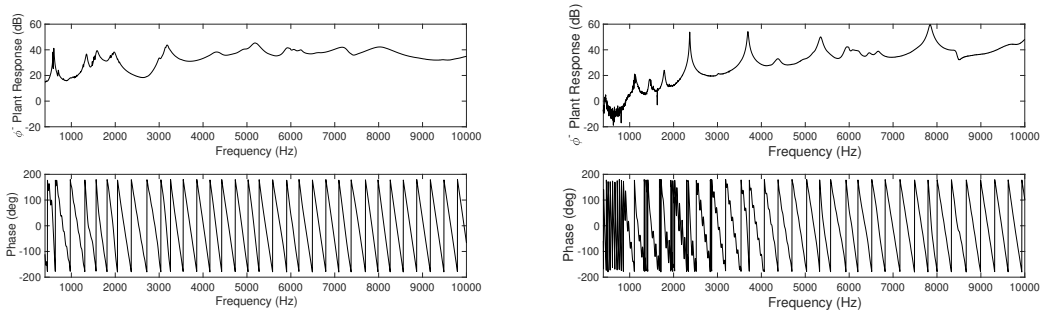

FIGURE 3.8: The frequency response and phase of the reflected wave for a beam with (a) an AABH termination and (b) a constant thickness active termination.

Figure 3.8(a) shows the frequency response of the reflected wave for the AABH termination. The results show that there is a resonance with a double peak at 0.6 kHz, which can be seen to align with with a rapid phase change, and three more peaks at 1.35 kHz, 1.6 kHz and 1.95 kHz. The final notable peak occurs at approximately 3.2 kHz. All higher resonances have been significantly damped by the passive behaviour of the AABH. Figure 3.8(b) shows the frequency response of the reflected wave for the constant thickness active termination. The results show that there are strong resonances at 2.4 kHz, 3.65 kHz and 7.75 kHz. There are also resonances with smaller magnitudes at 0.5 kHz, 1.15 kHz, 1.75 kHz and 5.4 kHz. The low frequency resonances are smaller in magnitude because the constant thickness active termination requires a larger force to excite low order modes. Unlike the AABH termination, where there was a significantly rapid phase change at the 600 Hz resonance, it can be seen from the results in Figure 3.8(b) that there are are a lot of rapid phase changes occurring below 4 kHz in the response of the constant thickness active termination. It can also be seen that below 3 kHz the frequency response of the AABH termination is much higher than the frequency response of the constant thickness termination, indicating that the thin taper has better coupling with the piezoelectric patch at lower frequencies.

3.2.3 The Effect of Plant Modelling Accuracy

To investigate the plant modelling requirements, the frequency responses presented in Figure 4.1 have been subsequently modelled using FIR filters. To create the FIR filters, the MATLAB function `invfreqz` has been used. The FIR filters have been weighted so

that they are most accurate between 400 Hz and 10 kHz. In order to examine the effect of plant model accuracy, the number of FIR filter coefficients has been varied from 10 to 5000 (or 0.4 to 208 ms at the 24 kHz sample rate). As a measure of the plant model error, the normalised mean-squared error (NMSE) has been calculated as

$$\text{NMSE} = \frac{1}{2}\sum_{l=1}^{2}\frac{\left[(\boldsymbol{g}_l - \widehat{\boldsymbol{g}}_l)^H(\boldsymbol{g}_l - \widehat{\boldsymbol{g}}_l)\right]}{(\boldsymbol{g}_l^H \boldsymbol{g}_l)}, \tag{3.24}$$

for each filter length and averaged over both accelerometers. In Equation 3.24, $\widehat{\boldsymbol{g}}_l$ is the column vector containing the frequency response of the plant model FIR filter and $\boldsymbol{g}_l$ is the identified plant, both between the piezoelectric patch and the l-th accelerometer. These results are shown in Figure 3.9 for the beam with an AABH termination and the beam with a constant thickness termination.

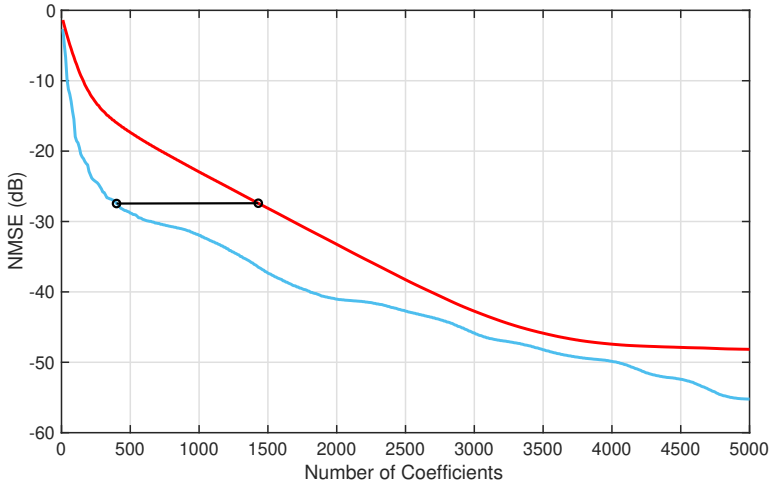

FIGURE 3.9: The NMSE of the plant model for filter lengths between 10 and 5000 coefficients. The red line represents the constant thickness termination and the blue line represents the AABH. A plant modelling error has been selected so that it is the same for both the constant thickness termination and the AABH termination. This has been marked on the figure in black.

From the results shown in Figure 3.9, which have been calculated using Equation 5.18, it can be seen that increasing the number of filter coefficients in the plant model decreases the NMSE. It can also be seen that the AABH configuration requires fewer filter coefficients than the constant thickness active termination configuration to achieve the same NMSE in the plant model. The difference can be attributed to the extra passive damping provided by the ABH. This is a potentially significant advantage because it reduces the computational requirements of implementing the active feedforward control strategy outlined in Section 3.1.2. A comparative case has been highlighted by the black line in Figure 3.9. For this case, the NMSE of the plant model has been kept at -28 dB for both the AABH termination and the constant thickness termination. To achieve this level of error, 400 FIR filter coefficients were required to model the plant response of the AABH and 1430 FIR filter coefficients were required to model the plant response

of the constant thickness active termination. From this case study, it can be seen that the AABH termination potentially allows a more computationally efficient implementation of the FxLMS controller.

3.2.4 The Effect of Controller Length

Having established the case study for accurate plant modelling, this section is used to investigate the effect of the control filter length. To assess how many coefficients are required for the optimum controller, $\boldsymbol{w}_{opt}$, the total broadband attenuation of the reflection coefficient has been calculated for a range of control filter lengths. At each frequency, the reflection coefficient has been calculated as

$$R(\omega) = \left| \frac{\phi^-(\omega)}{\phi^+(\omega)} \right|, \tag{3.25}$$

where the wave components, ϕ^+ and ϕ^-, have been decomposed previously for the controller in Section 3.1.1. The attenuation at each frequency has been calculated as

$$R_{atten}(\omega) = -20 \log_{10} \left(\frac{R(\omega)}{R_0(\omega)} \right), \tag{3.26}$$

where R_0 is the passive reflection coefficient of the beam with a constant thickness termination, which has been used as a reference reflection coefficient, and R is the reflection coefficient of the test case. Finally, the total broadband average attenuation of the reflection coefficient can be calculated by taking the frequency average of R_{atten}, in this case over a bandwidth of 400 Hz – 10 kHz.

The optimum set of control filter coefficients have been calculated using the measured plant responses for each of the beam configurations and the control effort weighting coefficient, β in Section 3.1.2, was initially set to zero for each case. For the constant thickness termination configuration, β has also been set so that the peak-to-peak input voltage is equal to the peak-to-peak input voltage required by the optimal AABH configuration. This limitation allows the two control systems to be directly compared.

The broadband attenuation has been calculated for the un-regularised AABH termination, un-regularised constant thickness termination and regularised constant thickness termination using a range of 0 to 500 controller coefficients. The broadband average attenuation, normalised with respect to the passive, uncontrolled, beam with a constant thickness termination, can be seen in Figure 3.10(a) and the maximum peak-to-peak voltage of the control signal can be seen in Figure 3.10(b). The passive performance can be seen when the control filter length is 0. From the results presented in Figure 3.10(a), it can be seen that in all cases the broadband performance increases as the number of control filter coefficients increases. The increase in performance is initially quite rapid, however for a control filter length of over 350 coefficients there is less than 1 dB increase

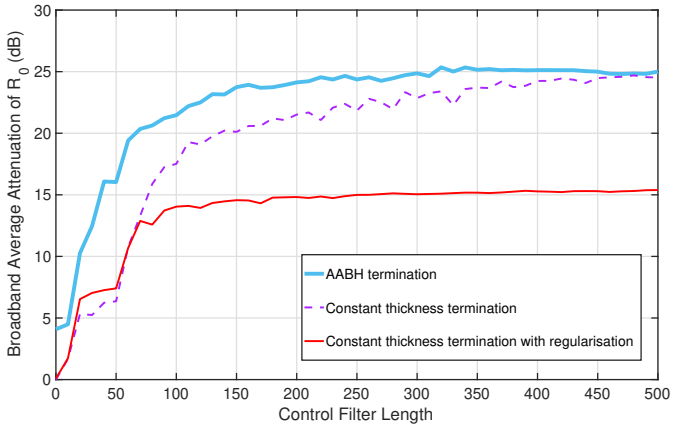

(a)

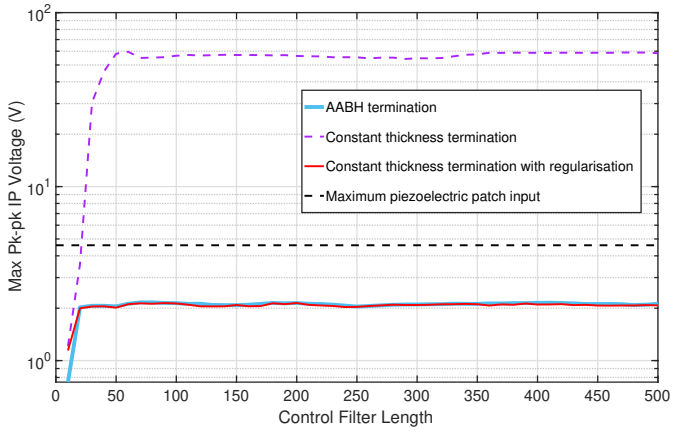

(b)

FIGURE 3.10: (a) The total broadband attenuation with respect to the passive constant thickness termination vs the control filter length and (b) the maximum peak-to-peak voltage of the control signal for each of the case studies.

in performance for any of the controllers. In addition to demonstrating how the performance varies with control filter length, it can be seen in Figure 3.10(a) that the AABH termination provides more attenuation than the constant thickness termination with or without regularisation, up to the limit of 500 control filter coefficients shown here. This is due to the increased passive performance of the AABH that can be seen by examining the broadband performance at 0 control filter coefficients (where the AABH termination achieves approximately 4 dB of attenuation passively). Although when 500 controller coefficients are used the performance of the AABH termination and un-regularised constant thickness termination are similar, it can be seen from Figure 3.10(b) that the maximum peak-to-peak voltage of the control signal for the un-regularised constant thickness termination is approximately 13 times the peak-to-peak voltage required by the AABH system. It is important to highlight that the maximum operating peak-to-peak voltage for the piezoelectric transducer used in this investigation has been marked as the dashed black line in Figure 3.10(b), and it is clear that without regularisation the

constant thickness termination significantly exceeds this physical limit. Some insight into the reason for this can be seen in the plant models shown in Section 3.2.2, where the magnitude of the plant response for the AABH termination is generally larger than the magnitude of the plant response for the constant thickness termination, especially at lower frequencies. Therefore, Figures 3.10(a) and 3.10(b) also show the performance of the constant thickness termination when the maximum peak-to-peak voltage of the control signal has been regularised to the same level as the AABH termination, which is within the physical limit of the patch. In this case, it can be seen that the performance of the constant thickness termination is reduced and the performance of the AABH termination is increased by approximately 10 dB for longer control filter lengths. It can be noted that this performance is not just due to the passive effect of the AABH, as this only accounts for 4 dB of broadband attenuation. These results thus demonstrate that the AABH termination has practical advantages over a standard constant thickness active termination.

3.2.5 Broadband Performance

To provide a detailed comparison between the active beam terminations in this study, the reflection coefficient has been calculated for each termination over a frequency range of 400 Hz to 10 kHz, with and without control. The control parameters for the AABH termination are 400 plant model coefficients and 350 controller coefficients; the control parameters for the constant thickness termination are 1430 plant model coefficients and 350 control filter coefficients. Two cases are presented for the constant thickness termination, one where the controller is unconstrained and the other where the maximum peak-to-peak voltage of the control signal has been regularised to the same level as the AABH. These results, therefore, show the control performance of each termination when operating under the same limitations. In addition to the control performance, the required control effort for each controller configuration, defined as $\boldsymbol{w}^T\boldsymbol{w}$, has been presented.

Figure 3.11 shows the reflection coefficient and control effort for the different terminations over frequency. From the results shown in Figure 3.11(a), it can be seen that the reflection coefficient of the constant thickness termination without control is approximately 1 over the frequency bandwidth shown and the reflection coefficient of the beam with an AABH termination without control exhibits the bands of low reflection that are typical of a passive ABH. The passive damping required for the ABH effect is, in this case, being provided by the piezoelectric patch. It can be seen, from the active control results in Figure 3.11(a), that all configurations achieve control over the full frequency bandwidth presented. When control is performed using the AABH termination (light blue line), the reflection coefficient is almost perfectly controlled at all frequencies above 4.1 kHz. Between 400 Hz and 4.4 kHz, the reflection coefficient is also reduced

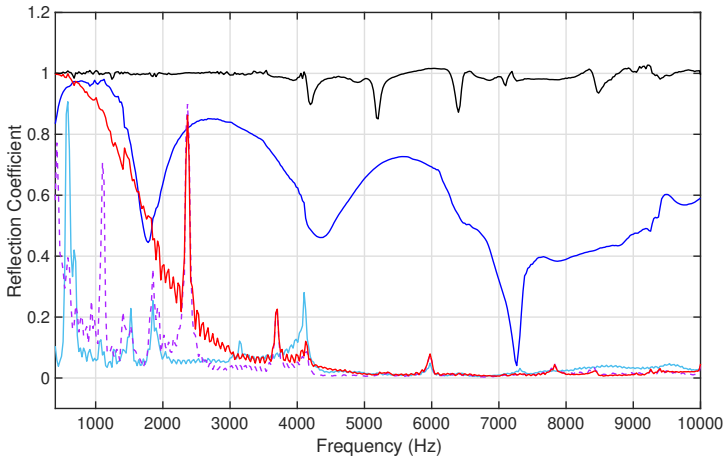

(a)

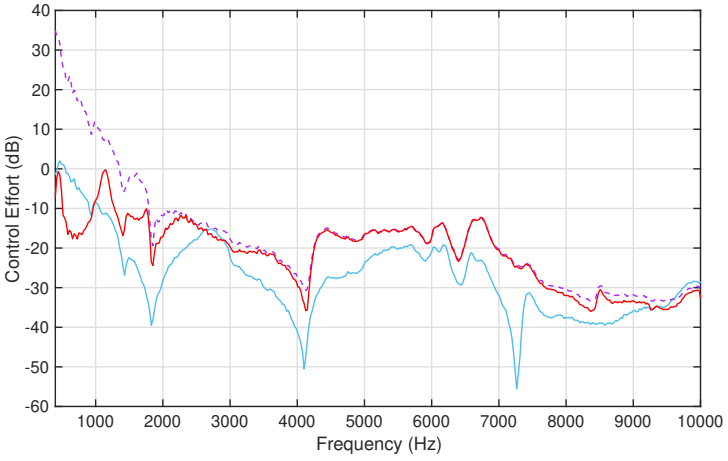

(b)

FIGURE 3.11: (a) The reflection coefficient of the AABH termination without control (dark blue line), AABH termination with control (light blue line), constant thickness termination without control (black line), constant thickness termination with unconstrained control (purple dashed line), and constant thickness termination with constrained control (red line). (b) The control effort required in each respective control case. The control effort has been normalised so that a constant level at 0 dB corresponds to the maximum broadband input to the piezoelectric patch.

to almost zero, but there is one notable peak where control is less effective. This occurs at approximately 600 Hz and is attributed to a dominant structural resonance that can be seen in the plant response, shown in Section 3.2.2. This resonance coincides with a rapid phase change, which is difficult to model accurately.

When control is performed using the un-regularised constant thickness termination (purple dashed line), the reflection coefficient is almost perfectly controlled above 4.1 kHz. Between 400 Hz and 4.1 kHz, the reflection coefficient is mostly controlled, except for peaks at approximately 420 Hz, 1.1 kHz and 2.4 kHz. Similarly to the AABH termination, these frequencies correspond with dominant structural resonances that can be

seen in the plant response, shown in Section 3.2.2. These peaks in the response largely account for the difference in the broadband average level between the un-regularised constant thickness termination and the AABH termination, shown in Figure 3.10(a). When control is performed using the regularised constant thickness termination (red line), the reflection coefficient is still almost perfectly controlled above 4.1 kHz, however below this frequency it can be seen that the regularisation largely limits the performance of the active termination to a level that, below 2 kHz, it is comparable with the uncontrolled AABH termination.

The control effort for each of the three performance results is shown in Figure 3.11(b). These results have been presented with reference to the control effort corresponding to the maximum broadband input to the piezoelectric actuator. From these results, it can be seen that the beam with an AABH termination requires up to 30 dB less energy than the constant thickness termination. Although this difference is largest below 2 kHz, it can be seen that the control effort requirements are still notably less for the AABH at higher frequencies. Although the employed level of regularisation for the constant thickness termination limits the large control effort below 2 kHz, the effort required at higher frequencies is still more compared to the AABH termination. This is reflected in the average level of the control effort, which is -31 dB for the AABH termination, -24 dB for the un-regularised constant thickness active termination and -25 dB for the regularised constant thickness active termination. These results more clearly demonstrate the advantages of the AABH termination over the constant thickness active termination that have already been noted in the broadband average performance results presented in Section 3.2.4. Once again, it is interesting to note that the performance advantage of the AABH is above that expected by simply combining the passive performance gained by the ABH with the active performance of the constant thickness termination. Particularly, at frequencies outside of the bands of low reflection, the AABH is able to achieve near perfect absorption with a lower control effort compared to the constant thickness active termination.

It has been shown by the presented results that the AABH termination outperforms the constant thickness termination in terms of the broadband reflection coefficient. In addition, it has been shown that the AABH termination is more efficient because it requires a significantly reduced control effort to achieve the same or better performance. In order to further understand the effect that control has on the response of the termination, Figure 3.12 presents the responses of each termination, with and without control. From the results presented in Figures 3.12(a) and 3.12(b), it can be seen that the AABH termination response is, on average, 10 dB greater than the constant thickness termination response. This is to be expected because the ABH effect is known to focus energy into the taper, as observed in [41, 47, 83]. It is interesting, however, to observe the effect that control has on each termination response. In the case of the AABH termination (Figure 3.12(a)), it can be seen that controlling the reflected wave significantly enhances

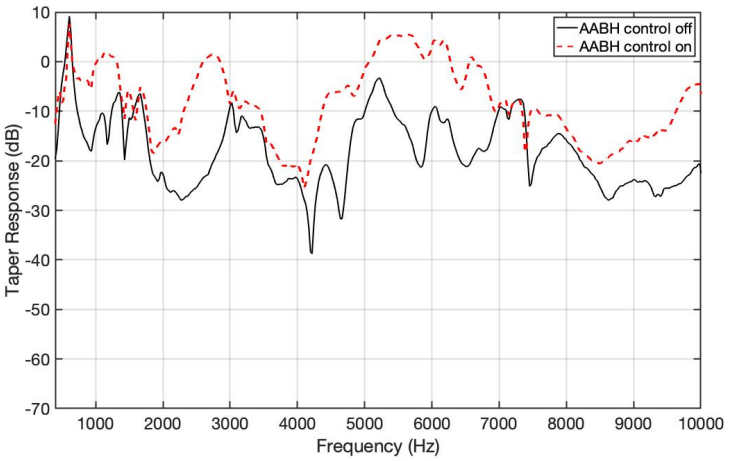

(a)

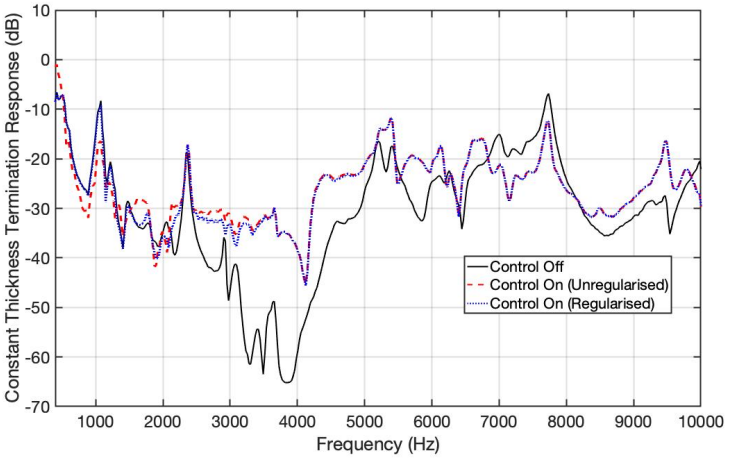

(b)

FIGURE 3.12: The response measured at (a) the AABH termination with and without control, and (b) the constant thickness termination with and without control and with regularised control.

the taper response across the majority of the presented bandwidth. On the other hand, when the reflected wave is controlled using the constant thickness termination, there is only a modest variation in the response over the presented bandwidth. The main enhancement in this case is between 3 kHz and 5 kHz where the uncontrolled response is low. These results indicate that for this control strategy, there is a trade-off between enhancing the stress concentration in the taper and reducing the reflection coefficient of the termination, which has been considered for passive ABHs in [84]. In the case of an active termination, this trade-off will be addressed in more detail in Chapter 4.

3.2.6 Real-Time Experimental Validation

The practical control configurations where the plant model error has been kept the same for the two terminations have been implemented experimentally. In this case, 400 FIR filter coefficients were used in the plant model for the beam with the AABH termination and 1430 FIR coefficients were used in the plant model for the beam with a constant thickness termination. 350 control filter coefficients were used and the wave filters were delayed by 10 samples to ensure causality. The optimal control filter has been calculated using Equation 3.23 and implemented directly. Due to the physical limitations of the piezoelectric patch, it was not possible to experimentally evaluate the unconstrained constant thickness active termination configuration and, therefore, the results are only presented for the constrained case where the peak-to-peak voltage is consistent for both the AABH and the constant thickness termination. The control performance and control effort results for this real-time implementation are presented in Figure 3.13.

In general, the real-time results shown in Figure 3.13 are consistent with the offline simulations presented in Section 3.2.5. Both the offline and real-time results show that when the performance of both control systems is compared, the beam with an AABH termination outperforms the beam with an active constant thickness termination at almost all frequencies, with the most significant performance benefit being shown below 3 kHz. The AABH termination is also shown to be more efficient, requiring a reduced control effort to give superior performance. A general observation from comparing the offline and real-time results is that the peaks in the controlled responses are more significant in the real-time results. For example, there are two peaks in the reflection coefficient of the active constant thickness termination at 2.4 kHz and 3.7 kHz where there is enhancement. These peaks in the reflection coefficient are related to the rapid phase changes that occur due to the lightly damped resonances in the structure and lead to narrowband errors between the modelled and physical plant. Despite these narrowband differences between the predictions and measurement results, the broadband, reflection coefficient differs by only 0.1 in the case of the constant thickness beam results and 0.06 in the case of the AABH, therefore demonstrating that the offline predictions provide a reliable estimation of the real-time performance. The effects of this are exacerbated in the real-time results due to finite precision effects. Despite this, it is clear that the AABH termination offers significant performance benefits over the constant thickness active termination and the nature of the practical implementation will determine whether the AABH is suitable.

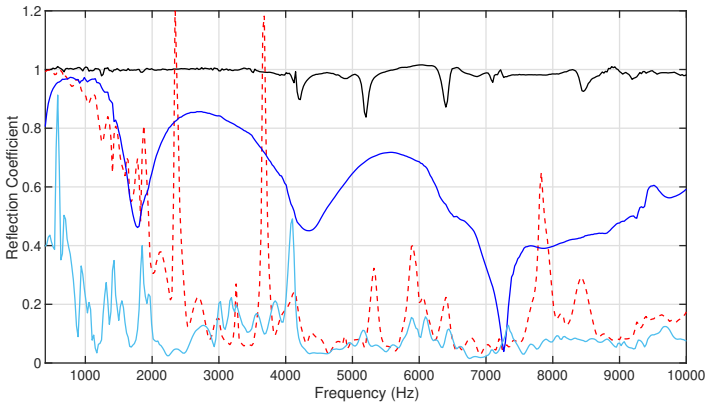

(a)

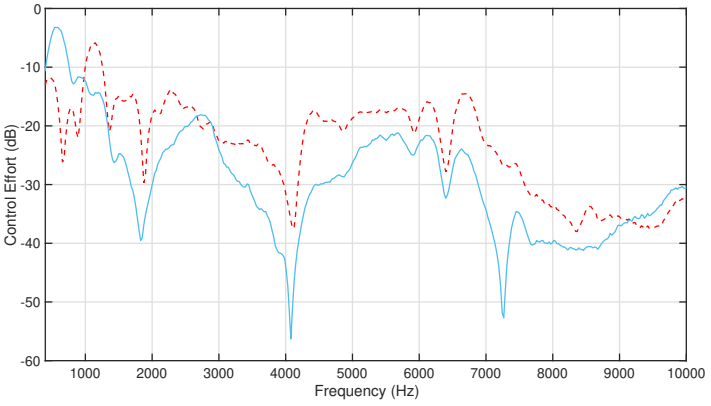

(b)

FIGURE 3.13: (a) The reflection coefficient of the uncontrolled constant thickness active termination (black line), controlled constant thickness active termination (dashed red line), uncontrolled AABH termination (dark blue line) and controlled AABH termination (light blue line). (b) The control effort required for each control case is shown in the respective colour. The control effort has been plotted with respect to the maximum broadband peak-to-peak input to the piezo.

3.3 Summary

This chapter has presented a detailed investigation into a hybrid control solution, consisting of an ABH with a piezoelectric transducer attached to the taper. A feedforward control strategy has been implemented where the piezoelectric transducer has been driven to minimise the flexural wave reflected from the termination. The characteristic behaviour of the AABH termination has been compared to a constant thickness active termination. Initially, a plant modelling study has been carried out in order to assess how the number of FIR filter coefficients affects the accuracy of the plant model. It has been shown that the AABH termination requires fewer FIR filter coefficients to achieve the same plant modelling error. This study has, therefore, shown that the AABH can be

implemented with a lower computational requirement compared to the constant thickness active termination, whilst achieving the same level of NMSE in the plant model.

A study of the control filter length for each case study has then been presented, which shows how the broadband average attenuation varies with the control filter length. It has been shown that, for a specific level of attenuation, the AABH termination requires significantly fewer control filter coefficients than the constant thickness termination. It has also been shown that the total attenuation achieved by using the AABH termination is not matched by the constant thickness termination until 500 control filter coefficients are used. However, despite matching the total broadband attenuation, the peak-to-peak voltage required by the constant thickness termination to achieve this performance is significantly higher than the peak-to-peak voltage required by the AABH termination, far exceeding the maximum input of the piezoelectric transducer. Therefore, the controller has been regularised for the constant thickness active termination so it requires the same maximum peak-to-peak voltage as the AABH termination. This constraint decreases the performance of the constant thickness termination so that the total broadband attenuation is approximately 10 dB lower than the AABH termination for all control filter lengths. The performance advantage of the AABH is, therefore, significantly greater than the level of control provided by the passive ABH effect alone, which was shown to be 4 dB for the investigated configuration. Consequently, the AABH offers a performance advantage above that expected from simply combining the levels of control offered by the constant thickness active termination and the passive ABH effect.

A set of control performance results have then been presented from an offline study. Over frequency, it has been shown that the reflection coefficient can be controlled at all frequencies using either the AABH termination or the constant thickness active termination. For both terminations, there were some poorly controlled frequencies that corresponded to resonances in the plant responses, however this only occurs at one frequency for the AABH termination compared to three frequencies for the constant thickness active termination. It has been shown that the performance of the AABH termination is significantly better than the regularised constant thickness active termination above 4.1 kHz. At lower frequencies, the performance of the regularised constant thickness active termination was notably worse to the extent that, below 2 kHz, the performance was similar to the uncontrolled AABH termination, thus demonstrating a clear performance advantage of the AABH termination at lower frequencies. It has also been shown that the constant thickness termination could, theoretically, perform almost as well as the AABH at lower frequencies, however the control effort required to do so would exceed the power limitations of the piezoelectric transducer. The control effort required for the constant thickness active termination to perform optimally was higher at almost all frequencies when compared to the AABH termination, regardless of constraints. This is reflected in the average level of control effort, which is at least 6

dB less for the AABH termination. Therefore, even if a more powerful transducer was used, the AABH would require significantly less energy to achieve a superior level of control. These results have then been validated experimentally in real-time where, due to the power limitations of the piezoelectric transducer, the constant thickness active termination could only be implemented for the regularised case.

In order to further understand how this feedforward wave-based control strategy affects the termination, the response of each controlled termination has been investigated and it has been shown that the AABH undergoes a significant vibration enhancement in the taper compared to the constant thickness termination. This has been linked to the energy focussing effect observed in passive ABHs and it has been highlighted that the resulting structural fatigue issues should be considered when implementing an AABH in practice.

This chapter has clearly shown the performance advantages of using an AABH termination over a constant thickness termination. In applications where feedforward active control is already used, implementing an AABH could provide significant performance enhancements and reduce power requirements. However, the enhanced vibration in the termination, produced by actively improving the performance of the termination, may cause problems. The following chapter of this thesis will address the tradeoff between actively improving the performance of an AABH termination and reducing vibration in the termination.

Chapter 4

Feedback Control using an Acoustic Black Hole Termination

In Chapter 3, it has been shown that a feedforward control strategy can be used to realise an AABH termination. It has also been shown that the AABH termination provides better performance than a constant thickness active termination and requires less computational and electrical power to implement. However, this increase in performance has also been shown to significantly increase the level of vibration in the AABH termination itself. In addition, the use of a feedforward control strategy requires time-advanced information in the form of a reference signal and this is not always available in real-time applications. This might occur, for example, in the control system presented in Chapter 3, if the propagation time of a wave from the wave decomposition error sensors to the taper is smaller than the signal processing time, which would result in a loss of causality. Another limitation may be that the primary source or sources cannot be measured and, in such cases, a feedback control architecture may provide a solution [1, 81].

In the case of an AABH, the most straightforward feedback control case would be to implement disturbance rejection using a local loop about the taper to control the vibration in the ABH. This would be beneficial because the reduction in vibration would reduce structural fatigue and prolong the life of the ABH. However, if the goal of control is to actively reduce the reflection coefficient of the termination, thus improving the performance of the termination, it has been shown in Chapter 3 that the vibration in the taper is enhanced. An ideal control strategy would be to simultaneously minimise the reflected wave, to increase performance, and the local taper vibration, to reduce structural fatigue.

A geometric controller design approach has been presented in [85], which can be applied to tackle this AABH control problem. In [85], it is shown how a feedback compensator can be calculated that can be used to control both a local and remote error

signal simultaneously, or reach a trade-off between controlling the two variables. This controller design method is further discussed in [86,87] in the context of a robust broadband controller. However, for the broadband case the controller design becomes complex and for the purpose of this study, physical insight can be gained into the control performance and potential trade-offs between local and remote control by considering a tonal controller. To implement the tonal controller, a recursive least squared (RLS) based instantaneous harmonic control (IHC) architecture can be used [85,88].

In this chapter, the geometric controller design process presented in [85] has been applied to the AABH to provide further insight into the tradeoff between controlling the reflected wave and enhancing the local taper vibration in an AABH. The chapter is organised as follows. Section 4.1 presents the controller formulation that can be used to calculate an appropriate compensator and the limitations of the tonal remote damping controller. Section 4.2 contains a description of the experimental setup used and the geometric controller design process has been used to select four control strategies. These four control strategies are control of the local taper vibration, control of the reflected wave component, control of the local taper vibration without enhancing the reflected wave component and control of the reflected wave component without enhancing the local taper vibration. This is followed by the control performance results from a frequency domain implementation of each control strategy. Finally, a time domain implementation of each control strategy is presented in Section 4.2.4 and a summary of the chapter is given in Section 5.4.

4.1 Tonal Remote Damping

In this section, a remote damping controller that can simultaneously consider the local taper vibration and the reflected wave component has been designed using the geometric approach described in [85]. The limitations of this control strategy are also discussed.

The control system examined in this investigation is shown in Figure 4.1 and has two error signals. The first error signal, e_l, is the local vibration that is measured on the ABH taper using an accelerometer and the second error signal, e_{ϕ^-}, which is denoted as the remote variable, and is the reflected wave component that is estimated using two accelerometers located on the beam. In this investigation, the reflected wave component has been estimated using the same method described in Section 3.1.1.

By examining Figure 4.1 it can be seen that there are two primary paths and two secondary paths that have a corresponding frequency response. The frequency response function between the signal driving the control source, u, and the local error, e_l, will be referred to as g_{11}; the frequency response function between the control signal driving the control source, u, and the remote error, e_{ϕ^-}, will be referred to as g_{21}; the frequency

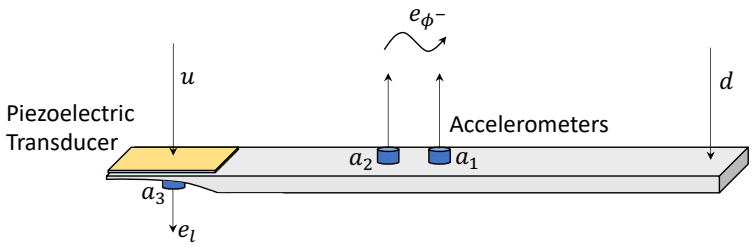

FIGURE 4.1: A diagram of an active ABH termination on one end of a beam. The primary disturbance is driven using the signal d, the control source is driven using the control signal u, the local error signal e_l is measured using accelerometer a_3 and the remote error signal e_{ϕ^-} is estimated using accelerometers a_1 and a_2.

response function between the signal driving the primary disturbance, d, and the local error, e_l, will be referred to as g_{12}; and the frequency response function between the signal driving the primary disturbance, d, and the remote error, e_{ϕ^-}, will be referred to as g_{22}. A block diagram that shows these responses as part of the control system is shown in Figure 4.2. It can be seen that the control signal, u, is produced by applying a compensator, κ, to the local error signal. The control signal is used to drive the piezoelectric patch, which contributes to each error signal via the respective control path. In

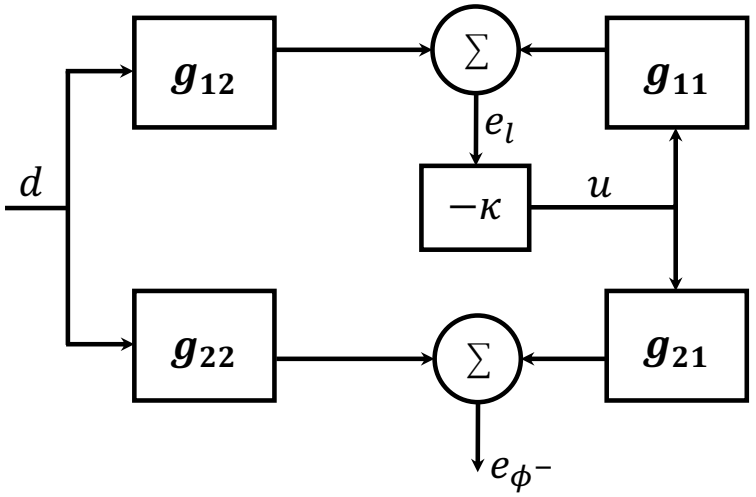

FIGURE 4.2: A block diagram showing the feedback control system. The local signal from accelerometer 3 is fed back through a compensator, κ, to obtain the control signal, u. The control signal is used to drive the piezoelectric transducer and the control of both the taper vibration and the reflected wave component can be examined.

the frequency domain, the frequency response function of the system shown in Figure 4.2 can be written in matrix form as

$$\begin{bmatrix} e_l(\omega) \\ e_{\phi^-}(\omega) \end{bmatrix} = \begin{bmatrix} g_{11}(\omega) & g_{12}(\omega) \\ g_{21}(\omega) & g_{22}(\omega) \end{bmatrix} \begin{bmatrix} u(\omega) \\ d(\omega) \end{bmatrix}. \tag{4.1}$$

Applying the feedback control law for disturbance rejection [81], the control signal can be written as

$$u(\omega) = -\kappa(\omega)e_l(\omega), \tag{4.2}$$

where $-\kappa$ is the negative feedback compensator, which can be set to reduce each error signal. By substituting Equation 4.2 into Equation 4.1 and re-arranging, the local and remote closed loop transfer functions can be written as

$$\frac{e_l(\omega)}{d(\omega)} = \frac{g_{12}(\omega)}{1 + g_{11}(\omega)\kappa(\omega)} \tag{4.3}$$

$$\frac{e_{\phi^-}(\omega)}{d(\omega)} = g_{22}(\omega) - \frac{\kappa(\omega)g_{12}(\omega)g_{21}(\omega)}{(1 + g_{11}(\omega)\kappa(\omega))}. \tag{4.4}$$

The frequency dependency is suppressed from this point forward for clarity, but it should be assumed unless stated otherwise.

In order to determine the conditions required to control either the local or remote error, the closed loop transfer functions can be rewritten as

$$\frac{e_l}{d} = f_l(\kappa)g_{12} \tag{4.5}$$

$$\frac{e_{\phi^-}}{d} = f_{\phi^-}(\kappa)g_{22}, \tag{4.6}$$

where

$$f_l(\kappa) = \frac{1}{1 + g_{11}\kappa} \tag{4.7}$$

$$f_{\phi^-}(\kappa) = 1 - \frac{\kappa g_{12}g_{21}}{g_{22}(1 + g_{11}\kappa)}. \tag{4.8}$$

It can be seen that if $\kappa = 0$, $f_l(\kappa)$ and $f_{\phi^-}(\kappa)$ become equal to 1 and Equations 4.5 and 4.6 become the open loop transfer functions for the local and remote error respectively. To reduce each error signal, the magnitude of the closed loop transfer function has to be less than the magnitude of the open loop transfer function, requiring that

$$|f_l(\kappa)g_{12}| < |f_l(0)g_{12}| \tag{4.9}$$

$$\left|f_{\phi^-}(\kappa)g_{22}\right| < \left|f_{\phi^-}(0)g_{22}\right|, \tag{4.10}$$

or equivalently

$$\left|\frac{1}{1 + g_{11}\kappa}\right| < 1 \tag{4.11}$$

$$\left|1 - \frac{\kappa g_{12}g_{21}}{g_{22}(1 + g_{11}\kappa)}\right| < 1. \tag{4.12}$$

By defining the sensitivity as α, such that Equation 4.11 becomes $|\alpha| < 1$ [85], the sensitivity can be expressed in terms of a compensator as

$$\kappa = \frac{(1-\alpha)}{\alpha g_{11}}. \tag{4.13}$$

Substituting Equation 4.13 into Equation 4.12 gives

$$\left|(\alpha-1)\,\frac{g_{12}g_{21}}{g_{11}g_{22}}+1\right| \;<\; 1, \tag{4.14}$$

which can be simplified to

$$|\beta+1| \;<\; 1, \tag{4.15}$$

where

$$\beta = (\alpha-1)\,\frac{g_{12}g_{21}}{g_{11}g_{22}}. \tag{4.16}$$

α can then be expressed in terms of β[1] by rearranging Equation 4.16, to give

$$\alpha = \beta\frac{g_{11}g_{22}}{g_{12}g_{21}}+1, \tag{4.17}$$

which means Equation 4.11 can be expressed in terms of β as

$$\left|\beta\frac{g_{11}g_{22}}{g_{12}g_{21}}+1\right| \;<\; 1. \tag{4.18}$$

Equation 4.18 can be simplified to

$$|\gamma+1| \;<\; 1, \tag{4.19}$$

where

$$\gamma = \beta\frac{g_{11}g_{22}}{g_{12}g_{21}}. \tag{4.20}$$

Both Equation 4.15 and Equation 4.19 describe a unit circle with a centre point (-1, 0) on the complex β-plane and complex γ-plane respectively. Equation 4.20 shows that Equation 4.16 can be mapped onto the γ-plane as a circle with a centre point at $-\tilde{g}$ and radius $|\tilde{g}|$ [85], where

$$\tilde{g} = \frac{g_{11}g_{22}}{g_{12}g_{21}} \tag{4.21}$$

An example of the two circles on the γ-plane is shown in Figure 4.3. To calculate a compensator from a specific point on the γ-plane, referred to as γ_0, Equation 4.16 can be substituted into Equation 4.20 to give

$$\gamma_0 = (\alpha-1) = \frac{1}{1+g_{11}\kappa_0}-1, \tag{4.22}$$

[1]Note that the use of β in this chapter is distinct from its use in the rest of this thesis, where it is a positive control effort coefficient-weighting parameter

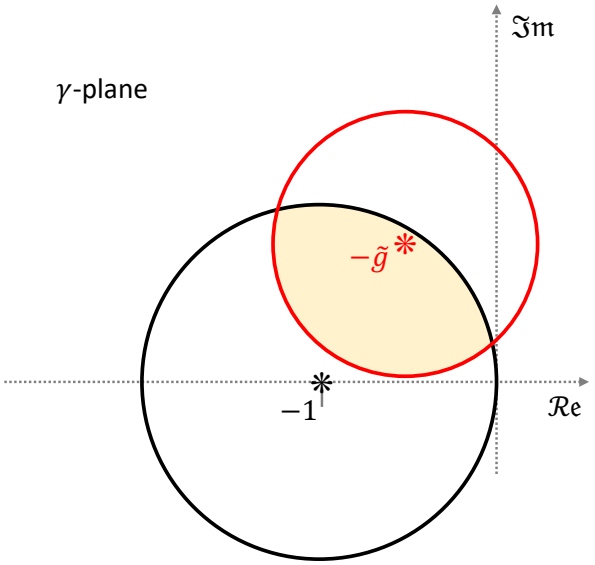

FIGURE 4.3: Mapping of $|\beta + 1| = 1$ onto the complex γ-plane. The black circle corresponds to the local error signal, the red circle corresponds to the remote error signal and the yellow highlighted area where the circles intersect represents a simultaneous reduction in both error signals.

which can be rearranged as

$$\kappa_0 = \frac{\gamma_0}{(1+\gamma_0)g_{11}}. \tag{4.23}$$

Referring to Figure 4.3, the centre point of each of these circles corresponds to a point of the γ-plane that can be used to calculate a compensator that completely cancels, or annihilates the respective error signal. Likewise, if a point on the γ-plane is selected from the edge of one of the circles then this value can be used to calculate a compensator that neither attenuates nor enhances the error corresponding to that circle. Both circles will also intersect at the origin (0,0) of the γ-plane and by referring to Equation 4.23 it can be seen that when γ_0 is equal to zero, κ_0 is equal to zero and there is subsequently no control. If, say, a point is chosen that falls within both circles, then a compensator can be calculated that reduces both the local and remote error. However, if a point is chosen from outside one of the circles then that error signal will be enhanced. It should be noted that due to the formulation of Equation 4.23, annihilation of the local error is impractical because it requires an infinitely large gain. This could be solved by using, for example, an IHC architecture [85].

The controller design presented here is tonal, which means that for each frequency γ_0 must be selected from the γ-plane in order to calculate κ_0. If this selection process is carried out over a broad range of frequencies, a vector of compensator values can be calculated that can be used to design a broadband controller. However, this process is not straightforward, since both the causality and stability of this broadband controller must be considered and this is explored in [85–87].

To avoid predicting unrealistic levels of control, each compensator has been regularised so that the attenuation produced using the feedback controller is limited to 20 dB. To achieve this, Equation 4.23 has been modified by adding a constant number to the plant response. This regularisation number is different for each frequency, however by making this number proportional to the magnitude of the plant response, a general solution can be expressed as

$$\kappa_0 = \frac{\gamma_0}{(1 + \gamma_0 + \xi)g_{11}}. \tag{4.24}$$

Through an iterative approach, it was found that when ξ was assigned a value of 0.111, the compensator calculated using Equation 4.24 was limited to producing a maximum attenuation of 20 dB.

In order to implement the tonal compensator in the time domain, a recursive least squares (RLS) control architecture based on [88] is used here. The RLS controller requires a complex tonal reference signal to be generated artificially, which is used in addition to the error signal to determine the gain and phase difference of the corresponding tonal component of the error signal relative to the reference. Therefore, although a time-advanced reference signal from the disturbance is not required to implement this controller, an estimate of the frequency of the disturbance is required and the tonal reference signal can then be generated at this frequency. A block diagram of this controller is shown in Figure 4.4. In the block diagram shown, $e_l(n)$ is the n-th sample of the error

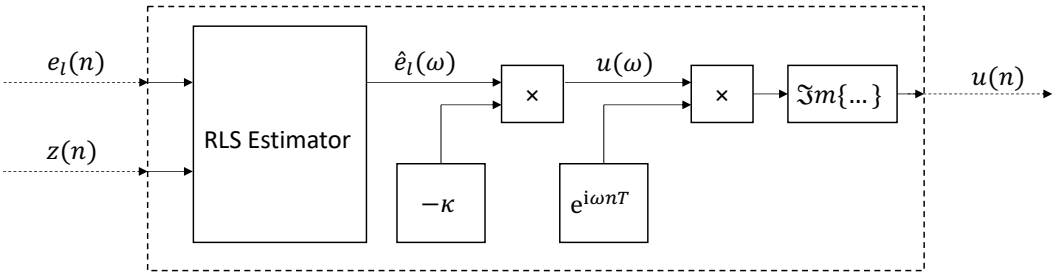

FIGURE 4.4: A block diagram showing the RLS based IHC. The inputs are the local error signal ($e_l(n)$) and a tonal reference signal (z), which are used to calculate the gain (ν) and phase (ϕ) of the tonal component of the error signal relative to the reference signal. The compensator (κ) is then applied in the frequency domain and the signal is transformed back into the time domain. The imaginary, sinusoidal, part of this signal is taken as the control signal.

signal, $z(n)$ is the n-th sample of an artificially generated reference signal and u is the control signal. $\hat{e}_l(\omega)$ is an estimate of the gain and phase of the error signal relative to the reference signal, which can be expressed as

$$\hat{e}_l(\omega) = \nu e^{i\phi}, \tag{4.25}$$

where ν is the gain relative to the reference and ϕ is the phase shift relative to the reference. In order to calculate $\hat{e}_l(\omega)$, the n-th sample of the error signal can be expressed as

a sinusoidal tone relative to the reference,

$$e_l(n) = \nu \sin(\omega n T + \phi) + \epsilon(n), \tag{4.26}$$

where T is the sampling time period, ω is the angular frequency, and ϵ represents random white measurement noise with zero mean. Equation 4.26 can be expanded as

$$e_l(n) = \nu \sin(\omega n T)\cos(\phi) + \cos(\omega n T)\sin(\phi) + \epsilon(n), \tag{4.27}$$

which is condensed to

$$e_l(n) = \theta(n)^T \mathbf{z}(n) + \epsilon(n), \tag{4.28}$$

where

$$\theta(n)^T = \begin{bmatrix} \nu\cos(\phi) & \nu\sin(\phi) \end{bmatrix} \tag{4.29}$$

is the vector containing the real and imaginary parts of the error signal with respect to the real and imaginary parts of the reference signal, which are contained within the vector

$$\mathbf{z}(n) = \begin{bmatrix} \sin(\omega_0 n T) & \cos(\omega_0 n T) \end{bmatrix}^T. \tag{4.30}$$

$\boldsymbol{\theta}_k$ can be estimated from the exponential forgetting RLS algorithm [89] as

$$\theta(n) = \theta(n-1) + \mathbf{K}(n)\left(e_l(n) - \theta(n-1)^T \mathbf{z}(n)\right), \tag{4.31}$$

where

$$\mathbf{K}(n) = \left(1 + \lambda^{-1}\mathbf{z}(n)^T \mathbf{P}(n-1)\mathbf{z}(n)\right)^{-1} \lambda^{-1}\mathbf{P}(n-1)\mathbf{z}(n) \tag{4.32}$$

and

$$\mathbf{P}(n) = \lambda^{-1}\mathbf{P}(n-1) + \lambda^{-1}\mathbf{K}(n)\mathbf{z}(n)^T \mathbf{P}(n-1). \tag{4.33}$$

The λ term in Equations 4.32 and 4.33 is a forgetting factor and takes a real value between 0 and 1. Although it is possible to implement the controller using a gradient descent method as shown in [88], in this study the compensator has been calculated earlier in this section and is implemented directly. An instantaneous inverse Fourier transform is then applied to the frequency domain control signal, $u(\omega)$, and the sinusoidal imaginary part of the subsequent signal is taken as the time domain control signal. Taking the feedback control law from Equation 4.2 and the estimated error signal from Equation 4.25, the time domain control signal [88] can be expressed as

$$u(n) = -\kappa\nu \sin(\omega n T + \phi). \tag{4.34}$$

In this study, the focus has been on a tonal implementation to obtain further insight into how the different feedback compensators affect the taper vibration and reflected wave component. The first limitation to consider arises from the wave component estimation method, which has a low and high frequency limit. These have been previously

discussed in Sections 2.2 and 3.1.1 and the resulting frequency limits are highlighted in Section 4.2.1 for this investigation.

Another limitation of this study is that the robustness of the system and the power requirements have not been considered. However, since the purpose of this study is to provide insight into the tradeoff between minimising the local taper vibration and minimising the reflected wave component in an ABH, rather than implementing the controller in real-time, the robustness and power requirements have not been investigated.

4.2 An Experimental Investigation of a Feedback AABH

This section presents an investigation into the application of the feedback remote damping controller described in Section 4.1. The experimental setup used is presented in Section 4.2.1 and the frequency response functions are shown for g_{11} g_{12} g_{21} and g_{22}. The remote damping circles are then presented for two example frequencies to demonstrate how a compensator is chosen and four compensators are then chosen for each frequency. Section 4.2.3 follows on with the performance results for each compensator, presented over frequency in terms of the reflected wave component and the local taper vibration. The initial analysis has been carried out in the frequency domain. Following this, an IHC architecture [85, 88] has been used to assess the performance of each compensator in the time domain.

4.2.1 Experimental Setup

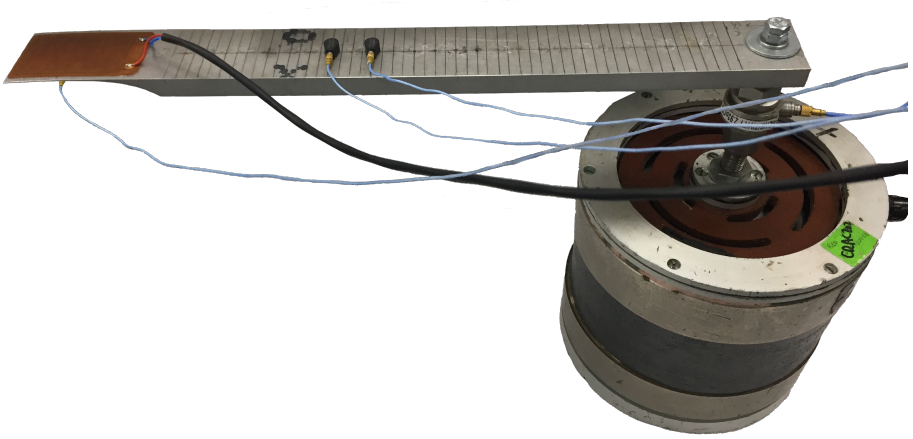

FIGURE 4.5: A picture showing the experimental setup used in this investigation.

The experimental setup presented in Figure 4.1 has been implemented and a picture can be seen in Figure 4.5. This setup is very similar to the setup presented in Section

TABLE 4.1: The dimensions of the experimental setup. Each parameter has a tolerance of $\pm$ 0.1 mm.

Parameter	Beam	ABH termination	Constant thickness termination
Height	10 mm	$(9.5(1-(x/70))^4 + 0.5)$ mm	10 mm
Length	300 mm	70 mm	70 mm
Width	40 mm	40 mm	40 mm

3.2.1, which was used to carry out a feedforward control strategy. However, in this case an extra accelerometer has been attached to the termination to provide a measure of the local termination vibration. An identical setup has also been used for a beam with a constant thickness termination, which has been included for reference. The signals from the accelerometers were filtered with a 10 kHz low pass filter to prevent aliasing and the signals used to drive the shaker and piezoelectric patch were filtered with a 10 kHz low pass reconstruction filter. The DAC/ADC was performed using dSPACE, a rapid prototyping hardware. In addition to the figure showing the setup, the dimensions of the beam with the ABH termination and the beam with the constant thickness termination are shown in Table 4.1. These are the same as the dimensions used in the experimental studies presented in Chapters 2 and 3, and have been reproduced here for convenience. The piezoelectric transducer is also the same component that was used in Chapter 3 and has a length of 61 mm, a height of 0.4 mm, a width of 33 mm and a mass of 2 g. Note that, however, the effective mass of the piezoelectric patch is actually 4 g, which takes into account the mass of the resting wires.

The frequency limits of this investigation are, therefore, the same as those used in Chapter 3, which have been calculated as 400 Hz – 10 kHz. Using a sampling frequency of 22 kHz, the primary responses between the disturbance signal used to drive the shaker and the three accelerometers were measured. The measurements were then repeated whilst driving the piezoelectric transducer to obtain the secondary responses. The frequency responses were then calculated using the H1-estimator. The frequency responses of the accelerometers on the beam section were then used to estimate the frequency response of the reflected wave component using the method described in Section 4.1. The resulting frequency responses are presented in Figure 4.6.

From the frequency responses shown in Figure 4.6, it can be seen that the plant responses of each termination are lower than the primary responses at lower frequencies and higher than the primary responses at higher frequencies. This is partially due to the cut-on frequency of the piezoelectric patch, which is 250 Hz, and also due to the coupling between the piezoelectric patch and the structure at higher frequencies. The cross-over frequency is, however, much lower for the beam with the AABH termination (approximately 1 kHz compared to 2.5 kHz). This implies that the coupling between the piezoelectric patch and the AABH is better at lower frequencies compared to the constant thickness termination. The benefit of this is that low frequency control will require less input energy, which has been demonstrated previously in Chapter 3.

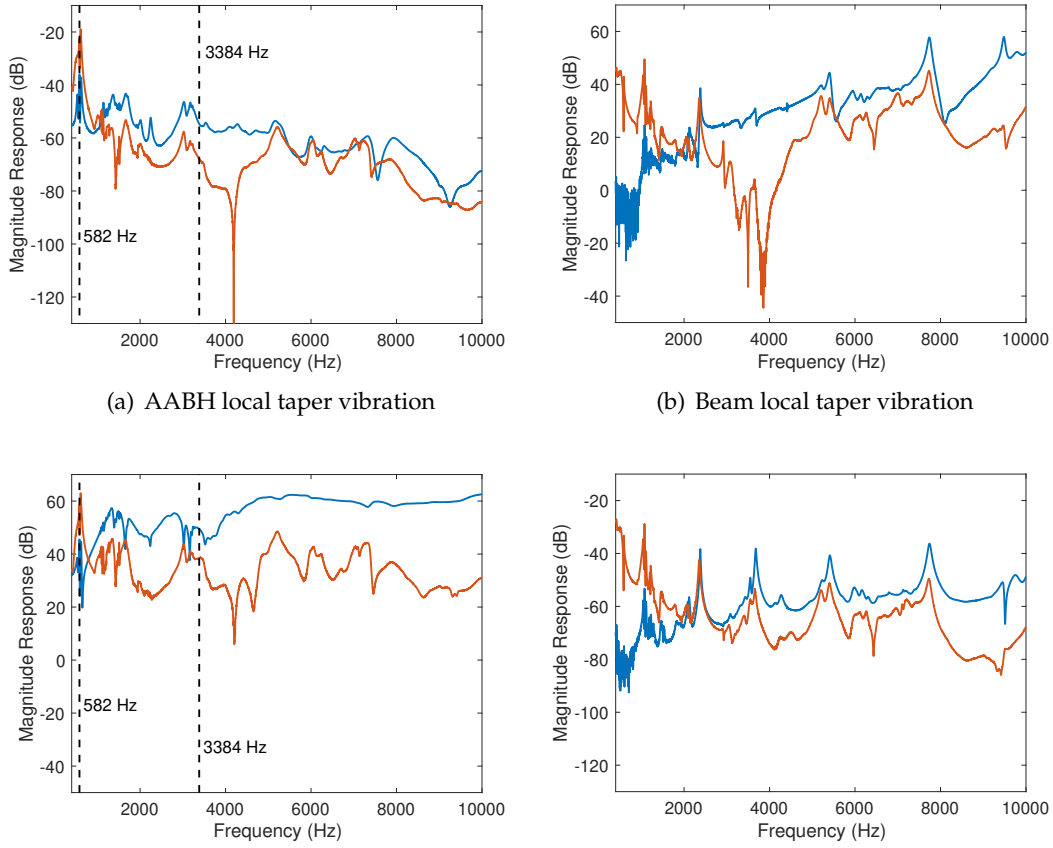

(a) AABH local taper vibration

(b) Beam local taper vibration

(c) AABH reflected wave component

(d) Beam reflected wave component

FIGURE 4.6: The local (local taper vibration) and remote (reflected wave component) frequency responses for the (a, c) beam with the ABH termination and (b, d) the beam with the constant thickness termination. The primary responses are shown by the red lines and the secondary responses are shown by the blue lines. Two frequencies have been highlighted by the black dashed lines and correspond to the examples given in Figure 4.7.

In order to perform the time domain analysis that is presented later in this chapter, FIR filters with 2 coefficients were used to model the frequency responses at each chosen frequency. These FIR filters were estimated using the MATLAB function `invfreqz`.

4.2.2 Compensator Selection

To demonstrate how a compensator can be selected from the controller design method presented in Section 4.1, two examples are given in Figure 4.7 at 582 Hz (on resonance) and at 3384 Hz (off resonance). These have been marked on Figures 4.6(a) and 4.6(c) using black dashed lines. The results presented in Figure 4.7 show a solid-lined black circle that has been plotted in the γ-plane using Equation 4.19 and a solid-lined red circle that has been plotted by mapping Equation 4.15 onto the γ-plane. The asterisks at the centre of each circle represent the minimisation of the respective error and the

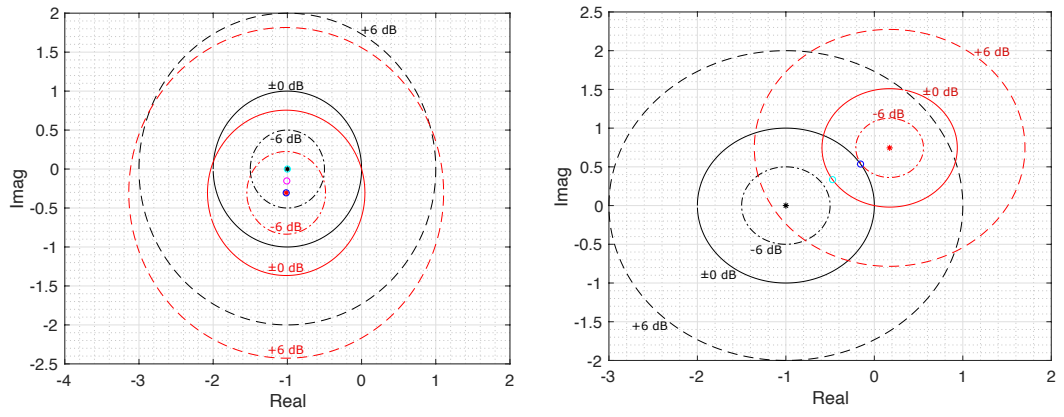

(a) 582 Hz (b) 3384 Hz

FIGURE 4.7: The red circle representing control of the reflected wave component plotted with respect to the black unit circle representing control of the local vibration at (a) 582 Hz and (b) 3384 Hz. The solid lines represent 0 dB of attenuation, the dot-dash lines represent 6 dB of attenuation, the dashed lines represent 6 dB of enhancement and the asterisk represents minimisation of the respective quantity. The cyan circle represents the best possible control of the local taper vibration without enhancing the reflected wave and the blue circle represents the best possible control of the reflected wave without enhancing the local taper vibration. The magenta circle in (a) is the point that gives an equal reduction in both error signals.

small blue and cyan circles represent the best control cases possible without enhancing either the local taper vibration or the reflected wave component. Finally, the dot-dashed lines represent 6 dB of attenuation and the dashed lines represent 6 dB of enhancement in the respective error signal.

In Figure 4.7(a), it can be seen that the (-1,0) point that corresponds to minimisation of the local vibration lies within the -6 dB circle of control of the reflected wave. Therefore, at 582 Hz, minimising the local taper vibration will also attenuate the reflected wave, in this case by approximately 10 dB. Minimising the reflected wave component will also result in attenuation of the local taper vibration because the red asterisk lies within the -6 dB dot-dashed black line. At this frequency, either of the two errors can be minimised without enhancing the other and therefore the cyan circle, that represents reducing the local taper vibration without enhancing the reflected wave, and the blue circle, that represents reducing the reflected wave without enhancing the local taper vibration, are both located on the minimisation asterisks. The final control case highlighted in Figure 4.7(a) is marked by a magenta circle. This point lies midway between the centres of both circles and can be used to calculate a compensator that equally controls the reflected wave component and the local taper vibration.

The results in Figure 4.7(b) show a different set of circles for this control system, at a frequency where minimising either quantity will result in enhancement of the other. From these results it can be seen that a compensator that minimises the local taper vibration (from the (-1,0) point) will slightly enhance the reflected wave component (by

approximately 5 dB), whilst a compensator that minimises the reflected wave component (from the -$\tilde{g}$ point) will enhance the local taper vibration by approximately 3 dB. At this frequency, it can be seen that the largest reduction in the local taper vibration that can be achieved without enhancing the reflected wave component will occur if a compensator is calculated using the point at (-0.5,0.3), which is highlighted by a cyan circle. In this case, approximately 4 dB of attenuation is achieved in the local taper vibration without enhancing the reflected wave component. It can also be seen that if a compensator is calculated using the point (-0.2,0.5), highlighted by a blue circle, then approximately 6 dB of attenuation can be achieved in the reflected wave component without enhancing the local taper vibration.

4.2.3 Frequency Domain Performance

Using the four control compensator selection criteria described previously, the compensator responses have been calculated over frequency and their performance can be seen in Figure 4.8 over a bandwidth of 400 Hz to 10 kHz. In each case, regularisation has been added to the selected local plant response, g_{11}, to constrain the maximum attenuation to approximately 20 dB for clarity and to avoid predicting unrealistic levels of control. From the results presented in Figure 4.8, it can be seen that when control is set to minimise the local taper vibration (shown by the solid blue lines), the vibration in the taper is reduced by approximately 20 dB at all frequencies, which is simply limited by the level of regularisation used in the study. The corresponding reflected wave component is generally unchanged, varying by approximately $\pm$ 1 dB over the bandwidth presented. However, there are specific frequencies and frequency bands that are attenuated or enhanced slightly more. For instance, at 582 Hz, the resonant frequency used as an example in Figure 4.7(a), there is approximately 10 dB of attenuation, which is consistent with the prediction. Additionally, there is also a simultaneous reduction at 4198 Hz, which is situated very close to a large enhancement detailed below. The frequency bands 600 Hz – 1 kHz, 1.4 kHz – 1.8 kHz and 2.8 kHz – 4.5 kHz are enhanced by up to 30 dB. The largest of these enhancements occurs around 4190 Hz and, by referring back to Figure 4.6(c), it can be seen that there is a strong anti-resonance in the primary response of the reflected wave component at this frequency. The enhancement in the reflected wave component occurs because, although minimising the vibration in the taper perfectly dampens the taper, this control strategy introduces a high impedance change at the ABH junction, which can be considered as a zero velocity boundary condition. This essentially truncates the termination at the ABH junction, making it equivalent to a flat termination. This study has shown that minimising vibration in the taper is not a suitable control strategy if the objective is to maintain or improve the damping performance of the ABH.

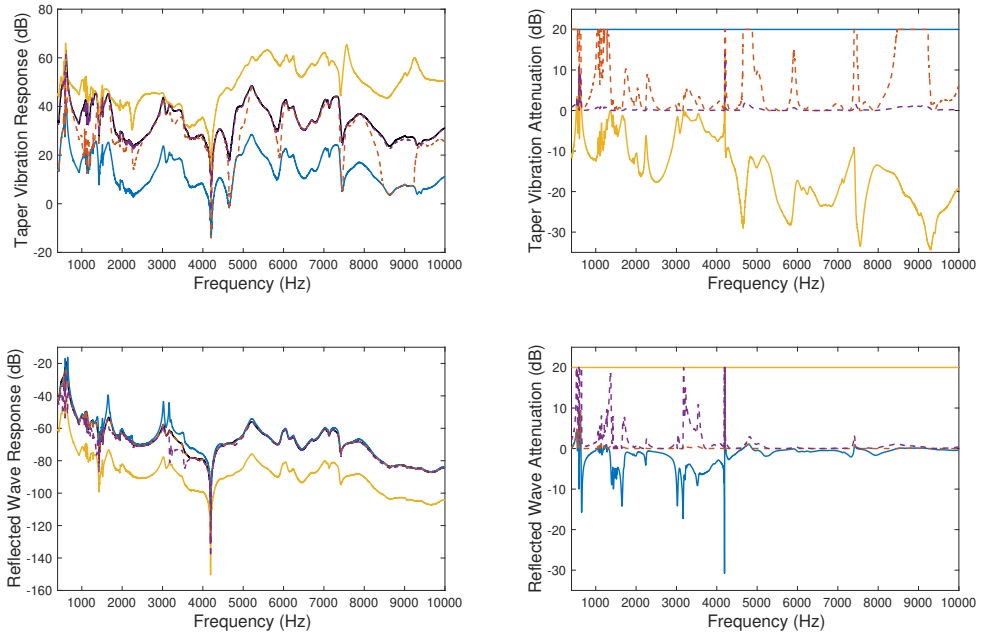

FIGURE 4.8: Feedback control implemented for the four cases and presented in terms of the responses and attenuation. The effect that each compensator has in the local vibration is shown in the top plots and the effect that each compensator has in the reflected wave is shown in the bottom plots. The uncontrolled case is represented by 0 dB of attenuation, the local minimisation case is represented by a solid blue line, the reflected wave minimisation case is represented by a solid yellow line, the local reduction without enhancement of the reflected wave case is represented by a dashed red line and the reflected wave reduction without enhancement of the local vibration is represented by a purple dashed line.

When control is set to minimise the reflected wave component (shown by the solid yellow lines), the results in Figure 4.8 show that the reflected wave component is reduced by approximately 20 dB at all frequencies, which is again limited by the selected level of regularisation. It can be seen from the response in the taper, that this control strategy leads to a significant increase in the taper vibration of up to 30 dB. There are, however, three narrow frequency bands where the local vibration is reduced by up to 10 dB and these are around 582 Hz, 620 Hz and 4198 Hz. This control strategy is of particular interest because one of the key performance criteria of an ABH is its reflection coefficient. It has been previously shown that the reflection coefficient can be controlled using a feedforward control architecture in Chapter 3 and that this control strategy resulted in an enhancement of the taper response. This study demonstrates the same relationship between the reflection coefficient and the taper vibration amplitude.

In order to reduce effects of structural fatigue, the results from the two control strategies that focus on minimising the reflected wave without enhancing the level of vibration in the taper or, alternatively, minimising the local vibration in the taper without enhancing the reflected wave component have been presented. In the former case, the

performance is shown by the dashed purple line in Figure 4.8 and it can be seen that there are a number of narrow bandwidths where the reflected wave can be reduced by up to 20 dB (limited by the regularisation) without enhancing the taper vibration. These narrow bandwidths can all be seen to occur below 5 kHz, except one small reduction at approximately 7.5 kHz. Although this control strategy is not particularly effective at higher frequencies, it should be noted that the uncontrolled ABH already provides a high level of damping and so high frequency vibrations are unlikely to cause issues in practice. When the latter control strategy is implemented to reduce the local taper vibration without enhancing the reflected wave component, it can be seen from the red dashed line in Figure 4.8 that a reduction in the local vibration can be achieved over a number of frequency bands, covering the full bandwidth presented. In application, the choice of control strategy will depend on the nature of the problem and a combination of the different control strategies will likely produce the best solution to a broadband problem.

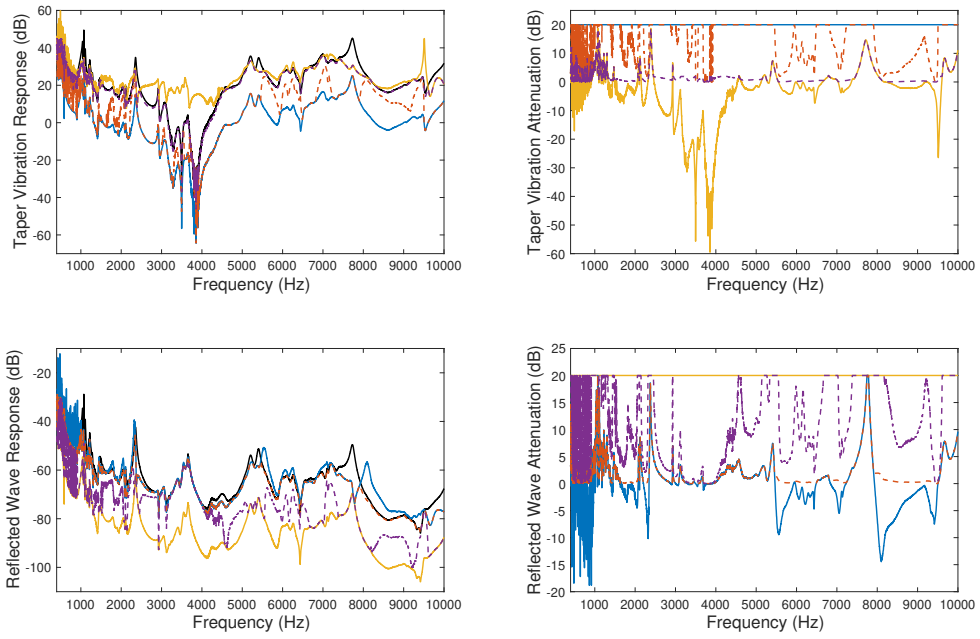

(a) Beam control responses

(b) Beam control attenuation

FIGURE 4.9: Feedback control implemented for the four compensators presented in terms of the responses and attenuation. The effect of control on the local taper vibration is shown in the top plots and the effect of control on the reflected wave component is shown in the bottom plots. The uncontrolled case is represented by 0 dB of attenuation, the local minimisation case is represented by a solid blue line, the reflected wave minimisation case is represented by a solid yellow line, the local reduction without enhancement of the reflected wave case is represented by a dashed red line and the reflected wave reduction without enhancement of the local vibration is represented by a purple dashed line.

The results presented in Figure 4.9 show the same four control strategies implemented

for a beam with the constant thickness termination. These results provide a comparison, however they do not take into account the benefits of the AABH that were discussed in Chapter 3, namely the lower computational cost required for real-time implementation and the lower control effort required to perform control. It can be seen from the results in Figure 4.9 that when the local taper vibration is minimised, the reflected wave component is enhanced at some frequencies and attenuated at other frequencies. However, the magnitude of the enhancement is smaller than that shown in Figure 4.8 for the AABH termination. When the reflected wave component is minimised, it can be seen that there is a large enhancement in the response of the termination between 2.5 kHz and 5 kHz, however this has occurred because over this frequency band the primary response, shown in Figure 4.6(b), is very low. At all other frequencies, there is generally only a small amount of enhancement or attenuation. These results are consistent with the findings of the feedforward control study presented in Chapter 3. If the reflected wave component is controlled without enhancing the local taper vibration, it can be seen that there is a simultaneous reduction of both error signals over some narrow bands, particularly around 2.5 kHz and 7.75 kHz. In addition, there are a number of frequency bands where the reflected wave component can be minimised without enhancing the local taper vibration. Similarly, when the local taper vibration is controlled without enhancing the reflected wave, minimisation of the taper vibration can occur without enhancing the reflected wave at the majority of frequencies presented.

Compared to the AABH termination, it is clear that the constant thickness active termination is more effective for simultaneous control because the reflected wave component and termination vibration level are more strongly coupled due to there being no significant impedance change between the beam and the termination. Referring back to the uncontrolled reflection coefficient presented in Chapter 3, the constant thickness termination exhibits near perfect reflection, which demonstrates that an incident wave is not significantly changed as it reflects from the termination. In contrast, the wavelength change and absorption that occurs along the length of the ABH makes the coupling between the reflected wave component and the local taper vibration more complex. Furthermore, these results do not take into account the reduced computational and electrical power requirements of the AABH termination that have been demonstrated in Chapter 3. The most appropriate termination for a specific application will, therefore, depend on the requirements of the application, the resources available and the constraints imposed on the stress of the termination. For example, the increased vibration in the ABH may result in increased stress, however a constant thickness termination may require more powerful components to achieve a suitable level of control. A solution could, therefore, be to use an AABH termination with a limit set on the acceptable level of vibration in the system.

4.2.4 Time Domain Performance

The results presented in this section serve to demonstrate the performance of each of the control strategies in the time domain via simulation. The results are presented in terms of the AABH as a proof of concept and so no results for the standard beam are shown. The compensators used to obtain the results in Section 4.2.3 have been implemented at each frequency using the RLS based IHC architecture [88] that was described in Section 4.1. A pure sinusoidal tone was used as the disturbance signal. The two frequencies, 582 Hz and 3384 Hz, presented as an example in Section 4.2.2 have been used to demonstrate each of the compensator selections in the time domain. The local taper vibration and reflected wave component error signals are shown before and after control, which has been turned on at $t = 1s$, in Figure 4.10 for each of the cases. The error signal has been normalised so that the pre-control level is ± 1 in each case to improve the clarity of the results. Each factor of 2 represents an increase or decrease of 6 dB in the error signal. For each case, Table 4.2 shows the increase or decrease in the error signal in decibels relative to the respective uncontrolled level.

TABLE 4.2: The change in the local and reflected wave component (ϕ^-) error signals before and after control.

Frequency	Control Case	Error	Level Change
3384 Hz	Local Minimisation	e_l	-20 dB
		e_{ϕ^-}	+5 dB
3384 Hz	Local Reduction Without Enhancing ϕ^-	e_l	-4 dB
		e_{ϕ^-}	$\pm$0 dB
3384 Hz	ϕ^- Minimisation	e_l	+3 dB
		e_{ϕ^-}	-20 dB
3384 Hz	ϕ^- Reduction Without Enhancing Local Vibration	e_l	$\pm$0 dB
		e_{ϕ^-}	-6 dB
582 Hz	Simultaneous Reduction	e_l	-15 dB
		e_{ϕ^-}	-15 dB

From the results shown in Figure 4.10(a) and Table 4.2, it can be seen that at 3384 Hz the local taper vibration can be reduced by 20 dB, which causes a 5 dB enhancement of the reflected wave component. These levels are consistent with the frequency domain results shown in Section 4.2.3. The results in Figure 4.10(b) and Table 4.2 show that approximately 4 dB of attenuation can be achieved in the local taper vibration without enhancing the reflected wave component. These results are also consistent with the frequency domain simulation results presented in Section 4.2.3. If, instead, the reflected wave component is minimised then from the results shown in Figure 4.10(c) it can be seen that there is an enhancement in the local taper vibration. Referring to Table 4.2, it can be seen that this enhancement is 3 dB. If it is ensured that there is no enhancement in the local taper vibration, the controller can achieve approximately 6 dB of attenuation in the reflected wave component, which is shown both in Table 4.2 and in Figure 4.10(d). Examining the implementation of control at 582 Hz, it was shown in Sections

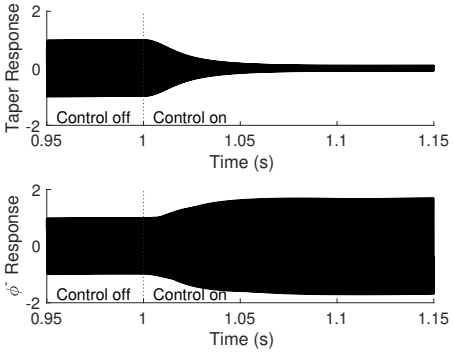

(a) 3384 Hz Local Minimisation

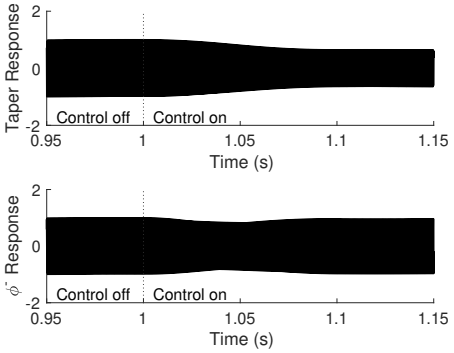

(b) 3384 Hz Local Control

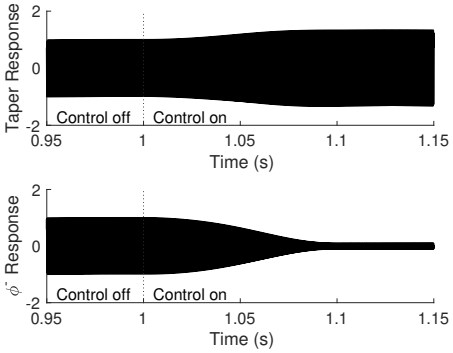

(c) 3384 Hz Remote Minimisation

(d) 3384 Hz Remote Control

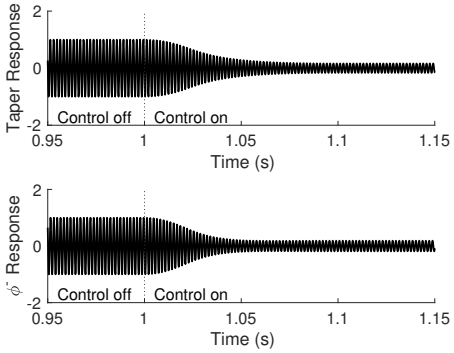

(e) 582 Hz Simultaneous Control

FIGURE 4.10: The local and remote error signals for each of the time domain cases, normalised with respect to the pre-control level.

4.2.2 and 4.2.3 that simultaneous reduction could be achieved in both the local taper vibration and the reflected wave component. To demonstrate this, a compensator has been calculated from the midpoint on the γ-plane between the two circles, which was highlighted by the magenta circle in Figure 4.7(a). Implementing this compensator in the time domain gives the results presented in Figure 4.10(e), which show the simultaneous reduction in both error signals. Referring to Table 4.2, it can be seen that each error signal is attenuated by approximately 15 dB. This specific case was not presented in the frequency domain implementation, however, the results are very similar to those obtained by implementing the compensators that minimise each error signal and so are considered consistent.

It is also interesting to note that for each control case, the decay profile is different and this can be linked to the γ-plane circles presented previously in Figure 4.7. For example, at 3384 Hz, to control the taper response without enhancing the reflected wave component the controller must converge from the (0,0) point on the γ-plane to the location on the 0 dB reflected wave response circle closest to the centre of the local taper response circle (highlighted by the cyan circle in Figure 4.7(b)). Drawing a straight line between these two points will bisect the 0 dB reflected wave response circle and therefore the convergence in Figure 4.10(b) shows a slight attenuation in the reflected wave response before returning to the original level. At each frequency, the dynamics between the reflected wave component and the local taper vibration will be different, resulting in a unique decay profile for each case.

4.3 Summary

An investigation into the use of feedback control in an active ABH has been presented in this chapter. A geometric controller design used for remote damping control has been used to examine the tradeoff between controlling the local taper vibration and controlling the reflected wave component. Four different control cases were chosen at each frequency and a compensator was calculated for each. A frequency domain implementation has shown that minimising the local taper vibration produces a small amount of unwanted enhancement in the reflected wave at frequencies below 5 kHz. Intuitively, minimising the taper vibration imposes a zero velocity boundary condition at the ABH junction, which can therefore be approximated as a constant thickness flat termination. This indicates that a control strategy such as pure velocity feedback control is unlikely to have any significant performance benefits, except perhaps at one or two very specific frequencies, and an alternative controller is required. It has also been shown that if the reflected wave component is minimised, similarly to the feedforward control strategy presented in Chapter 3, the local vibration in the taper is greatly enhanced. Although this leads to an improvement in ABH performance in terms of a low reflection coefficient, the subsequent enhancement of vibration in the thin region

of the taper may lead to early failure due to increased structural fatigue. In addition, designing a stable and robust feedback controller that greatly enhances the local vibration may be difficult. If a constraint is set so that the reflected wave is controlled without enhancing the taper vibration, it has been shown that some level of reduction in the reflected wave can be achieved below 5 kHz, however there are only two frequencies where a simultaneous reduction is possible. It should be noted that one of these frequencies is a resonance and so this control strategy may be of use if examining the radiated sound from the structure. Above 5 kHz, this control strategy provides very little benefit. If a constraint is set so that the taper vibration is controlled without enhancing the reflected wave, a reduction in the local taper vibration is achievable at a significant number of frequencies across the full 400 Hz – 10 kHz bandwidth presented, including resonances. This control strategy may, therefore, be useful in applications where the ABH provides enough damping passively but is suffering from fatigue due to high amplitude vibration in the taper. These final two control strategies have shown that a controller can be designed for applications where there are constraints on the performance or maximum vibration level. The same investigation has been carried out using a beam with a constant thickness termination, and it has been found that simultaneous control of both error signals can be achieved at more frequencies compared to the AABH termination, which has been linked to the near perfect reflection from the uncontrolled termination. However, it has also been noted that these results do not take into account the main benefits of using an AABH, namely the reduced computational and electrical power requirements. Finally, a time domain study has shown that a RLS based IHC can be used to implement each of the compensators effectively in the time domain and the results shown were consistent with the results from the frequency domain implementation.

So far, Chapters 3 and 4 of this thesis have provided detailed insight into the implementation of active control using an AABH beam termination. Whilst this termination has been shown to be effective, many vibration problems occur in plates and Chapter 5 will, therefore, extend the concept of the AABH to a plate.

Chapter 5

Feedforward Active Control of a Plate with Embedded ABHs

Up to this point in this thesis, the focus of the work has been on ABHs operating as beam terminations. Although this provides interesting physical insight into the mechanisms by which ABHs and AABHs can achieve effective vibration control, many practical vibrating structures have more complex geometries. Therefore, this chapter will present an extension of the ABH concept, and particularly the AABH concept developed within this thesis, to a two-dimensional plate structure. In a two-dimensional structure, an ABH can be manufactured into the plate as a revolved taper that results in a disk-like indentation. An example of an embedded ABH can be seen in Figure

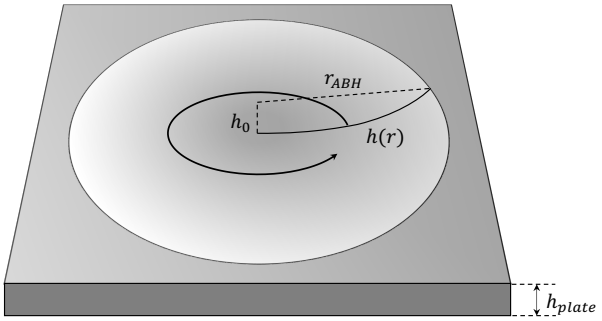

FIGURE 5.1: A diagram showing how an ABH is embedded into a plate.

5.1, where r_{ABH} is the radius of the ABH, h_0 is the difference between the height of the plate, h_{plate}, and the minimum taper height of the ABH, h_{min}, and $h(r)$ is the height function used to define the taper of the ABH. Alternatively, ABHs can be attached to the surface of the plate with designs such as those proposed in [32–34]. Similarly to ABHs on beams, a power law (or other function [22, 49]) is usually used to define the taper and damping is required to achieve good performance. Unlike the beam-based literature, there has been significant focus on the radiated sound from plate based

ABHs [53, 90–93], as well as developments to understand the way that vibrational energy propagates though the circular ABHs [41, 43, 44]. The low frequency performance of ABHs has been shown in previous chapters to be characterised by the narrow bands of low reflection which, as frequency is increased, become wider and thus the damping effect becomes more broadband. Although the low frequency performance of ABH plates can be improved by, for example, increasing the size of the ABHs to decrease the local modal frequencies or by integrating the ABHs into a sandwich structure [94], these solutions are not always practical due to constraints on the size and weight of the host structure. Chapters 3 and 4 have presented an active solution to this problem, where it has been shown that feedforward and feedback active control strategies can be applied to a beam with an AABH termination to improve the performance. Both control strategies examined the capability of the active system to reduce the reflected wave component and thus the reflection coefficient of the termination. For a plate with embedded ABHs, the reflection coefficient with respect to structural waves is less obviously defined and, therefore, previous research on ABHs embedded in plates has focused on different structural metrics, such as surface mobility [32, 43] and mean-squared acceleration/velocity [49, 53, 91].

To examine the performance of plate based AABHs, this chapter presents an investigation into the active control of a plate with five embedded AABHs and the performance is compared to an equivalent active control system applied to a conventional flat plate. The performance of both structures has also been examined when passive damping treatments are applied. Since, as mentioned above, the reflection in a plate is not well defined with respect to structural waves, the mean-squared acceleration has been adopted as a performance metric. A multichannel, feedforward, global control strategy has been utilised and an investigation has been carried out into the minimisation of the vibration of the plate. This chapter is organised as follows. The experimental setup is presented in Section 5.1 and the multichannel feedforward controller formulation is presented in Section 5.2. Section 5.3 presents the experimental results, starting with an analysis of the structural responses. A plant modelling study has subsequently been carried out to examine the computational requirements associated with modelling the plant responses and the results from this study are presented in Section 5.3.2. The required control filter length has then been investigated in Section 5.3.3 and this study is followed by the results from a time domain investigation into the minimisation of the global vibration of the plate, which is presented in Section 5.3.4. Finally, the work presented in this chapter has been summarised in Section 5.4.

5.1 Experimental Setup

The experimental setup used to investigate the performance of a plate with embedded AABHs is shown in Figure 5.2 and a more detailed diagram of the top surface of

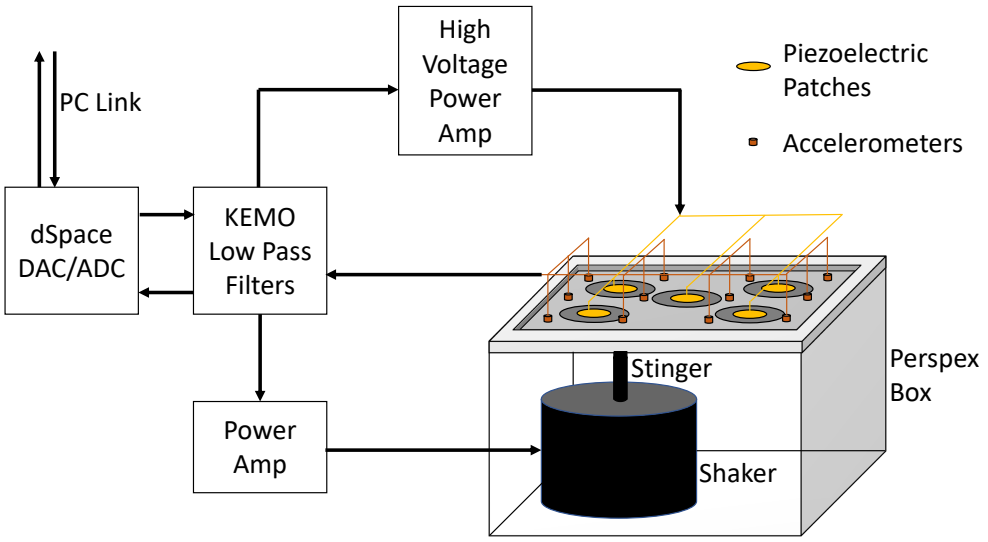

FIGURE 5.2: The plate mounted on a perspex box that can be driven by both the shaker and each of the piezoelectric patches attached to the ABHs. A high voltage amplifier is required to drive the piezoelectric patches and low pass filters have been used for signal anti-aliasing and reconstruction.

the plate is shown in Figure 5.3. The dimensions of the system and some information about the damping and piezoelectric patches are shown in Table 5.1. The plate has been bolted onto the top surface of a perspex box using a metal edge clamp, which is 63 mm wide and reduces the effective surface area of the plate from 475 mm by 375 mm to 412 mm by 312 mm. The shaker has been connected to the underside of the plate using a stinger and the accelerometers have been attached to the top surface of the plate using wax. The piezoelectric patches have also been attached to the top surface of the plate, co-located with the centre of each embedded ABH. By referring to the damping placement optimisation presented in [53], covering the central region of the ABH produces the optimal vibration absorption below the cut-on frequency of the ABH. Additionally, the central location gives better coupling between the piezoelectric patch and the plate due to the thin region of the ABH. The primary disturbance has been generated by driving the shaker with white noise and the control sources have been generated by driving the piezoelectric patches via a feedforward control strategy that will be described in Section 5.2. The structural response of the plate can be measured using the evenly distributed array of 12 accelerometers. This arrangement of accelerometers has been chosen so that the separation of the sensors is 6 cm, which corresponds to the flexural wavelength of a 16 kHz wave in the plate with the properties described in Table 5.1. The signals used to drive the shaker and piezoelectric patches have been passed through low pass reconstruction filters and the signals from the accelerometers have been passed through low pass anti-aliasing filters. dSpace, a rapid prototyping DSP system, has been used to connect the setup to a computer. The upper frequency of interest in this investigation has been defined by the cutoff frequency of the filters as 10 kHz and so the separation of the sensors is small enough to meet the Nyquist spatial

TABLE 5.1: Information about the plates and treatments used in the experimental setup.

Variable	Value
Plate length	475 mm ± 1 mm (412 mm with baffle)
Plate width	375 mm ± 1 mm (312 mm with baffle)
Plate height	6 mm ± 0.1 mm
ABH radius	50 mm ± 0.1 mm
ABH minimum height	0.5 mm ± 0.1 mm
ABH power law	3 ± 0.1
Plate mass with ABHs	2.545 kg
Plate mass without ABHs	2.886 kg
Henley's damping mass per ABH	17 g ± 0.5 g
Piezoelectric patch mass	2 g ± 0.5 g (4 g including resting wire mass)
Piezoelectric patch radius	25 mm
Piezoelectric patch height	0.5 mm
Piezoelectric patch cut-on frequency	250 Hz

sampling limit. In order to contextualise the performance, two plates have been used,

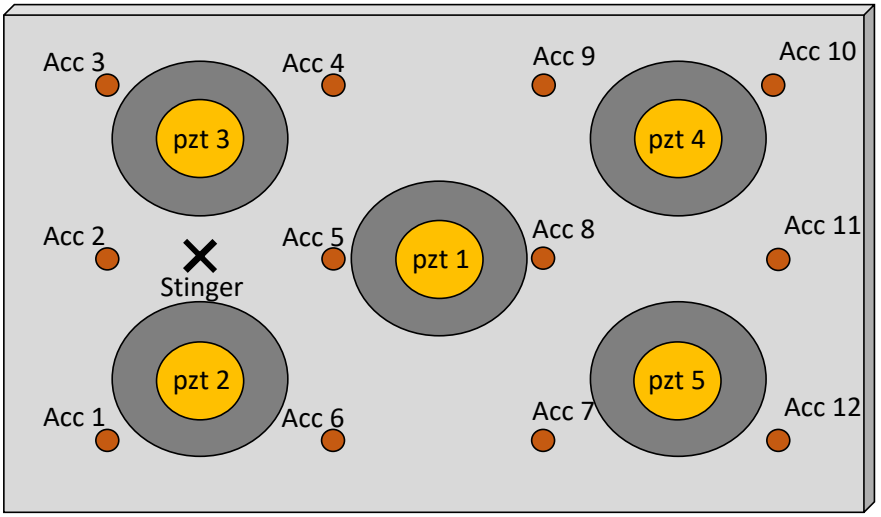

FIGURE 5.3: The surface of the plate showing the location of the accelerometers, ABHs, piezoelectric patches and stinger mount.

one embedded with ABHs and one without ABHs. The ABHs have been manufactured into the plate in five locations; one located at the centre of the plate and the other four located at the centre of each of the four quadrants as shown in Figure 5.3. The lay-out of these ABHs is based on the layout of control actuators presented in [95], which considers a clamped plate with similar dimensions and shows that this arrangement of actuators can be used to effectively control low order plate modes. This layout is also

representative of a segment of the 13 ABH plate from [41], which has been shown to perform similarly to the plate with a more dense layout of ABHs. In total, 8 different variations of the experimental setup have been used. Each plate has been tested with no treatment, treatment with Henley's yellow compound [77], treatment with piezoelectric patches, and treatment with both Henley's compound and piezoelectric patches. The Henley's damping material has been applied to the curved side of the ABH so that the piezoelectric patches could be applied to the flat side to reduce pre-stress. The piezo patches have been custom made by PI ceramic, but share the same operating characteristics and thickness as the P-876.A12 patch shown in [82]. When compared to the rectangular piezoelectric patches used on the ABH beam termination in Chapters 3 and 4, these circular piezoelectric patches are 0.1 mm thicker and contain a piezoceramic layer that is twice as thick, which gives an operating voltage range that is twice that of the rectangular patches. The cut-on frequency of the patches is 250 Hz, which introduces a low frequency limit for control. Anti-aliasing and reconstruction filters have been used in this investigation and are all KEMO low pass filters set with a cut-off frequency of 10 kHz. Therefore, in order to measure the responses of each plate, a sampling frequency of 22 kHz has been chosen because it equates to a Nyquist frequency of 11 kHz and accommodates for the 0 – 10 kHz frequency range of interest. In addition to the sampling frequency used to measure the plate responses, a second sampling frequency of 4 kHz (equating to a 2 kHz Nyquist frequency) has been selected to implement the control strategy that will be presented in Section 5.2. The justification for this second control frequency will be made in Section 5.3.1.

Each of the ABH indentations has been defined by revolving a 2D taper about its tip. Each taper has been defined as

$$h(r) = \varepsilon \left(1 - \frac{r}{r_{ABH}}\right)^{\mu} + h_{min}, \tag{5.1}$$

where $\varepsilon = h_{plate} - h_{min}$ is a scaling factor, h_{plate} is the plate height, h_{min} is the minimum height that the taper reaches, r_{ABH} is the radius of the taper, r ranges from 0 to r_{ABH} and μ is the power law used to define the taper gradient. The taper dimensions have been selected by considering similar examples in the literature [43, 44, 57] as well as with guidance from the parametric study presented in Chapter 2 for a one-dimensional taper, which showed that for a taper length of 5 cm (and thus a 10 cm diameter if revolved) and a tip height of 0.5 mm, the optimum power law would be approximately 3. It may be appropriate to conduct a similar study to that presented in Chapter 2 for the two-dimensional plate ABH, however, in order to focus this thesis on the novel AABH technology, this has not been conducted here. The cut-on frequency of an ABH with the dimensions detailed above can be estimated as the frequency at which the wavelength in the ABH becomes comparable to the size of the ABH [43, 46, 47]. Using the method outlined in [46, 47], this gives a value of approximately 1.4 kHz. From the difference in the plate mass with and without the ABH features, shown in Table 5.1,

it can be seen that each embedded ABH removes 68.2 g of aluminium from the plate, which is significantly more that the mass of either the Henley's damping compound or piezoelectric patch that is added to improve the passive performance. With both damping and piezoelectric patches applied, the total mass of the ABH plate is 246 g lighter than the constant thickness plate with no treatment. If treatment is applied to both plates, the ABH plate is 341 g lighter than the constant thickness plate. Regardless of the damping added, the ABH plate offers a lighter weight structure with superior passive broadband performance.

Figure 5.4(a) shows a photo of the full setup of the box with the mounted plate and the large shaker inside the box that has been driven with the primary disturbance signal. This photo also shows the locations of the 12 accelerometers and the 5 piezoelectric

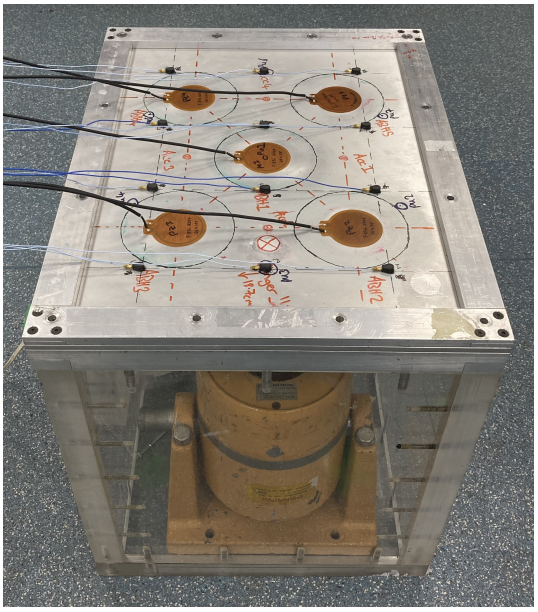

(a) Piezo and accelerometer locations

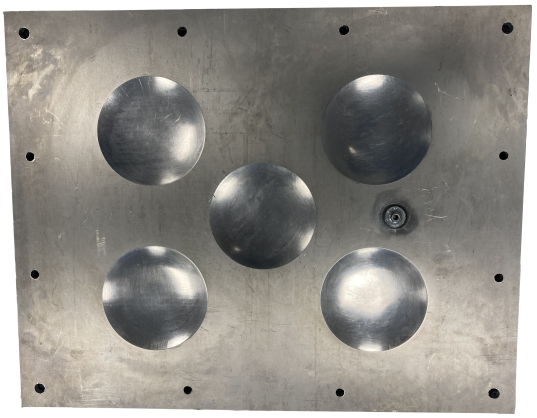

(b) Undamped ABHs

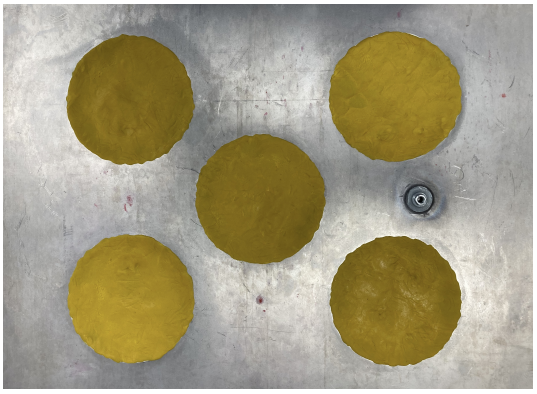

(c) Damping placement

(d) Stinger location

FIGURE 5.4: The experimental setup used to measure the structural responses of the plate with embedded ABHs and the constant thickness plate.

patch actuators mounted on the top surface of the clamped plate. Figure 5.4(b) shows a photo of the underside of the plate where the ABHs have been embedded and Figure 5.4(c) shows a photo of the ABHs with Henley's yellow compound applied over the surface of each ABH indentation. Figure 5.4(d) shows a photo of the stinger attached to the underside of the plate.

5.2 Controller Formulation

A block diagram of the feedforward control system used in this study is shown in Figure 5.5. The reference signal, x, is taken from the signal that is used to drive the shaker

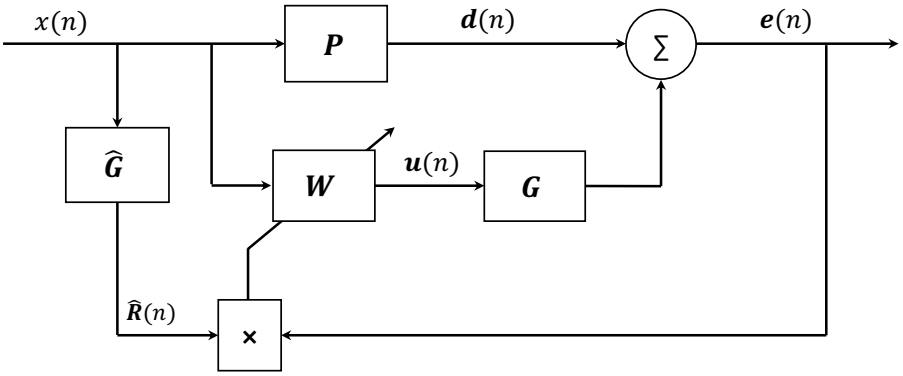

FIGURE 5.5: A block diagram showing the feedforward control system that has been used to control the structural vibration of the plate with AABHs.

and thus a perfect reference signal is assumed in this case. The reference signal is filtered by $\widehat{\boldsymbol{G}}$, which is the matrix of estimated plant responses between the voltage inputs to the piezoelectric patches and the output signals from the accelerometers. The matrix of filtered reference signals, $\hat{\boldsymbol{R}}$, and the vector of error signals from the accelerometers, $\boldsymbol{e}$, are then used to update the controller, $\boldsymbol{W}$. The reference signal is filtered by the controller to generate the vector of control signals, $\boldsymbol{u}$, which are used to drive the piezoelectric patches to minimise the primary disturbance. Although the controller can be implemented adaptively using, for example, the FxLMS algorithm, to ensure that the limitations on the maximum control performance are clearly demonstrated the optimum matrix of control filter coefficients can be calculated using the derivation shown in Section 5.2.1 of [81]. In this investigation, only one reference signal is used and so the controller formulation is slightly simplified. To start, the error signal measured at the l-th accelerometer can be written as

$$e_l(n) = d_l(n) + \sum_{m=1}^{M} \sum_{j=0}^{J-1} g_{lmj} u_m(n-i), \tag{5.2}$$

where g_{lmj} is the j-th coefficient of a J-th order FIR filter that represents the plant response between the m-th piezoelectric patch and the l-th accelerometer. The control signal used to drive the m-th piezoelectric patch can be expressed as

$$u_m(n) = \sum_{i=0}^{I-1} w_{mi} x(n-i), \tag{5.3}$$

where w_{mi} is the i-th coefficient of an I-th order FIR filter. The error signal of the l-th sensor can be rewritten by substituting Equation 5.3 into Equation 5.2 to give

$$e_l(n) = d_l(n) + \sum_{m=1}^{M} \sum_{j=0}^{J-1} \sum_{i=0}^{I-1} g_{lmj} w_{mi} x(n-i-j). \tag{5.4}$$

Assuming that the filters are time invariant, Equation 5.4 can be rewritten as

$$e_l(n) = d_l(n) + \sum_{m=1}^{M} \sum_{i=0}^{I-1} w_{mi} \hat{r}_{lm}(n-i), \tag{5.5}$$

where the filtered reference signal is given by

$$\hat{r}_{lm}(n) = \sum_{j=0}^{J-1} g_{lmj} x(n-j). \tag{5.6}$$

Equation 5.5 can be expressed in vector form as

$$e_l(n) = d_l(n) + \sum_{i=0}^{I-1} \boldsymbol{w_i}(n) \hat{\boldsymbol{r}}_{\boldsymbol{l}}(n-i), \tag{5.7}$$

where

$$\boldsymbol{w_i} = \begin{bmatrix} w_{1i} & w_{2i} & \cdots & w_{Mi} \end{bmatrix}^{\mathrm{T}} \tag{5.8}$$

and

$$\hat{\boldsymbol{r}}_{\boldsymbol{l}}(n) = \begin{bmatrix} \hat{r}_{l1}(n) & \hat{r}_{l2}(n) & \cdots & \hat{r}_{lM}(n) \end{bmatrix}^{\mathrm{T}}. \tag{5.9}$$

The error signals at all L sensors can be written as

$$\boldsymbol{e}(n) = \begin{bmatrix} e_1(n) & e_2(n) & \cdots & e_L(n) \end{bmatrix}^{\mathrm{T}}, \tag{5.10}$$

and the disturbance signal at all L sensors can be written as

$$\boldsymbol{d}(n) = \begin{bmatrix} d_1(n) & d_2(n) & \cdots & d_L(n) \end{bmatrix}^{\mathrm{T}}. \tag{5.11}$$

When the sum of $\boldsymbol{w_i}(n)\hat{\boldsymbol{r}}_{\boldsymbol{l}}(n-i)$ is performed over all I control filter coefficients, as in Equation 5.7, the multichannel generalisation of Equation 5.7 can be expressed as

$$\boldsymbol{e}(n) = \boldsymbol{d}(n) + \hat{\boldsymbol{R}}(n)\boldsymbol{w}, \tag{5.12}$$

where the matrix of filtered reference signals corresponding to all M control sources and all L sensors can be written as

$$\hat{\boldsymbol{R}}(n) = \begin{bmatrix} \hat{\boldsymbol{r}}_1^{\mathrm{T}}(n) & \hat{\boldsymbol{r}}_1^{\mathrm{T}}(n-1) & \cdots & \hat{\boldsymbol{r}}_1^{\mathrm{T}}(n-I+1) \\ \hat{\boldsymbol{r}}_2^{\mathrm{T}}(n) & \hat{\boldsymbol{r}}_2^{\mathrm{T}}(n-1) & \cdots & \hat{\boldsymbol{r}}_2^{\mathrm{T}}(n-I+1) \\ \vdots & & & \\ \hat{\boldsymbol{r}}_L^{\mathrm{T}}(n) & \hat{\boldsymbol{r}}_L^{\mathrm{T}}(n-1) & \cdots & \hat{\boldsymbol{r}}_L^{\mathrm{T}}(n-I+1) \end{bmatrix} \tag{5.13}$$

and the vector of I control filter coefficients can be written as

$$\boldsymbol{w} = \begin{bmatrix} \boldsymbol{w}_0^{\mathrm{T}} & \boldsymbol{w}_1^{\mathrm{T}} & \cdots & \boldsymbol{w}_{I-1}^{\mathrm{T}} \end{bmatrix}^{\mathrm{T}}. \tag{5.14}$$

The objective of this control strategy, as noted above, is to minimise the sum of the squared error signals. In this case, an expression can be formed using Equation 5.12 for the cost function defined as the expectation, E, of the sum of the squared error signals, which can be weighted with a positive control effort coefficient-weighting parameter and can be expressed as,

$$J = \mathrm{E}\left[\boldsymbol{e}^{\mathrm{T}}(n)\boldsymbol{e}(n)\right] + \beta \boldsymbol{w}^{T}\boldsymbol{w}. \tag{5.15}$$

The inclusion of the β term in the cost function has a number of practical benefits, which include constraining the control effort and improving the robustness of the control system as discussed in Section 3.4.7 of [81], but it has been included here to specifically enable a constraint to be imposed on the peak-to-peak magnitude of the control signals to avoid overdriving the piezoelectric patch actuators, as discussed in Chapter 3. Substituting Equation 5.12 into Equation 5.15 gives the full cost function as

$$J = \boldsymbol{w}^{\mathrm{T}}\mathrm{E}\left[\hat{\boldsymbol{R}}^{\mathrm{T}}(n)\hat{\boldsymbol{R}}(n)\right]\boldsymbol{w} + 2\boldsymbol{w}^{\mathrm{T}}\mathrm{E}\left[\hat{\boldsymbol{R}}^{\mathrm{T}}(n)\boldsymbol{d}(n)\right] + \mathrm{E}\left[\boldsymbol{d}^{\mathrm{T}}(n)\boldsymbol{d}(n)\right] + \beta \boldsymbol{w}^{T}\boldsymbol{w}. \tag{5.16}$$

Partially differentiating this cost function with respect to $\boldsymbol{w}$ and setting each element to 0 allows the optimum set of control filter coefficients that minimise this cost function to be calculated as

$$\boldsymbol{w}_{\mathrm{opt}} = -\left\{\mathrm{E}\left[\hat{\boldsymbol{R}}^{\mathrm{T}}(n)\hat{\boldsymbol{R}}(n)\right] + \beta \mathbf{I}\right\}^{-1}\mathrm{E}\left[\hat{\boldsymbol{R}}^{\mathrm{T}}(n)\boldsymbol{d}(n)\right]. \tag{5.17}$$

5.3 Experimental Results

This section presents an implementation of the experimental setup and control strategy that have been outlined in the previous sections of this chapter. Initially, the responses of the experimental system are presented and a plant modelling study has been carried out to determine the FIR filter lengths required to accurately model the plant response of each plate, as previously conducted for the beam structure in Chapter 3. An investigation into how the broadband average level of structural vibration attenuation varies

with the control filter length is then presented. Finally, the performance of the feedforward controller is assessed for the different AABH and constant thickness active plate configurations, and the results are presented in terms of both structural response and control effort.

5.3.1 Structural Responses

Using the setup described in Section 5.1, the shaker has been driven with broadband white noise at a sampling frequency of 22 kHz. The primary response has been measured at each accelerometer for 30 seconds and the H1-estimator has been used to calculate the response between the signal driving the primary shaker and each accelerometer. In addition, the power spectral density (PSD) of the signal measured at each accelerometer has been calculated using the Welch method. The global structural response of the plate has then been estimated by summing the PSDs corresponding to each accelerometer signal and these results can be seen in Figure 5.6 for both the constant thickness plate and the plate with embedded ABHs without damping, with Henley's yellow compound, with piezoelectric patches and with both Henley's and piezoelectric patches. In addition, the broadband average vibration level for each plate configuration is shown in Table 5.2. From the primary responses presented in Figure

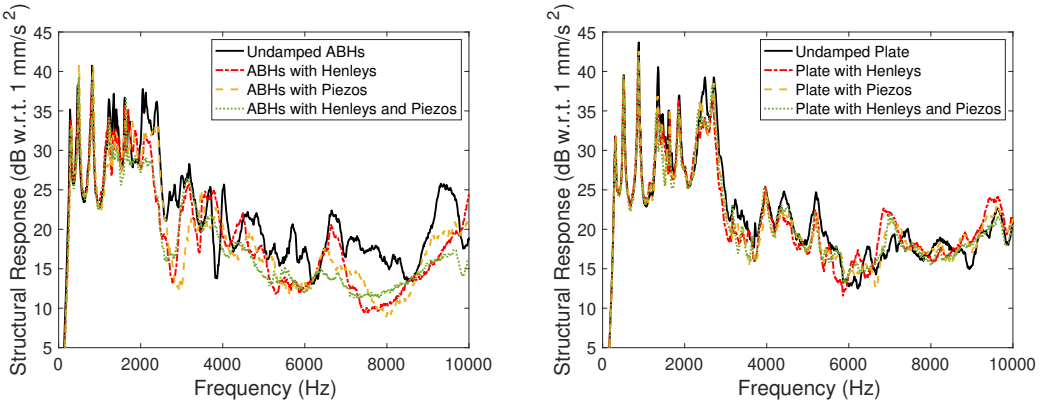

(a) Plate with ABHs

(b) Constant Thickness Plate

FIGURE 5.6: The structural responses of the plate with ABHs and the constant thickness plate with each type of damping applied.

5.6, it can be seen that all combinations of damping reduce the vibration level of the plate with ABHs. All combinations of damping also reduce the vibration level of the plate without ABHs, however the reduction is less significant. Figure 5.6(a) shows that the addition of Henley's damping material to the ABHs dampens the resonances above 1.4 kHz, which is consistent with the cut-on frequency estimated in Section 5.1 and Table 5.2 shows that this brings the broadband average vibration level down by 2 dB. Below 1.4 kHz, the addition of Henley's does not have much effect on the structural

TABLE 5.2: The broadband level of vibration for each plate configuration with respect to 1 mm/s^2

Plate type	Damping type	Broadband level
Plate with ABHs	No Damping	27 dB
	Henley's	25 dB
	Piezoelectric patches	25 dB
	Henley's and piezoelectric patches	24 dB
Constant Thickness Plate	No Damping	28 dB
	Henley's	26 dB
	Piezoelectric patches	27 dB
	Henley's and piezoelectric patches	26 dB

response. It can be seen that at some frequencies, such as around 4.5 kHz, there is a slight shift in the frequency response of the ABH plate treated with Henley's, which is likely due to the mass and stiffness that the Henley's compound adds to the structure.

Figure 5.6(b) shows that when the same amount and distribution of Henley's compound is added to the constant thickness plate, the damping effect is significantly smaller, although the frequency range affected is approximately the same as for the ABH plate (1.4 kHz to 10 kHz). Figures 5.6(a) and 5.6(b) show that if Henley's damping material is replaced with piezoelectric patches, which are effectively 13 grams lighter per patch and cover a slightly smaller surface area compared to the Henley's damping treatment, the level of damping is approximately the same for the ABH plate. This is because the majority of the damping in an ABH occurs within the thinnest region of the tip, which is covered by the Henley's compound or piezoelectric patch. However, for the constant thickness plate the level of damping provided by the piezoelectric patches is lower compared to Henley's damping material.

From Table 5.2, it can be seen that the combination of both Henley's compound and the un-driven piezoelectric patches dampens the ABH plate by 1 dB more than either individual treatment. The specific frequency bands where there is a difference in the level can be seen in Figure 5.6(a); for example, the peak at 2.1 kHz which is partially dampened by the addition of either treatment but fully dampened by the combination of both treatments. In contrast, the constant thickness plate does not benefit from the combination of Henley's compound and piezo patches. By examining the broadband levels shown in Table 5.2, it can be seen that the combination of both treatments gives the same broadband average level as the Henley's treatment. In addition to the differences introduced by ABHs and different configurations of damping, there is a similar drop in the structural response of both plates between 2 kHz and 3 kHz. This drop occurs around the critical frequency of each plate, which can be estimated as the frequency at which the flexural wavelength matches the acoustic wavelength [2]. At and above the critical frequency, the radiation efficiency of the plate significantly increases.

Since both plates are manufactured from the same material and share the same thickness profile, with the exception of the ABHs, they will approximately share the same critical frequency, which has been calculated as 2.2kHz.

These passive structural results have shown that, in the case of the ABH plate, an active solution should focus on the 0 Hz to 2 kHz frequency band, where the passive damping of the ABHs is less effective. In contrast, an active solution for the constant thickness plate would be required over the full frequency range presented, or a larger quantity of passive damping treatment would be initially required to match the passive performance of the ABH embedded plate.

Using the same setup, each of the 5 piezoelectric patches has been driven separately with white noise using a sampling frequency on 22 kHz. Again, 30 second measurements have been made at each accelerometer and the H1-estimator has been used to calculate the plant responses between the input to each piezoelectric patch and each accelerometer. Two examples are given in Figure 5.7; the first is the plant response between the input to piezoelectric patch 1 and accelerometer 1 (see Figure 5.3) and the second is the plant response between the input to piezoelectric patch 2 and accelerometer 1. Accelerometer 1 has been chosen because it is located near the corner of the clamped plate and will thus detect a greater number of structural modes than, say, the centrally located accelerometer; piezoelectric patch 1 is located at the centre of the plate, whilst piezoelectric patch 2 is located towards one corner of the plate, thus providing an overview of the different plant response characteristics. From the results shown in Figure 5.7, it can be seen that the plant responses for each plate configuration are relatively similar at frequencies below 1 kHz, which is expected because the cut-on frequency of the ABHs has been shown to be at approximately 1.4 kHz by the results presented in Figure 5.6(a). Figures 5.7(a) and 5.7(c) show that the centrally located piezoelectric patch (m = 1) effectively excites the plate at frequencies above 250 Hz, which corresponds to the cut-on frequency of the piezoelectric patches. These results are not surprising since the central actuator will couple into the first mode of the plate well. However, it can be seen from Figures 5.7(b) and 5.7(d) that piezoelectric patch l = 2, which is located nearer the edge of the clamped plate, is less effective at exciting the lower frequencies and this is reflected in the noisy phase and low magnitude of the signal below 650 Hz. This may cause issues when trying to control the first two structural resonances of the plate shown in Figure 5.6, which occur below 650 Hz. Between 1 kHz and 2 kHz, the response of the plate configurations with ABHs is up to 20 dB higher than the constant thickness plate configurations, which indicates that the ABH plate configuration, both with or without the Henley's compound applied, is more receptive to energy input from the piezoelectric patches. Thus, based on both the structural responses due to the primary excitation, shown in Figure 5.6, and the secondary plant responses, the ABH embedded plate offers both higher passive damping

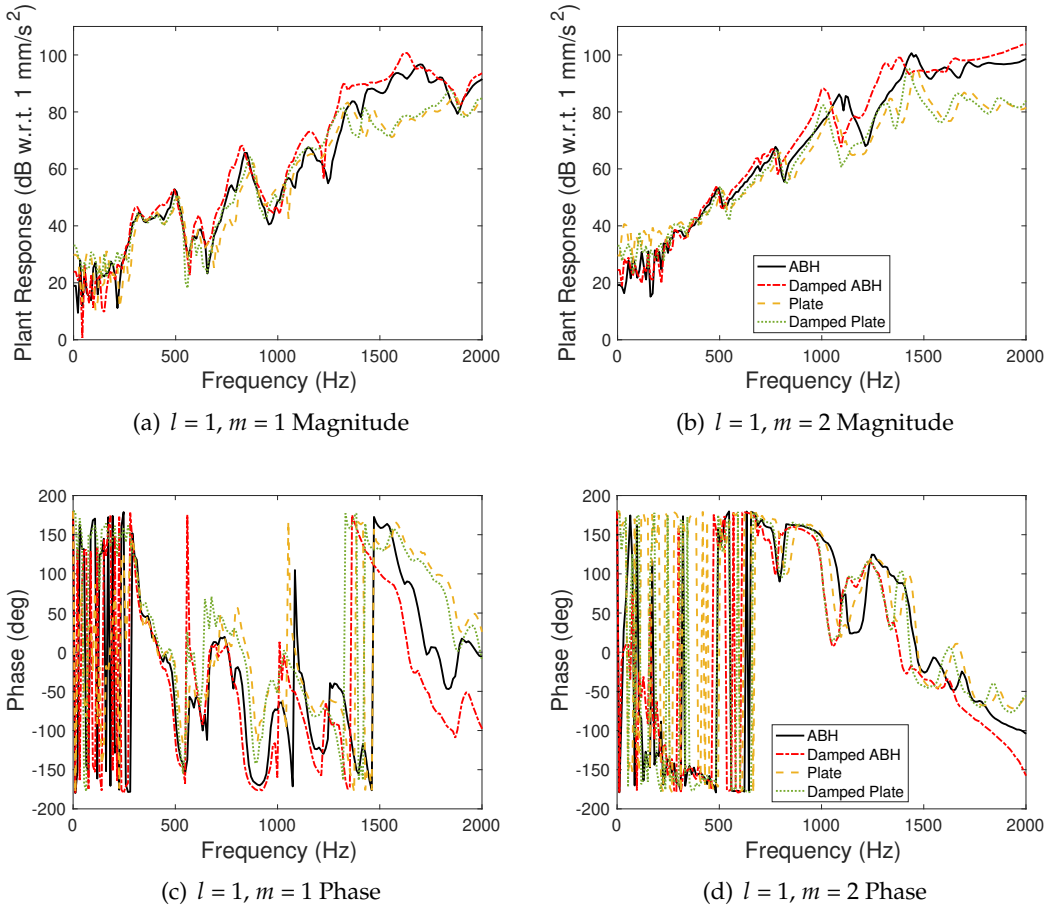

(a) $l = 1$, $m = 1$ Magnitude

(b) $l = 1$, $m = 2$ Magnitude

(c) $l = 1$, $m = 1$ Phase

(d) $l = 1$, $m = 2$ Phase

FIGURE 5.7: The plant response between the input to piezoelectric patch $m = 1$ and accelerometer $l = 1$ and also the input to piezoelectric patch $m = 2$ and accelerometer $l = 1$ for each of the plate configurations.

at higher frequencies and greater coupling between the piezoelectric patch actuators and the structural response when compared to the constant thickness plate.

5.3.2 Plant Modelling

In this section, a plant modelling study, similar to the one presented for the active beam in Chapter 3, has been carried out to determine the different plant modelling filter requirements for the plates with and without ABHs. In this study and the following control implementation a sampling frequency of 4 kHz has been used, which is justified based on the results presented in Section 5.3.1 because the passive damping of the ABHs is poor below 2 kHz and thus requires the use of active control. From this point the term broadband will refer to the full 0 – 10 kHz frequency range, whilst the 400 Hz – 2 kHz frequency band will be referred to the control bandwidth for clarity. This frequency range has been chosen because it captures the resonances that fall above the

cut-on frequency of the piezoelectric patches, but is below the frequency at which the passive damping becomes effective.

For each plate setup with piezoelectric patches, the plant frequency responses have been modelled as FIR filters using the MATLAB function `invfreqz`, which fits a discrete time filter to a frequency response. In order to examine the effect of plant model accuracy, FIR filters have been calculated with between 2 and 150 coefficients (corresponding to durations of 0.5 ms to 37.5 ms at the 4 kHz sample rate). The frequency responses that have been estimated using the H1-estimator have been used as the ideal plant responses and these have been compared to each of the plant models using the normalised mean-squared error (NMSE), which has been calculated as an average over frequency and both the control actuators and error sensors, which gives

$$NMSE = \frac{1}{ML} \sum_{\omega=0}^{\omega_{max}} \sum_{m=1}^{M} \sum_{l=1}^{L} \frac{|g_{ml}(\omega) - \widehat{g}_{ml}(\omega)|^2}{|g_{ml}(\omega)|^2}, \tag{5.18}$$

where $\widehat{g}_{ml}$ is the frequency response of the FIR filter modelling the plant response between the m-th actuator and l-th sensor, g_{ml} is the corresponding identified plant frequency response and there are M piezoelectric patches and L accelerometers. The NMSE has been calculated for each of the 4 different plate configurations with piezoelectric patches attached (with and without Henley's) and the results from this study are presented in Figure 5.8. From these results, it can be seen that as the number of FIR

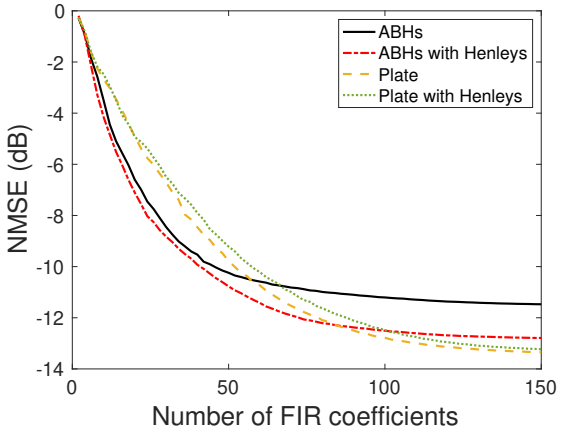

FIGURE 5.8: The normalised mean-squared error (NMSE) for the plant responses between the piezo patches and the accelerometer array.

coefficients increases, the error in the plant model decreases for all cases, as expected. It can also be seen that for the plate with undamped ABHs, the NMSE is lower than for the constant thickness plate configurations for filter lengths of between 0 and 60 coefficients. For filter lengths greater than 60 coefficients, the change in the error plateaus and increasing the length of the plant model further does not give any significant improvement in the plant modelling accuracy. The plate with ABHs and Henley's compound

has a lower NMSE than all of the other configurations up to 80 filter coefficients, above which the error plateaus and becomes comparable to either of the constant thickness plate configurations. Additionally, the plateau of the error in these three configurations is approximately 2 dB lower than the plate with undamped ABHs. The configurations with ABHs have both plate modes and local ABH modes, which increases the complexity of the plant responses and may contribute to the higher NMSE plateau, particularly when there is no added damping to suppress the local ABH modes. In all cases, the plant model accuracy is not improved significantly by increasing the filter length beyond 128 coefficients and so this filter length will be used in the control performance evaluation. Comparing this plant modelling study to the plant modelling study conducted for the beams, which was presented in Chapter 3, it can be seen that the modelling error for the plates has plateaued at a lower number of FIR filter coefficient, approximately 200 less than for the beams. This may be attributed to the high level of damping added by clamping the plates to the box, which results in a similarly damped response at frequencies below 2 kHz. Comparatively, the beams are cantilevered and so less damping has been introduced into the system via its boundary conditions. In this case, the passive damping of the ABH beam termination was clearly higher than the passive damping of the constant thickness beam termination.

5.3.3 Control Filter Length Study

Having established the plant modelling requirements for each plate configuration as 128 FIR filter coefficients, the effect of the control filter length can now be investigated. To determine how many coefficients are required for the optimum controller, $\boldsymbol{w}_{\text{opt}}$, the attenuation in the structural response at each frequency has been calculated for a range of control filter lengths as

$$\text{Attenuation}(\omega) = \frac{trace(\boldsymbol{S_{dd}}(\omega))}{trace(\boldsymbol{S_{ee}}(\omega))}, \tag{5.19}$$

where $\boldsymbol{S_{dd}}$ is the matrix of cross and power spectral densities of the disturbance signals and $\boldsymbol{S_{ee}}$ is the matrix of cross and power spectral densities of the error signals, each at the frequency ω. An average over the frequencies examined has then been taken to obtain the mean control bandwidth attenuation for a particular control filter length. The optimal control performance has been calculated using the formulation presented in Section 5.2. These calculations have been performed using a range of between 2 to 80 FIR filter coefficients and in each case the peak-to-peak voltage of the control signal has been constrained to be within the operating limits of the piezoelectric patch actuator using the β weighting parameter shown in Equation 5.17. The mean control bandwidth attenuation with respect to the uncontrolled constant thickness plate has been plotted against the number of control filter coefficients used and the results are shown in Figure 5.9. From these results, it can be seen that the two constant thickness

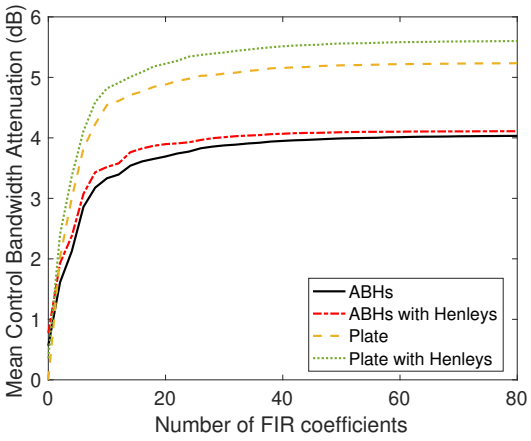

FIGURE 5.9: The mean attenuation over the control bandwidth achieved with respect to the uncontrolled constant thickness plate, using a control filter with between 2 and 80 FIR coefficients.

plate configurations reach a slightly higher level of attenuation than either of the ABH plate configurations. However, this is at most 1.5 dB and may be due to the higher level of passive damping present in the ABH plate configurations. It can also be seen that in all cases, the mean control bandwidth attenuation increases most between 0 and 10 control filter coefficients, above which the attenuation plateaus. Increasing the control filter beyond 32 FIR coefficients gives less than 0.2 dB performance benefits and so this filter length will be used in the performance evaluation.

5.3.4 Control Performance

The control strategy described in Section 5.2 has been implemented offline to determine the performance of each of the plates under ideal conditions using filtered white noise between 400 Hz and 2 kHz. This frequency range has been justified in Section 5.3.2. The plant model filters for each case have been implemented with 128 FIR coefficients based on the study presented in Section 5.3.2 and the control filters have been set to contain 32 FIR coefficients based on the study presented in Section 5.3.3. The maximum peak-to-peak voltage of the control signals has been limited to just within the operating range of the piezoelectric patches for all cases by the use of the β weighting parameter in Equation 5.17 to provide a direct and realistically achievable comparison of the performance. The results are presented in terms of the control performance and associated control effort and can be seen in Figures 5.10 and 5.11 respectively. The control bandwidth level, between 400 Hz and 2 kHz, before and after each control strategy is implemented is shown in Table 5.3; it should be noted that these levels differ from those presented in Table 5.2, which show the broadband (0 – 10 kHz) levels before control and include the passive performance of the different treatments. From the results presented in Figure 5.10, it can be seen that effective structural control can be achieved

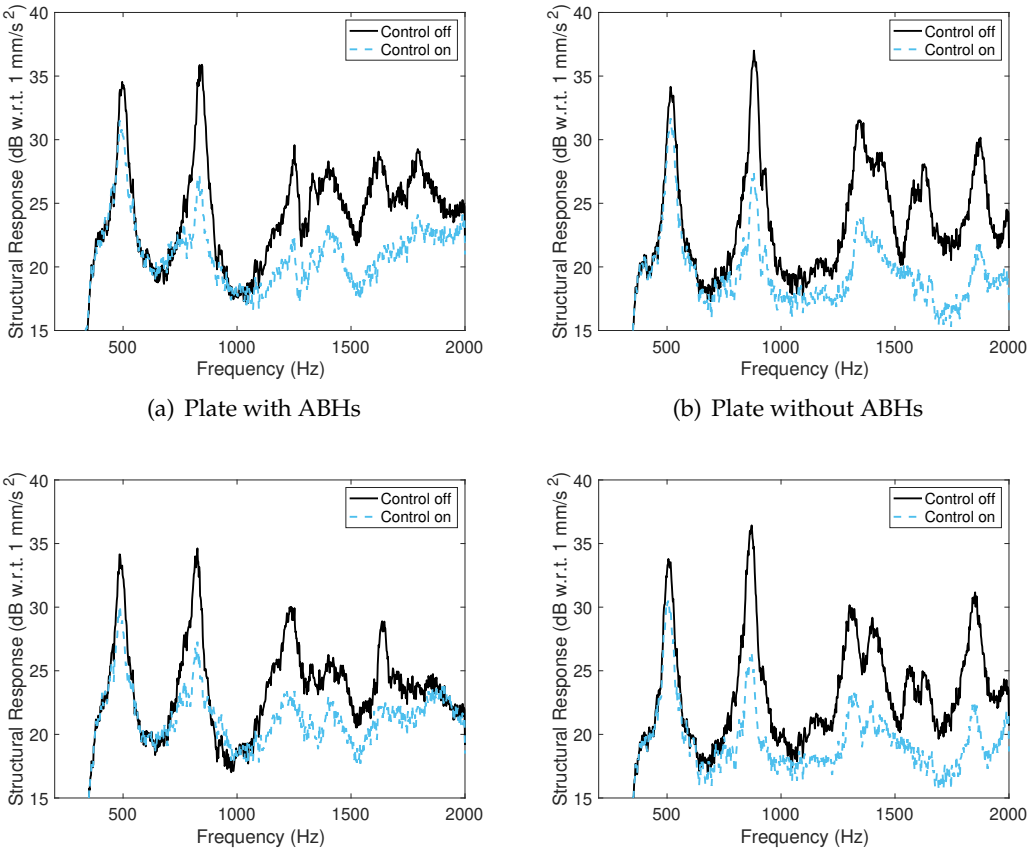

(a) Plate with ABHs

(b) Plate without ABHs

(c) Plate with ABHs and Henley's

(d) Plate without ABHs and with Henleys

FIGURE 5.10: The global structural response with respect to 1 mm/s^2 after minimising the structural response for (a) the plate with ABHs, (b) the plate with no ABHs, (c) the plate with ABHs and Henley's and (d) the plate with no ABHs and Henley's.

for all plate configurations. When structural control is performed on the plate with embedded ABHs (Figure 5.10(a)), it can be seen that the resonance at 500 Hz is reduced by approximately 4 dB, the resonance at 840 Hz is reduced by approximately 10 dB and the smaller resonances above 1 kHz have been reduced by approximately 5 dB. It can also be seen from the results presented in Table 5.3 that the active control strategy reduces the average structural control bandwidth level of the ABH plate by 4 dB. From the control effort results presented in Figure 5.11, it can be seen that the ABH plate configuration without Henley's requires up to 3 dB more energy to control the 500 Hz mode compared to any of the other configurations, but less energy than the constant thickness plate configurations to achieve control at higher frequencies. The mean control effort required for this configuration is -4 dB. When structural control is performed on the plate with ABHs that also have Henley's compound applied, it can be seen from the results presented in Table 5.3 that the control bandwidth level after control is the same as for the configuration without Henley's, and that the controller has reduced the control bandwidth level by 3 dB to achieve this performance. Once

TABLE 5.3: The mean control bandwidth (400 Hz – 2 kHz) level of the structural vibration of each plate with piezoelectric patches attached, with and without active control.

Plate type	Control off 400 Hz – 2 kHz	Control on 400 Hz – 2 kHz
ABHs	26 dB	22 dB
ABHs with Henley's	25 dB	22 dB
Constant thickness	26 dB	21 dB
Constant thickness with Henley's	26 dB	21 dB

again, this reduction is attributed to the active control strategy and does not take into account the passive damping of the ABHs above 2 kHz, which has been shown in Section 5.3.1. The results in Figure 5.10(c) show that the resonances at 480 Hz and 830 Hz are reduced by 5 dB and 8 dB respectively. The resonances above 1 kHz are reduced by up to 5 dB. Figure 5.11 shows that the control effort required to control the 480 Hz mode is approximately the same as for both constant thickness plate configurations and at all frequencies above 500 Hz, the ABH plate configuration with Henley's treatment requires the least control effort, which is reflected by a mean control effort level of -9 dB. This demonstrates that applying a viscoelastic damping material to the structure can give an additional performance benefit that is not necessarily apparent from the structural response results. The results presented in Figure 5.10(b) show that when structural control is performed on the constant thickness plate without Henley's, the resonance at 515 Hz is reduced by 3 dB and the resonance at 880 Hz is reduced by 3 dB. The resonances above 1 kHz are reduced by up to 8 dB and the average control bandwidth level shown in Table 5.3 is reduced by approximately 5 dB. The required control effort for this implementation is shown to be similar to the ABH plate configurations below 800 Hz but significantly larger at higher frequencies. The mean control effort in this case is 0 dB, which is considerably higher than either of the ABH plate configurations. When structural control is performed on the constant thickness plate with Henley's damping, the results presented in Figure 5.10(d) show that the resonance at 505 Hz is reduced by 4 dB, the resonance at 870 Hz is reduced by 10 dB and the resonances above 1 kHz are reduced by up to 8 dB. The average control bandwidth level, which is shown in Table 5.3, is reduced by approximately 5 dB, which is less than the constant thickness plate without Henley's treatment, however, the controlled level is the same. It should be noted that this additional damping treatment also had minimal affect on the structural response at higher frequencies, which has been shown in Section 5.3.1. The control effort shown in Figure 5.11 is very similar to the constant thickness plate without Henley's and this is reflected in the mean control effort, which is also 0 dB. These results have shown that there is very little difference between the two constant thickness plate configurations, both of which require more control effort than the ABH plate configurations, but achieve a comparable post control vibration level. This is consistent with the observations regarding the passive attenuation provided by the

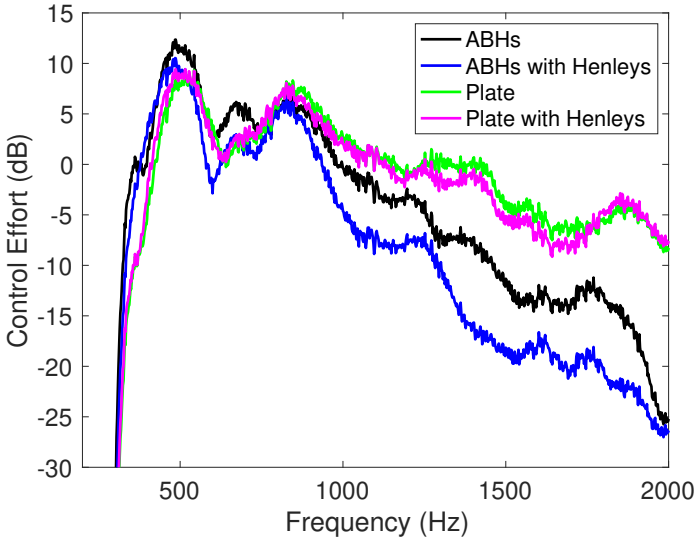

FIGURE 5.11: The control effort required for each control case.

TABLE 5.4: The mean broadband level of the structural vibration of each plate with no damping applied (undamped, control off), with piezoelectric patches and Henley's treatment applied (damped, control off) and with piezoelectric patches, Henley's treatment and active control (damped, control on).

Plate type	**Undamped Control off 0 – 10 kHz**	**Damped Control off 0 – 10 kHz**	**Damped Control on 0 – 10 kHz**
ABHs	27 dB	24 dB	22 dB
Constant thickness	28 dB	26 dB	25 dB

Henley's compound as presented in Section 5.3.1, which demonstrated that the passive damping on the constant thickness plate is not particularly effective. When Henley's is added to the ABH plate, however, there is a significant reduction in the energy required for control, especially towards the upper end of the presented control bandwidth. This is consistent with the increased passive performance shown in Section 5.3.1 and shows that the additional damping has benefits in both the passive and also active performance. Interestingly, considering that the plant modelling error for the AABH plate configuration without Henley's has been shown in Section 5.3.2 to be approximately 2 dB higher than the other configurations, there is no indication that this has significantly affected the optimal performance results.

To give an indication of the wider bandwidth performance of each plate, Figure 5.12 presents the structural responses when the hybrid of the passive and active control strategies are used. From these results it can clearly be seen that the AABHs provide an effective hybrid control solution and considerably dampen the structure over the full bandwidth presented, whereas the constant thickness plate is only damped over the bandwidth that active control is applied. Table 5.4 shows that the mean broadband

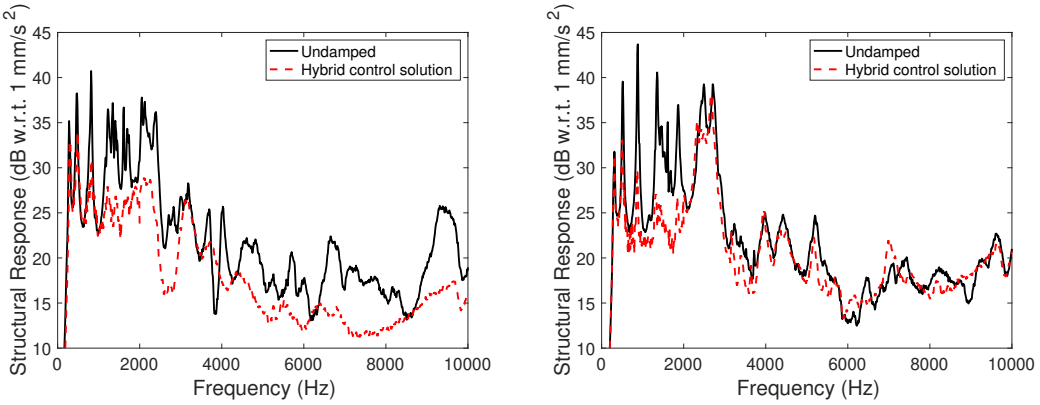

(a) Plate with ABHs (b) Constant thickness plate

FIGURE 5.12: The global structural response with respect to 1 mm/s^2 over the extended bandwidth when a combination of active and passive control is used.

vibration level is reduced from 27 dB to 22 dB in the ABH plate and from 28 dB to 25 dB in the constant thickness plate. These results demonstrate that the plate with AABHs achieves a 3 dB performance benefit over the constant thickness active plate and a 6 dB performance benefit over the uncontrolled and undamped constant thickness plate. Taking into account the reduced control effort of the AABHs, these results have clearly highlighted the performance benefits gained from embedding AABHs into a plate.

5.4 Summary

Previously, in Chapters 3 and 4, it has been shown that active control can be used to reduce the reflection coefficient or vibration of an ABH termination. This chapter has presented an investigation into the active control of a plate with embedded ABHs and compared it to the active control of a constant thickness plate. To realise the AABHs, circular piezoelectric patches have been attached to the flat side of each ABH and Henley's damping compound has been applied to the curved side of each ABH. The same treatment has also been applied to the constant thickness plate in the same distribution. Before control is performed, it has been shown that the mass of the plate with AABHs is lower than the mass of the constant thickness active plate. In addition, the passive damping provided by the AABHs has been shown to significantly attenuate the higher frequency resonances of the plate.

To address the limited passive performance at lower frequencies, a feedforward multichannel control strategy has been considered over a control bandwidth of 400 Hz – 2 kHz where the piezoelectric patches are driven to minimise the global structural response of the plate. Prior to investigating the active control performance, a study

has been carried out to examine the requirements of the FIR filter in order to accurately model the plant responses. The results have shown that the error between the plant model and the measured plant response plateaus at a similar level for both of the constant thickness plate configurations and the AABH plate configuration with damping. The error associated with the plant model for AABH plate configuration without damping plateaus 2 dB higher. However, prior to the plateau the plant model for both AABH plate configurations is more accurate. A control filter length study has subsequently been performed and the results showed that the number of control filter coefficients required to achieve optimal control is approximately the same for all plate configurations.

When active control is performed on each of the plates, it has been shown that the structural response can be reduced at the resonant frequencies by up to 10 dB. Interestingly, the lower plant model accuracy of the AABH plate configuration without Henley's did not translate into any notable difference in control performance. The average level of attenuation achieved over the controlled bandwidth has been shown to be within 1 dB for each of the plate configurations, therefore demonstrating that there is no particularly advantageous configuration in terms of attenuation. However, the control effort required by each of the AABH plate configurations, particularly the design with damping material added, has been shown to be significantly lower than the control effort required by either of the constant thickness active plate configurations. When the performance is assessed over the full 0 – 10 kHz bandwidth, it has been shown that the hybrid of active and passive damping provided by the AABHs reduces the structural response of the plate by 3 dB more than simply performing active control on a constant thickness plate. Therefore, the work in this chapter has been shown that integrating active control into an embedded ABH suitably addresses the low frequency limitation imposed by the size of the ABH. In addition, it has been shown that a plate with embedded AABHs is lighter than a standard plate with active components and offers a performance advantage in terms of both broadband damping and control effort. This chapter has shown that, similarly to the beam cases presented in Chapters 3 and 4, the addition of AABHs to a structure can give performance advantages in a wide variety of ways which will be summarised in the following and final chapter of this thesis.

Chapter 6

Conclusions and Future Work

6.1 Conclusions

Structural vibrations, specifically flexural vibrations, can cause damage to structures and can cause the radiation of undesired noise. This thesis has focussed on the design of a lightweight damping solution for structural vibrations called an ABH and has examined how active control can be integrated into an ABH in order to improve the broadband performance.

Previous work has shown for a small number of discrete ABH geometries that the reflection coefficient of a beam based ABH termination can be reduced by extending the length of the taper, reducing the tip height and increasing the power law. It has also previously been shown that the bands of low reflection of an ABH termination are linked to the local modes of the taper, which are dependent on the design parameters. The dimensions of the investigated configurations, specifically the tip height, have not always been practical and so the work presented in Chapter 2 of this thesis has first addressed some of the limitations of previous studies and provided a fine resolution parametric study and modal analysis of an ABH termination over a practical design parameter range. It has been shown in detail how modifying each of the geometrical parameters of an ABH termination influences the reflection coefficient and it has been highlighted that as each parameter is varied, the local minima within the bands of low reflection vary in magnitude as well as frequency. The local taper modes of the ABH have been shown to align with the bands of low reflection, which is consistent with previous investigations but has, in this case, been shown over a wider range of parameters and frequencies. Therefore, for a tonal problem, the parameters can be tuned so that the most absorbing mode occurs at the problematic frequency. Finally, it has been shown that when two parameters are varied simultaneously, the power law and tip height can be optimised for a particular design, whilst the taper length should just be made longer to improve performance. From this finding, it has been demonstrated that, although

reducing the tip height and increasing the power law of the ABH increases the modal density of the ABH, it will also increase the reflection from the ABH junction and will, therefore, not necessarily result in the maximum performance. The parametric study has been used to design an ABH with practical dimensions, which has then been tested experimentally to validate the model.

The work presented in Chapter 3 has taken the practically designed ABH beam termination and introduced active components to the taper. The objective of this novel combination is to create a hybrid damping solution, where the passive damping of the ABH is combined with active control, resulting in a performance increase that is greater than the simple summation of the active or passive treatments operating in isolation. To realise the AABH, a piezoelectric patch actuator has been attached to the ABH taper to act as both the passive damping strip and also as the secondary source and a feedforward wave-based control strategy has been used to control the reflected wave component, which is estimated using two error sensors on the beam. The performance of the AABH termination has been compared to a beam with a constant thickness active termination. This investigation has demonstrated that, due to the passive damping of the ABH, the AABH termination requires significantly fewer FIR coefficients to achieve the same plant model accuracy as the constant thickness termination. In addition, it has been found that to achieve a specific level of broadband attenuation, the AABH termination requires significantly fewer control filter coefficients compared to the constant thickness termination. This means that the AABH is more computationally efficient to implement than the constant thickness active beam termination. It has also been shown that the constant thickness termination requires a significantly higher control effort than the AABH termination and when the peak-to-peak control voltages for the two configurations are constrained to match, the AABH significantly outperforms the constant thickness active termination. In fact, the AABH termination offers a performance advantage above that expected from simply combining the levels of control offered by the constant thickness active termination and the passive ABH effect. In addition to the performance results, it has also been noted that controlling the reflection coefficient using the AABH termination caused an enhancement in the tip vibration, which has been linked to the energy focussing effect of the ABH and may cause accelerated structural fatigue when implementing an AABH in practice. These results have then been validated experimentally.

The work presented in Chapter 4 has taken the beam with an AABH termination and has investigated the use of a remote damping feedback control strategy. This study demonstrates the potential for a feedback control implementation, but provides further insight into the link between controlling the reflection coefficient and enhancing the vibration of the tip of the ABH. In this case, an accelerometer has been added to the underside of the taper to provide a measurement of the local vibration in the AABH. The signal from this accelerometer has been used to drive the piezoelectric patch using

a local feedback loop with an added compensator. Through a geometrical controller design method, it has been shown that a compensator can be selected that can provide a tradeoff between reducing the reflected wave component and reducing the local taper vibration. Simultaneous minimisation of both the reflected wave component and the taper vibration could not be achieved at any frequency examined for the AABH termination. However, it has been shown that it is possible at a small number of frequencies to significantly reduce both the reflected wave component and the taper vibration simultaneously. Four specific compensator cases have then been investigated to demonstrate some possible control strategies and provide further insight into the control tradeoff. It has been shown that at most frequencies, the performance benefits achieved by minimising the reflected wave component are not possible without significantly enhancing the taper vibration. It has also been shown that minimising the taper vibration enhances the reflected wave component, particularly at lower frequencies. Although it is not possible to minimise either error signal without enhancing the other, it is possible to achieve a moderate reduction in each error signal without enhancing the other. This approach can, therefore, be used to potentially extend the life of an AABH whilst maintaining the passive performance.

The work presented in Chapter 5 extends the concept of an AABH to a plate and considers a configuration with five ABHs embedded in a plate. The plate has been mounted on a box and configured with no damping, with viscoelastic damping material applied to the curved side of the ABHs, with circular piezoelectric patches attached to the flat side of the ABHs and with both the viscoelastic damping material and piezoelectric patches attached. The first advantage that has been demonstrated prior to any control is that the mass of the plate with embedded ABHs is lower than the mass of a plate with identical dimensions but without ABHs, regardless of the treatment applied. It has also been shown that the passive performance of the plates is similar up to 2 kHz, above which the ABH plate is more damped. To improve the performance below 2 kHz, a global multichannel feedforward control strategy has been implemented. Over this control bandwidth, it has been shown that the plate with embedded AABHs and the constant thickness active plate have similar requirements in terms of plant modelling and control filter length. The strong similarity between the two plates has been attributed to clamping each plate, which provides a higher level of damping than for the beam considered in Chapters 3 and 4. The damping from the ABHs is, therefore, small below 2 kHz compared to the damping from clamping the plate. Control has then been implemented for each plate configuration and it has been shown that the global response could be significantly reduced in each case. The difference in the structural response between each plate configuration has been shown to be less than 1 dB averaged over the control bandwidth, however, the control effort required by the AABH plate has been shown to be significantly lower, especially when viscoelastic damping material has also been applied to the ABHs. In addition, when the performance is

assessed up to 10 kHz, taking into account the passive damping, the AABH plate significantly outperforms the constant thickness plate. The constant thickness plate performed poorly above the active bandwidth. To match the performance of the AABH plate, either significantly more damping material would be required, adding significant mass to the structure, or a more complex active control system would be required to extend the control bandwidth, however, this is likely to become quickly impractical due to the increased number of sensors and actuators required.

To conclude, the work in this thesis has shown that ABHs can be designed effectively for practical applications where space and weight are limited by using the power law and tip height to tune the performance. It has also been shown that active control can be integrated into both beam based ABHs and plate based ABHs to achieve a significant performance increase over either an active solution or passive solution in isolation, and that the computational resources and electrical power required to implement control are lower when AABHs are used. Because of this, cheaper components can be used, which is beneficial for implementing AABHs in practice. In addition, all ABH and AABH control solutions have been shown to reduce the mass of the structure.

6.2 Future Work

There are a number of possible extensions of this work for the future, which have not been followed due to the time available and the direction of this thesis. The first extension could be to use the finite element model to investigate the radiated sound power from an ABH on a beam and the overall kinetic energy of the system. The radiated sound power and kinetic energy of the system could also be used to assess the design tradeoff, and may not follow the same trend as minimising the reflection coefficient. The finite element model could also be used to assess stresses on the system, so that the effect of vibration induced fatigue could be estimated. This could also lead to experimentally stress testing ABHs in industrial environments, and would be particularly useful for the transition of ABHs into industry.

A second extension to the modelling work would be to perform a similar parametric study to that presented in Chapter 2 but for a plate based ABH, which would require a different performance criteria such as surface mobility, radiated sound power or total kinetic energy within the plate. Although this would require significant computational power, this study would highlight whether the design parameters have similar tuning capabilities as for the beam based ABH. The model could, in addition, be used to investigate the optimum configuration of ABHs in a plate.

A third extension to the modelling work could be to perform a detailed modal study, exploring how the complex eigenmodes are linked to the behaviour of the ABH. This

could tie in with the work presented in [76] and could also encompass how the eigenmodes are affected by the active control strategies presented in Chapters 3 and 4. Active control could also be investigated as a means to achieve critical coupling of low order modes [76]. Similarly to the previous suggestion, this modelling work could also be extended to a plate, where the model behaviour is more complex.

With regards to AABHs, the work presented in this thesis could be extended in a number of ways. The feedforward control strategy used in Chapter 3 could be modified to control the radiated sound power. To achieve this, an estimate of the radiated sound power is required, which can be calculated using the particle velocity and sound pressure level measured at a number of discrete points that enclose the AABH and beam [96]. Simulations could then be performed offline to determine the possible performance benefits by directly controlling the estimated sound power. If this proves successful, structural sensors could be added to the AABH and beam and an active structural acoustic control (ASAC) strategy could be implemented, which would require the identification of the radiation resistance matrix [81, 97].

The control of the radiated sound power using an AABH will result in some change in the response of the taper, similarly to what has been demonstrated when controlling reflection. The remote damping geometric controller design [85] presented in Chapter 4 could be used to investigate the relationship between controlling the radiated sound power and the local vibration in the taper. Furthermore, this study could also include the reflected wave component as a third error signal, which would provide further insight into a three-way tradeoff between controlling the reflected wave component, controlling the radiated sound power and controlling the vibration of the taper. This work would then be extended to a realtime implementation using the time domain RLS controller presented in Chapter 4, which would require further work to ensure that the controller is both stable and robust.

The work presented in Chapter 5 could be extended by examining a control strategy that minimises the radiated sound power. Initially, similarly to the suggestion regarding sound power control for the beam based AABH, the radiated sound power could be estimated by measuring the particle velocity and sound pressure over an enclosing surface [96]. This sound power estimate could be directly controlled in an offline simulation and, if shown to be effective, an ASAC control strategy could be implemented [81, 97].

The work presented in Chapter 5 could also be extended by using the remote damping controller presented in Chapter 4 [85] to investigate the relationship between structural control, acoustic control and the vibration of the AABHs. This would provide insight into whether there is any performance tradeoff between the two control strategies and whether either control strategy causes significant vibration within the AABH.

Finally, different geometries, arrangements, or numbers of AABHs could be studied as, due to time limitations, only one design has been chosen to be investigated in this thesis. This could tie in with the earlier suggested modelling extensions and other ABH designs presented in the ABH literature, such as the resonant beam damper [33]. For example, this design could then be extended to create a meta-surface of attached AABHs. The damping optimisation procedures presented in [53], or focussing effect presented in [7], could also be applied to optimise the distribution of piezoelectric patches on the AABH for both passive and active performance.

These suggestions are only a few of the many possibilities that are now available with the use of the AABH vibration damping design and it will be interesting to observe developments in the fields of ABHs and active control that may present new opportunities for hybrid AABH damping solutions.

Appendix A

Equipment Lists

A.1 Chapter 2: Parametric Study Experimental Validation Setup

- Computer running MATLAB 2011a and Control desk version 3.7.
- dSpace, Double Autobox 1005, DAC: DS2103, ADC: DS2002, SN: 46310.
- Fylde, FE93PA, Power Amplifier with Low Pass Filters, SN: 115/081.
- Data Physics, IV46, Shaker, SN: CRAC202.
- Fylde, MA32/40, ICP MicroAnalogue with Low Pass Filters, SN: 214/201.
- Polytec, PDV 100, Laser Vibrometer, Version AO, SN: 0266782.

A.2 Chapter 3: Feedforward Active ABH Beam Setup

- Computer running MATLAB 2011a and Control desk version 5.4.
- dSpace, Single Autobox 1005, DAC: DS2103, ADC: DS2002, SN: 22319.
- Benchmaster, 21M Kemo, Filter Bank with ICP conditioning, SN: 107523.
- Fylde, FE93PA, Power Amplifier with Low Pass Filters, SN: 115/081.
- PCB–AV, 790-A01, High Voltage Power Amplifier, SN: 139.
- Data Physics, IV46, Shaker, SN: CRAC202.
- PCB, 352A24, ICP Shear Accelerometers, SNs: LW147291, LW147292.
- PI Ceramic, PI-876.A11, DuraAct Patch Transducers, SNs: 37/5, 37/6.

A.3 Chapter 4: Feedback Active ABH Beam Setup

- Computer running MATLAB 2011a and Control desk version 5.4.
- dSpace, Single Autobox 1005, DAC: DS2103, ADC: DS2002, SN: 22319.
- Benchmaster, 21M Kemo, Filter Bank with ICP conditioning, SN: 107523.
- Fylde, FE93PA, Power Amplifier with Low Pass Filters, SN: 115/081.
- PCB–AV, 790-A01, High Voltage Power Amplifier, SN: 139.
- Data Physics, IV46, Shaker, SN: CRAC202.
- PCB, 352A24, ICP Shear Accelerometers, SNs: LW147291, LW147292, LW147556.
- PI Ceramic, PI-876.A11, DuraAct Patch Transducers, SNs: 37/5, 37/6.

A.4 Chapter 5: Feedforward Active ABH Plate Setup

- Computer running MATLAB 2011a and Control desk version 5.4.
- dSpace, Single Autobox 1005, DAC: DS2103, ADC: DS2002, SN: 22319.
- Benchmaster, 21M Kemo, Filter Bank with ICP conditioning, SN: 107523.
- Benchmaster, 21M Kemo, Filter Bank with ICP conditioning, SN: 107524.
- Data Physics, PA30E, Power Amplifier, SN: 09/A6Q/24985.
- Ling Dynamic Systems, V457, Shaker, SN: 338.
- PCB–AV, 790-A01, High Voltage Power Amplifier, SN: 139.
- PCB, 352A24, ICP Shear Accelerometers, SNs: LW147557, LW147287, LW147556, LW147291, LW147399, LW147400, LW147289, LW147549, LW147286, LW145761, LW147553, LW147292.
- PI Ceramic, PI-876.K004, DuraAct Patch Transducers, SNs: 4106, 4107, 4108, 4109, 33.

References

[1] C.R. Fuller, S.J. Elliott and P.A. Nelson, "Active Control of Vibration," *Academic Press*, London, 1996.

[2] F. Fahy and D. Thompson, "Fundamentals of Sound and Vibration," 2nd edition, *CRC Press*, Boca Raton, 2015.

[3] M. Mironov, "Propagation of a flexural wave in a plate whose thickness decreases smoothly to zero in a finite interval," *Soviet Physics: Acoustics*, vol. 34, no. 3, pp. 318–319, 1988.

[4] V.V. Krylov and F. Tilman, "Acoustic 'black holes' for flexural waves as effective vibration dampers," *Journal of Sound and Vibration*, vol. 274, pp. 605–619, 2004.

[5] L. Zhao, S.C. Conlon and F. Semperlotti, "Broadband energy harvesting using acoustic black hole structural tailoring," *Smart Materials and Structures* vol. 23, no. 6, pp. 1–9, 2014.

[6] L. Zhao, S.C. Conlon and F. Semperlotti, "An experimental study of vibration based energy harvesting in dynamically tailored structures with embedded acoustic black holes," *Smart Materials and Structures*, vol. 24, no. 6, pp. 1–9, 2015.

[7] L. Zhao, C. Lai and M. Yu, "Modified structural Luneberg lens for broadband focussing and collimation," *Mechanical Systems and Signal Processing*, vol. 144, pp. 1–10, 2020.

[8] H. Ji, Y. Liang, J. Qiu, L. Cheng, Y. Wu, "Enhancement of vibration based energy harvesting using compound acoustic black holes," *Mechanical Systems and Signal Processing*, vol. 132, pp. 441–456, 2019.

[9] L. Zhang and L. Cheng, "A fully coupled electromechanical model for a PZT-coated acoustic black hole beam," in *INTER-NOISE and NOISE-CON Congress and Conference Proceedings*, vol. 261, no. 1, pp. 5288–5299, 2020.

[10] G. Yao, H. Ji and J. Qiu, "Research of broadband energy harvesting based on two-dimensional acoustic black hole," in *INTER-NOISE and NOISE-CON Congress and Conference Proceedings*, vol. 261, no. 1, pp. 5225–5232, 2020.

[11] O. Gausch, M. Arnela and P. Sánchez-Martín, "Transfer matrices to characterize linear and quadratic acoustic black holes in duct terminations," *Journal of Sound and Vibration*, vol. 395, pp. 65–79, 2017.

[12] O. Gausch, P. Sánchez-Martín and D. Ghilardi, "Application of the transfer matrix approximation for wave propagation in a metafluid representing an acoustic black hole duct termination," *Applied Mathematical Modelling*, vol. 77, pp. 1–13, 2020.

[13] J.P. Hollkamp and F. Semperlotti, "Application of fractional order operators to the simulation of ducts with acoustic black hole terminations," *Journal of Sound and Vibration*, vol. 465, pp. 1–16, 2019.

[14] W. Weaver Jr, S.P. Timoshenko and D.H. Young, "Vibration problems in engineering," 5th edition, *John Wiley & Sons*, USA, 1990.

[15] M.C. Junger and D. Feit, "Sound, structures, and their interaction," *MIT Press*, Cambridge, 1986.

[16] L. Cremer, M. Heckl and B.A.T. Petersson, "Structure-borne Sound," 3rd edition, *Springer*, Germany, 2005.

[17] A.N. Norris, "Flexural waves on narrow plates," *The Journal of the Acoustical Society of America*, vol. 113, no. 5, pp. 3647–2658, 2003.

[18] H. Ji, J. Luo, J. Qiu and L. Cheng, "Investigations on flexural wave propagation and attenuation in a modified one-dimensional ABH using a laser excitation technique," *Mechanical systems and signal processing*, vol. 104, pp. 19–35, 2018.

[19] P.A. Feurtado and S.C. Conlon, "A normalized wave number variation parameter for acoustic black hole design," *The Journal of the Acoustical Society of America*, vol. 136, no. 2, pp. 148–152, 2014.

[20] P.A. Feurtado and S.C. Conlon, "Investigation of boundary-taper reflection for acoustic black hole design," *Noise Control Engineering Journal*, vol. 63, no. 5, pp. 460–466, 2015.

[21] M.R. Shepherd, P.A. Feurtado and S.C. Conlon, "Multi-objective optimization of ABH vibration absorbers," *The Journal of the Acoustical Society of America*, vol. 140, no. 3, pp. 227–230, 2016.

[22] A. Karlos, S. Elliott and J. Cheer, "Higher-order WKB analysis of reflection from tapered elastic wedges," *Journal of Sound and Vibration*, vol. 449, pp. 368–388, 2019.

[23] A.D. Pierce, "Physical interpretation of the WKB or eikonal approximation for waves and vibration in inhomogeneous beams and plates," *The Journal of the Acoustical Society of America*, vol. 48, pp. 275–284, 1970.

[24] M. Mironov and V.V. Pislyakov, "One-dimensional acoustic waves in retarding structures with propagation velocity tending to zero," *Acoustical Physics*, vol. 48, no. 3, pp. 347–352, 2002.

[25] V.V. Krylov, "Conditions for validity of the geometrical-acoustic approximation in application to waves in an acute-angle solid wedge," *Soviet Physics: Acoustics*, vol. 35, no. 2, pp. 176–180, 1989.

[26] V.V. Krylov, "Acoustic black holes: recent developments in the theory and applications," *IEEE transactions on Ultrasonics, Ferroelectrics and Frequency Control*, vol. 61, no. 8, pp. 1296–1306, 2014.

[27] V. Denis, F. Gautier, A. Pelat and J. Poittevin, "Measurement and modelling of the reflection coefficient of an ABH termination," *Journal of Sound and Vibration* vol. 349, pp. 67–79, 2015.

[28] V.B. Georgiev, J. Cuenca, F. Gautier, L. Simon and V.V. Krylov, "Damping of structural vibrations in beams and elliptical plates using the acoustic black hole effect," *Journal of Sound and Vibration*, vol. 330, no. 11, pp. 2497–2508, 2011.

[29] V. Denis, A. Pelat, F. Gautier and B. Elie, "Modal overlap factor of a beam with an ABH termination," *Journal of Sound and Vibration*, vol. 333, no. 12, pp. 2475–2488, 2014.

[30] J.Y. Lee and W. Jeon, "Vibration damping using a spiral acoustic black hole," *The Journal of the Acoustical Society of America*, vol. 141, no. 3, pp. 1437–1445, 2017.

[31] S. Park, M. Kim and W. Jeon, "Experimental validation of vibration damping using an Archimedean spiral acoustic black hole," *Journal of Sound and Vibration*, vol. 459, pp. 1–9, 2019.

[32] S. Park, J.Y. Lee and W. Jeon, "Vibration damping of thin structures using surface-attached spiral acoustic black holes," *Proceedings of Inter-Noise 2020*, Seoul, Korea, 2020, pp. 1–4.

[33] T. Zhou and L. Cheng, "A resonant beam damper tailored with Acoustic Black Hole features for broadband vibration reduction," *Journal of Sound and Vibration*, vol. 430, pp. 174–184, 2018.

[34] N. Wang, H. Ji, C. Zhang, Y. Lu, J. Qiu and L. Cheng, "A new type of two-dimensional acoustic black hole-based vibration absorber," *Proceedings of Inter-Noise 2020*, Seoul, Korea, 2020, pp. 1–11.

[35] E.P. Bowyer, D.J. O'Boy, V.V. Krylov and J.L. Horner, "Effect of geometrical and material imperfections on damping flexural vibrations in plates with attached wedges of power law profile," *Applied Acoustics*, vol. 73, pp. 514–523, 2012.

[36] V.V. Krylov and E. Bowyer, "Acoustic black hole manufacturing for practical applications and the effect of geometrical and material imperfections," in *INTER-NOISE and NOISE-CON Congress and Conference Proceedings*, vol. 253, no. 4, pp. 3924–3934, 2016.

[37] S. Rothe, H. Watschke and S.C. Langer, "Study on the producibility of additively manufactured acoustic black holes," in *24th International Congress on Sound and Vibration*, vol. 24, 2017.

[38] W. Huang, H. Zhang, D.J. Inman, J. Qiu, C.E.S. Cesnik and H. Ji, "Low reflection effect by 3D printed functionally graded acoustic black holes," *Journal of Sound and Vibration*, vol. 450, pp. 96–108, 2019.

[39] J. Cheer and S. Daley, "On the potential of a functionally graded acoustic black hole using multi-material additive manufacturing," in *INTER-NOISE and NOISE-CON Congress and Conference Proceedings*, vol. 261, no. 1, pp. 1–7, 2020.

[40] L. Tang and L. Cheng, "Broadband locally resonant band gaps in periodic beam structures with embedded acoustic black holes," *Journal of Applied Physics*, vol. 121, pp. 1–9, 2017.

[41] S.C. Conlon and J.B. Fahnline, "Numerical analysis of the vibroacoustic properties of plates with embedded grids of acoustic black holes," *The Journal of the Acoustical Society of America* vol. 137, no. 1, pp. 447–457, 2015.

[42] P.A. Feurtado and S.C. Conlon, "Transmission loss of plates with embedded acoustic black holes," *The Journal of the Acoustical Society of America*, vol. 142, no. 3, pp. 1390–1398, 2017.

[43] P.A. Feurtado and S.C. Conlon, "An experimental investigation of acoustic black hole dynamics at low, mid, and high frequencies," *Journal of Vibration and Acoustics*, vol. 138, pp. 1–6, 2016.

[44] P.A. Feurtado and S.C. Conlon, "Wavenumber transform analysis for acoustic black hole design," *Journal of the Acoustical Society of America*, vol. 140, no. 1, pp. 718–727, 2016.

[45] S.C. Conlon and P.A. Feurtado, "Progressive phase trends in plates with embedded acoustic black holes," *The Journal of the Acoustical Society of America* vol. 143, no. 2, pp. 921–930, 2018.

[46] O. Aklouche, A. Pelat, S. Maugeais and F. Gautier, "Scattering of flexural waves by a pit of quadratic profile inserted in an infinite thin plate," *Journal of Sound and Vibration*, vol. 375, pp. 38–52 2016.

[47] A. Pelat, F. Gautier, S.C. Conlon and F. Semperlotti, "The acoustic black hole: A review of theory and applications," *Journal of Sound and Vibration*, vol. 476, pp. 1–24 2020.

[48] J. Deng, O. Gausch and L. Zheng, "Ring-shaped acoustic black holes for broadband vibration isolation in plates," *Journal of Sound and Vibration*, vol. 458, pp. 109–122, 2019.

[49] L. Ma, H-W. Dong and L. Cheng, "An alternative and optimized thickness profile of an acoustic black hole plate," *Journal of Sound and Vibration*, vol. 486, pp. 1–17, 2020.

[50] L. Tang and L. Cheng, "Periodic plates with tunnelled Acoustic-Black-Holes for directional band gap generation," *Journal of Sound and Vibration*, vol. 133, pp. 257–268, 2019.

[51] L. Tang, L. Cheng and K. Chen, "Flexural band gaps in periodic plates with 2D Acoustic black holes," *INTER-NOISE and NOISE-CON Congress and Conference Proceedings*, vol. 261, no. 1. pp. 1–9, 2020.

[52] L. Tang and L. Cheng, "Impaired sound radiation in plates with periodic tunneled Acoustic Black Holes," *Mechanical Systems and Signal Processing*, vol. 135, pp. 1–13, 2020.

[53] L. Ma and L. Cheng, "Topological optimization of damping layout for minimized sound radiation of an acoustic black hole plate," *Journal of Sound and Vibration*, vol. 458, pp. 349–364, 2019.

[54] L. Ma and L. Cheng, "Sound radiation and transonic boundaries of a plate with an acoustic black hole," *Journal of the Acoustical Society of America*, vol. 145, no. 1, pp. 164–172, 2019.

[55] M. Ouisse, D. Renault, P. Butaud and E. Sadoulet-Reboul, "Damping control for improvement of acoustic black hole effect," *Journal of Sound and Vibration*, vol. 454, pp. 63–72, 2019.

[56] L. Zhao, "Passive vibration control based on embedded acoustic black holes," *Journal of Vibration and Acoustics*, vol. 138, pp. 1–6, 2016.

[57] L. Zhao and F. Semperlotti, "Embedded Acoustic Black Holes for semi-passive broadband vibration attenuation in thin-walled structures," *Journal of Sound and Vibration*, vol. 388, pp. 42–52, 2017.

[58] K. Hook, J. Cheer and S. Daley, "A parametric study and modal analysis of an acoustic black hole on a beam," in *Proceedings of ISMA-USD 2018*, pp. 4489–4498, 2018.

[59] K. Hook, J. Cheer and S. Daley, "A Parametric Study of an Acoustic Black Hole on a Beam," *The Journal of the Acoustical Society of America*, vol. 145, no. 6, pp. 3488–3498, 2019.

[60] J. Cheer, S. Daley and K. Hook, "Structural damper," *International Patent Application PCT/GB2020/050769*, 10 2020.

[61] J. Cheer, K. Hook and S. Daley, "Active feedforward control of flexural waves in an Acoustic Black Hole terminated beam," *Smart Materials and Structures* vol. 30, no. 3, pp. 1–14, 2021.

[62] K. Hook, J. Cheer and S. Daley, "Minimisation of the reflection coefficient in a beam using an active acoustic black hole," in *INTER-NOISE and NOISE-CON Congress and Conference Proceedings*, vol. 261, no. 1, pp. 5280–5287, 2020.

[63] K. Hook, J. Cheer and S. Daley, "Optimal feedforward control of a beam with an active acoustic black hole termination," in *26th International Congress on Sound and Vibration*, pp. 1–8, 2019.

[64] K. Hook, S. Daley and J. Cheer, "Feedback active control using an acoustic black hole," in *Proceedings of ISMA-USD 2020*, pp. 1–9, 2020.

[65] D.J. O'Boy, V.V. Krylov and V. Kralovic, "Damping of flexural vibrations in rectangular plates using the acoustic black hole effect," *Journal of Sound and Vibration*, vol. 329, no. 22, pp. 4672–4688, 2010.

[66] C.A. McCormick, and M.R. Shepherd, "Optimal design and position of an embedded one-dimensional acoustic black hole," in *Proceedings of Inter-Noise 2018*, Chicago, IL, USA, 2018, pp. 26–29.

[67] L. Tang, L. Cheng, H. Ji and J. Qiu, "Characterization of acoustic black hole effect using a one-dimensional fully-coupled and wavelet-decomposed semi-analytical model," *Journal of Sound and Vibration*, vol. 374, pp. 172–184, 2016.

[68] F. Fahy and P. Gardonio, "Sound and structural vibration: Radiation, Transmission and Response," *Elsevier*, The Netherlands, 2007.

[69] A. Pelat, V. Denis and F. Gautier, "Experimental and theoretical study of the reflection coefficient of an ABH beam termination," *INTER-NOISE and NOISE-CON Congress and Conference Proceedings*, vol. 250, no. 2, pp. 5001–5009, 2015.

[70] S. Marburg and B. Nolte, "Computational Acoustics of Noise Propagation in Fluids - Finite and Boundary Element Methods," *Springer*, Berlin, pp. 309–332, 2008.

[71] B.H. Song and J.S. Bolton "A transfer-matrix approach for estimating the characteristic impedance and wave numbers of limp and rigid porous materials," *The Journal of the Acoustical Society of America*, vol. 107, no. 3, pp. 1131–1152, 2000.

[72] C.R. Halkyard and B.R. Mace, "Structural intensity in beams—waves, transducer systems and the conditioning problem," *Journal of Sound and Vibration* vol. 185, no. 2, pp. 279–298, 1995.

[73] C.R. Halkyard and B.R. Mace, "Feedforward adaptive control of flexural vibration in a beam using wave amplitudes," *Journal of Sound and Vibration*, vol. 254, no. 1, pp. 117–141, 2002.

[74] B.R. Mace, C.R. Halkyard and H.M. El-Khatib, "Real-time measurement of wave components and intensity in abeam in the presence of a near field," *Journal of Sound and Vibration*, vol. 286, pp. 507–527, 2005.

[75] C.R. Halkyard and B.R. Mace, "Adaptive active control of flexural vibration in a beam in the presence of a nearfield," *Journal of Sound and Vibration*, vol. 285, pp. 149–171, 2005.

[76] J. Leng, V. Romero-García, A. Pelat, R. Picó, J.P. Groby and F. Gautier, "Interpretation of the Acoustic Black Hole effect based on the concept of critical coupling," *Journal of Sound and Vibration*, vol. 471, pp. 1–10, 2020.

[77] W.T. Henley, "Yellow plastic compound," https://www.wt-henley.com/cable_accessories-green_and_yellow_plastic_compound.html, 2021 (Last Accessed: 06/02/2021).

[78] E. Rustighi, B.R. Mace and N.S. Ferguson, "An adaptive anechoic termination for active vibration control," *Journal of Vibration and Control*, vol. 17, no. 13, pp. 2066–2078, 2011.

[79] B.R. Mace and C.R. Halkyard, "Time domain estimation of response and intensity in beams using wave decomposition and reconstruction," *Journal of Sound and Vibration*, vol. 230, no. 3, pp. 561–589, 2000.

[80] D. Doherty, B.R. Mace, N.S. Ferguson and E. Rustighi, "An adaptive anechoic termination for active control of flexural vibration," in *Proceedings of EURODYN 2008, 7th European Conference on Structural Dynamics*, pp. 1–11, 2008.

[81] S.J. Elliott, "Signal Processing for Active Control," *Academic Press*, London, 2001.

[82] PI Ceramic, "PI876.A11 piezo patch," https://static.piceramic.com/fileadmin/user_upload/physik_instrumente/files/datasheets/P-876-Datasheet.pdf, 2021 (Last Accessed: 06/02/2021).

[83] W. Huang, H. Ji, J. Qiu and L. Cheng, "Wave Energy Focalization in a Plate With Imperfect Two-Dimensional Acoustic Black Hole Indentation," *Journal of Vibration and Acoustics*, vol. 138, pp. 1–12, 2016.

[84] T. Zhou, L. Tang, H. Ji, J. Qiu and L. Cheng, "Dynamic and static properties of double-layered compound acoustic black hole structures," *International Journal of Applied Mechanics*, vol. 9, no. 5, pp. 1–18, 2017.

[85] S. Daley and J. Wang, "A geometric approach to the design of remotely located vibration control systems," *Journal of Sound and Vibration*, vol. 318, pp. 702–714, 2008.

[86] J. Wang and S. Daley, "Broad band controller design for remote vibration using a geometric approach," *Journal of Sound and Vibration*, vol. 329, pp. 3888–3897, 2010.

[87] U. Ubaid, S. Daley, S.A. Pope and I. Zazas, "Design of stable and broadband remote vibration controllers for systems with local nonminimum phase dynamics," *IEEE Transactions on control systems technology*, vol. 24, no. 2, pp. 654–661, 2016.

[88] S. Daley and I. Zazas, "A recursive least squares based control algorithm for the suppression of tonal disturbances," *Journal of Sound and Vibration*, vol. 331, pp. 1270–1290, 2012.

[89] L. Ljung, "Recursive identification algorithms," *Circuits, Systems and Signal Processing*, vol. 21, no. 1, pp. 57–68, 2002.

[90] O. Unruh, C. Blech and H.P. Monner, "Numerical and Experimental Study of Sound Power Reduction Performance of Acoustic Black Holes in Rectangular Plates," *SAE International Journal of Passenger Cars-Mechanical Systems*, vol. 8, no. 3, pp. 956–963, 2015.

[91] X. Liu, J. Yuan, H. Liang and Z. Wang, "Study on energy propagation and noise radiation in plates containing the array of acoustic black holes," *Proceedings of Inter-Noise 2020*, Seoul, Korea, 2020, pp. 1–10.

[92] H. Ji, X. Wang, J. Qiu, L. Cheng, Y. Wu and C. Zhang, "Noise reduction inside a cavity coupled to a flexible plate with embedded 2-D acoustic black holes," *Journal of Sound and Vibration*, vol. 455, pp. 324–338, 2019.

[93] L. Cheng, "Sound radiation and transonic boundaries of a plate with an acoustic black hole," *Journal of the Acoustical Society of America*, vol. 145, no. 1, pp. 164–172, 2019.

[94] L. Zhao, "Low-frequency vibration reduction using a sandwich plate with periodically embedded acoustic black holes," *Journal of Sound and Vibration*, vol. 441, pp. 165–171, 2019.

[95] J. Rohlfing, P. Gardonio and D.J. Thompson, "Comparison of decentralized velocity feedback control for thin homogeneous and stiff sandwich panels using electrodynamic proof-mass actuators," *Journal of Sound and Vibration*, vol. 330, no. 20 pp. 4661–4675, 2011.

[96] ISO/TC 43/SC 1 Noise, "Acoustics — Determination of sound power levels of noise sources using sound intensity - Part 1: Measurement at discrete points," *International Organization for Standardization ISO 9614-1:1993*, pp. 1–19, 1993.

[97] J. Milton, J. Cheer and S. Daley, "Experimental identification of the radiation resistance matrix," *The Journal of the Acoustical Society of America*, vol. 145, no. 5, pp. 2885–2894, 2019.